

NASA Contractor Report 159379

(NASA-CR-159379) A STUDY OF OPTIMUM COWL
SHAPES AND FLOW PORT LOCATIONS FOR MINIMUM
DRAG WITH EFFECTIVE ENGINE COOLING, VOLUME I
(North Carolina State Univ.) 119 p
HC A06/MF A01

N83-16288

Unclas
02547

CSCL 01A G3/02

A STUDY OF OPTIMUM COWL SHAPES AND FLOW
PORT LOCATIONS FOR MINIMUM DRAG WITH
EFFECTIVE ENGINE COOLING - VOLUME I

Stan R. Fox and Frederick O. Smetana

NORTH CAROLINA STATE UNIVERSITY
Raleigh, North Carolina 27650

NASA Grant NSG-1584
November 1980

RELEASE DATE:

PUBLICLY RELEASE ON JANUARY 31, 1983



National Aeronautics and
Space Administration

Langley Research Center
Hampton, Virginia 23665

ABSTRACT

The successful prediction of the performance of a new or modified aircraft depends heavily on an accurate estimation of its lift and drag. The present work represents an effort to reduce the cruise drag of light aircraft through an analytical study of the contributions to the drag arising from the shape of the engine cowl and the forward fuselage area and also that resulting from the cooling air mass flow through intake and exhaust sites on the nacelle. It contains descriptions of the methods employed for the calculation of the potential flow about an arbitrary three-dimensional body with modifications to include the effects of boundary layer displacement thickness, a nonuniform onset flow field (such as that due to a rotating propeller), and the presence of air intakes and exhausts. It also contains a simple, reliable, largely automated scheme to better define or change the shape of a body.

A technique has been developed which can yield physically-acceptable skin-friction and pressure drag coefficients for isolated light aircraft bodies. For test cases on a blunt-nose Cessna 182 fuselage, the technique predicted drag reductions as much as 28.5% by body recontouring and proper placements and sizing of the cooling air intakes and exhausts.

TABLE OF CONTENTS

	Page
TABLE OF CONTENTS	111
LIST OF FIGURES	iv
INTRODUCTION	1
THEORETICAL APPROACH OF HESS AND SMITH FOR CALCULATION OF THE POTENTIAL FLOW ABOUT THREE-DIMENSIONAL NON-LIFTING BODIES BY A SURFACE SOURCE- DENSITY DISTRIBUTION METHOD	3
BOUNDARY LAYER SIMULATION FOR BODIES IN AN INVISCID POTENTIAL FLOW FIELD	10
PROPELLER WAKE SIMULATION	18
FLOW PORT LOCATIONS FOR MINIMUM DRAG AND EFFECTIVE ENGINE COOLING	39
A GRID REFINEMENT SCHEME FOR THE MODIFICATION OF A BODY'S GEOMETRIC DATA	51
COMPUTER IMPLEMENTATION OF METHODS	68
DISCUSSION OF RESULTS	69
CONCLUSIONS	110
REFERENCES	111

PRECEDING PAGE BLANK NOT FILMED

LIST OF FIGURES

	Page
1. Body surface represented by an equation of the form $S(x,y,z) = 0$. .	4
2. Notation used in describing the surface source-distribution potential	7
3. The approximate representation of the body surface by quadrilaterals	9
4. Displacement thickness addition to a body	13
5. Illustration of separated strips of elements	14
6. Definition of wake body	15
7. Velocity induction by element of three-dimensional ring vortex . . .	20
8. Formation of the wake by free vortices	22
9. Helical-shaped surface of vorticity	23
10. System of trailing vortices of a propeller with a constant circulation	24
11. Application of vortex rings	25
12. Motion of a single ring vortex	27
13. Mutual influences of two ring vortices	27
14. Leapfrog action of two free vortex rings	28
15. Doublet potential definition	31
16. Matching doublet flow to vortex flow	33
17. Denotation of first and last body axial station with illustration of point numbering	34
18. Equivalent circular body	36
19. Vortex-ring distribution and diameter variation about an aircraft fuselage in the wake of a propeller	38
20. Schematic of cowl interior	40
21. Typical behaviors of the interior pressure coefficients with parameter variation	48

LIST OF FIGURES (continued)	Page
22. Schematic of indexing scheme used for a 3-1 ellipsoid with 40 panels describing the half-body	52
23. Typical translation and rotation scheme of reference coordinate system	54
24. Coordinate information for averaging techniques	57
25. Examples of input-data modification	58
26. Example of equal-line augmentation scheme	59
27. Example of user-specified line-augmentation scheme	61
28. Example of a three-view orthographic projection	63
29. Example of a oblique orthographic projection	64
30. Example of a perspective projection	65
31. Example of stereoscopic projection	66
32. Results of Cessna 182 fuselage model with uniform flow (power-off)	82
33. Results of recontoured Cessna 182 fuselage model with uniform flow (power-off)	83
34. Results of blunt-nose Cessna 182 fuselage model with uniform flow (power-off)	84
35. Results of ATLIT fuselage model with uniform flow (power-off)	85
36. Results of ATLIT nacelle model with uniform flow (power-off)	86
37. Results of a fat nacelle model with uniform flow (power-off)	87
38. Results of Cessna 182 fuselage model with nonuniform flow (power-on)	88
39. Results of recontoured Cessna 182 fuselage model with nonuniform flow (power-on)	89
40. Results of blunt-nose Cessna 182 fuselage model with nonuniform flow (power-on)	90
41. Results of ATLIT fuselage model with nonuniform flow (power-on) . .	91

LIST OF FIGURES (continued)

Page

42. Results of ATLIT nacelle model with nonuniform flow (power-on) . . .	92
43. Results of a fat nacelle model with nonuniform flow (power-on) . . .	93
44. Results of blunt-nose Cessna 182 fuselage model (nonuniform flow, 74.563 kW power, intake and exhaust ports)	94
45. Results of blunt-nose Cessna 182 fuselage model (nonuniform flow, 100.66 kW power, intake and exhaust ports)	96
46. Results of blunt-nose Cessna 182 fuselage model (nonuniform flow, 223.69 kW power, intake and exhaust ports)	98
47. Variation of total drag coefficient C_D with power for blunt- nose Cessna fuselage model with fixed intake and exhaust sites	100
48. Comparison of drag coefficients between prediction and wind-tunnel tests	100
49. Behavior of pressure coefficients with effective orifice area . . .	101
50. Behavior of drag coefficient with effective orifice area	101
51. Results of blunt-nose Cessna 182 fuselage model (nonuniform flow, 74.563 kW power, 0.023 m ² initial EOA, intake and exhaust sites)	102
52. Results of blunt-nose Cessna 182 fuselage model (nonuniform flow, 74.563 kW power, 0.046 m ² initial EOA, intake and exhaust sites)	104
53. Results of blunt-nose Cessna 182 fuselage model (nonuniform flow, 74.563 kW power, 0.093 m ² initial EOA, intake and exhaust sites)	106
54. Results of blunt-nose Cessna 182 fuselage model (nonuniform flow, 74.563 kW power, 0.93 m ² initial EOA, intake and exhaust sites)	108

INTRODUCTION

The successful prediction of the performance of a new or modified aircraft depends heavily on an accurate estimation of its lift and drag. Although the importance of these data is recognized, many light aircraft manufacturers and most universities continue to depend essentially on the semi-empirical correlations of wind tunnel and flight test data along with personal rules of thumb in order to develop these estimates.

For some time sophisticated techniques utilizing high-speed digital computers have been available to predict the performance characteristics of light aircraft. Although quite accurate, most of these techniques consume large amounts of computational time and computer core storage. Several attempts - some successful - have been made within the last five to ten years to reduce the time required to perform these estimates without significant sacrifices in accuracy. These technological advances provide suitable starting points for the designer to "test" new or modified aircraft shapes without the expensive and time-consuming wind tunnel and flight tests.

The present work represents an effort to reduce the cruise drag of light aircraft through an analytical study of the contributions to the drag arising from the engine cowl shape and the forward fuselage area and as well as that due to the cooling air mass flowing through intake and exhaust sites on the nacelle. Since efficient fuel use is an increasingly important factor in general aviation operations, any design procedure which can lower the fuel consumption of a variety of aircraft through a drag clean-up is a welcomed advance in technology.

This report contains descriptions of the methods employed for the calculation of the potential flow about an arbitrary three-dimensional body with appropriate modifications to include the effects of (a) the boundary layer over the body, (b) a nonuniform onset flow field about the body - typically produced by a rotating propeller, and (c) the presence of air intake and exhaust sites on the body for engine cooling purposes. The basic potential flow solution is accomplished by a solution of a Fredholm equation of the second kind, while the effects of the boundary layer, the nonuniform flow field, and the air intake and exhaust sites are included as the boundary conditions to the Fredholm equation.

As an aid in the preparation of the input data to potential flow calculations, this report also discusses a simple, reliable, largely automated geometry scheme to augment and/or to modify the body shape information by various techniques. Being expeditious and inexpensive, this scheme - a digital computer program - is a valuable tool to the researcher who wishes to better define or change the shape of a complete body or of regions on the body of particular interest before beginning the potential flow calculations.

THEORETICAL APPROACH OF HESS AND SMITH FOR CALCULATION OF POTENTIAL FLOW ABOUT THREE- DIMENSIONAL NON-LIFTING BODIES BY A SURFACE SOURCE-DENSITY DISTRIBUTION METHOD

The problem under consideration is that of the potential flow of an incompressible, inviscid fluid about an arbitrary three-dimensional body. If the fluid density is constant and the viscosity is zero, the general Navier-Stokes equations reduce to the Eulerian equations of motion

$$\frac{\partial \vec{V}}{\partial t} + (\vec{V} \cdot \text{grad}) \vec{V} = - \frac{1}{\rho} \text{grad } p \quad (1)$$

where \vec{V} is the fluid velocity at any point, ρ is the constant fluid density, and p is the fluid pressure. The continuity equation becomes

$$\text{div}(\vec{V}) = 0 \quad (2)$$

All body forces are assumed to be conservative and their potentials absorbed in the pressure. Therefore equations (1) and (2) are valid expressions for the flow field exterior to the boundary surfaces.

In order to discuss the flow about a three-dimensional body surface, let R' denote the exterior flow field and S denote the surface of the body (also the boundary of the region R). The body is assumed to have a surface represented by an equation of the form

$$S(x,y,z) = 0 \quad (3)$$

where x , y , and z are the Cartesian coordinates as depicted in Figure 1. Under the assumption that the location of all boundary surfaces are known and that

ORIGINAL PAGE IS
OF POOR QUALITY

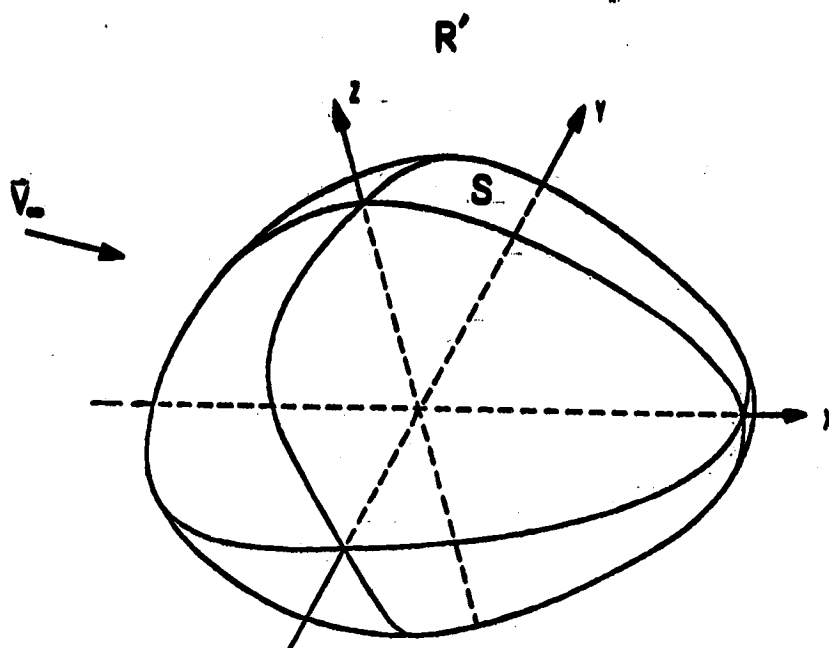


Figure 1. Body surface represented by an equation of the form $S(x,y,z) = 0$

the normal component of fluid velocity is prescribed on these boundaries, the boundary conditions may be given as

$$\vec{V} \cdot \vec{n}|_S = F \quad (4)$$

where \vec{n} is the unit outward normal vector at a point on S and F is a known function of position or time or both. To be complete, a regularity condition at infinity must be imposed for the exterior flow problem. The onset flow \vec{V}_∞ is assumed to be a uniform stream of unit magnitude; however, this restriction is not essential to the general derivation.

It should be noted that the above equations do not define a potential flow. Since potential flow is a consequence of the condition of irrotationality, the usual approach to determine the equations of potential flow is to

ORIGINAL PAGE IS
OF POOR QUALITY.

assume that the velocity field \vec{V} is irrotational and therefore the velocity field can be expressed as the negative gradient of a scalar potential function ϕ .

Letting the velocity field \vec{V} be the sum of the uniform, incompressible onset flow \vec{V}_∞ and the perturbation velocity field \vec{v} due to the surface boundaries, then

$$\vec{V} = \vec{V}_\infty + \vec{v} \quad (5)$$

where

$$\vec{v} = - \text{grad } \phi \quad (6)$$

Since the onset flow and the perturbation flow are incompressible, the continuity equation (2) is satisfied:

$$\left[\begin{array}{l} \text{div}(\vec{V}_\infty) = 0 \\ \text{div}(\vec{v}) = 0 \end{array} \right] \Rightarrow \text{div}(\vec{V}) = 0$$

As expected, the potential ϕ satisfies Laplace's equation

$$\nabla^2 \phi = 0 \quad (7)$$

in the region R' exterior to surface S . By equation (4) the boundary conditions on ϕ become

$$\text{grad } \phi \cdot \vec{n}|_S = \frac{\partial \phi}{\partial n}|_S = \vec{V}_\infty \cdot \vec{n}|_S - F \quad (8)$$

and the regularity condition for the exterior problem becomes

$$|\text{grad } \phi| \rightarrow 0 \text{ at infinity} \quad (9)$$

Therefore equations (7), (8), and (9) represent the necessary potential flow equations to be solved.

As demonstrated above, potential flow is derived from the fact that the velocity field is determined by the continuity equation (2) and the condition of irrotationality (6). Thus equation (1) is not used, and the velocity may be determined independently of the pressure. Even though Laplace's equation (7) is the simplest and best known of all partial differential equations, the number of useful exact analytical solutions is quite small because of the difficulty in satisfying the boundary conditions. Therefore indirect* methods of solution must be used to give satisfactory results from the various prescribed body surfaces and boundary conditions.

The reduction of the problem to an integral equation for a source-density distribution on the body surface can be accomplished by the use of Green's theorem. The problem now is to reduce the potential flow equations (7), (8), and (9) to an integral equation. For a single three-dimensional body, consider a unit point source located at a point q whose Cartesian coordinates are x_q , y_q , and z_q in Figure 2. At a point P with coordinates x , y , and z , the potential due to this source is

$$\phi = \frac{1}{r(P,q)} \quad (10)$$

where $r(P,q)$ is the distance between points P and q . The solution is

* Indirect or exact numerical methods contain the exact analytical formulation to the problem and have the property that the errors in the calculated results can be made as small as desired by refining the numerical procedures. Approximate methods contain analytical approximations in the formulation itself and thus places an accuracy limit on the results regardless of the numerical procedures used.

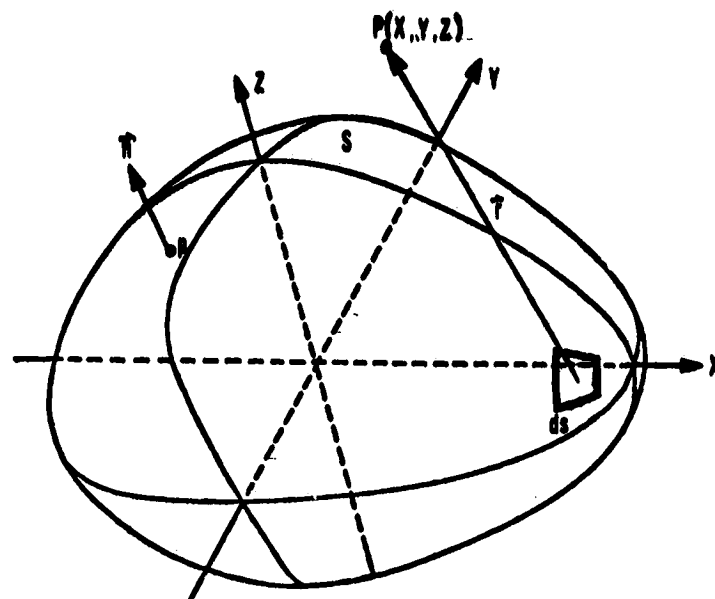


Figure 2. Notation used in describing the surface source-distribution potential

constructed of elementary potentials of the above form of an ensemble of sources. The resulting potential satisfies equation (9) and satisfies equation (7) at all points except q . Because of the linearity of the problem, such a potential that is internal or upon the boundary surface S satisfies equation (9) and satisfies equation (7) in the region R' that is external to S . It is of considerable importance to determine the potential of a continuous source distribution on the surface S .

Let $\sigma(q)$ be the local source distribution intensity, where the point q now represents a general point on the surface S . The potential of this distribution is

$$\phi = \oint_S \frac{\sigma(q)}{r(P,q)} dS \quad (11)$$

By the procedure given by Kellogg [3], the perturbation potential is given by equation (11) is differentiated, and the boundary condition (8) applied to it by permitting the point P to approach a point q on the surface S. The result is the following integral equation for the source-density distribution $\sigma(p)$:

$$2\pi\sigma(p) - \oint_S \frac{\partial}{\partial n} \left(\frac{1}{r(P,q)} \right) \sigma(q) dS = - \vec{n}(p) \cdot \vec{V}_\infty + F \quad (12)$$

where $\frac{\partial}{\partial n}$ denotes differentiation in the direction of the outward normal to the surface S at the point p, and $\vec{n}(p)$ is the unit outward normal vector (written explicitly to show its dependence on location). Equation (12) is a Fredholm integral equation of the second kind over the boundary surface S.

The method of solution of Equation (12) is demanded to be numerical rather than analytical by the fact that the domain of integration is completely arbitrary. The solution can be accomplished by first representing the body surface by a large number of small quadrilateral elements or "panels" (Figure 3). On each quadrilateral a control point is selected (usually the centroid) where the boundary condition is to be satisfied and where surface velocities are eventually calculated. A "matrix of influence coefficients", consisting of the complete set of velocities induced by the panels at each other's control points, is then determined. The integral equation (12) is now approximated by a set of linear algebraic equations for the values of the source strengths on the panels. Since each panel is assumed to have an independent value of constant source strength, the number of unknown parameters (source strengths) equals the number of panels or, more specifically, the number of linear equations. Once the source strengths are determined, the desired flow parameters may be calculated. This implementation renders the method as numerically "exact" and applicable to any arbitrary non-lifting body.

ORIGINAL PAGE IS
OF POOR QUALITY

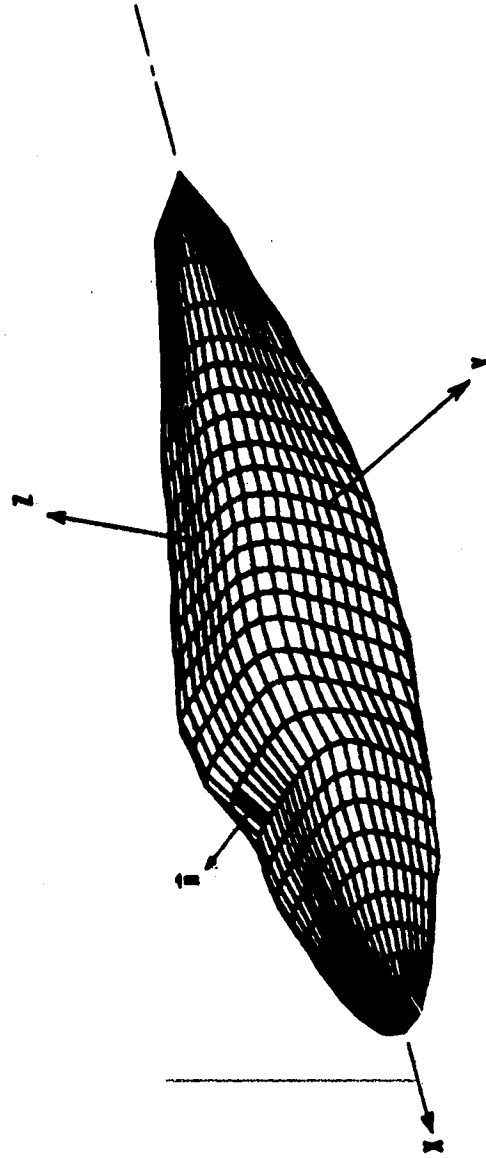


Figure 3. The approximate representation of the body surface by quadrilaterals

BOUNDARY LAYER SIMULATION FOR BODIES IN AN INVISCID POTENTIAL FLOW FIELD

Because of the considerations of large computation times, an "exact" numerical solution of the complete Navier-Stokes equations is not feasible at this time. Yet the problem of determining the characteristics of a boundary layer flowing over a general, three-dimensional body is of great interest if real viscous flow effects are to be approximated.

For essentially unseparated flow about a body at practical Reynolds numbers, the effects of viscosity are important only in a very thin boundary layer adjacent to the body's surface and in a thin wake downstream of the body. The following discussion will be restricted to the low-speed regime where the flow is incompressible or where the compressibility effects are sufficiently small to be handled by simple correction to an incompressible flow method.

Smetana et al. [4] and Hess [5] utilized a method of a two-dimensional boundary layer simulation technique expounded by Lighthill [6]. This method, that of surface displacement or flow reduction, essentially consists of producing a thicker body by adding the boundary layer displacement thickness to the original body in the direction along the local normal to the body surface. The potential flow about this modified body is thus the desired potential flow to approximate viscous flow effects. This method is reasonably accurate if the body's cross-sectional area and volume do not change rapidly in the stream-wise direction, if no significant pressure gradients exist in the cross flow direction, and if the wake is adequately modeled (see Smetana et al. [4], pp. 125-132).

Since the present work is essentially an extension of the work of Smetana et al. [4] of approximating real flows about light aircraft fuselages with an inviscid, incompressible flow method, their procedure for the calculation of the displacement thickness, wall shear, and, ultimately, the lift and drag on a fuselage will be discussed briefly. It should be pointed out that a fuselage is generally considered to be a body with a plane or symmetry (normally the x-z plane) rather than an axis of symmetry. Effectively, this consideration simplifies the implementation of the method but also restricts its generality.

Under certain conditions, as mentioned above, the three-dimensional boundary layer equations can be reduced to "simpler" two-dimensional equations written in a general curvilinear coordinate system which describe the fuselage surface. By representing the fuselage locally by a section of a prolate spheroid with its major axis aligned with the local streamline* and its center in the x-z plane, the direction and magnitude of the flow velocity at one point on each panel may be determined by the induced velocity equations (6). At the points where the boundary condition (8) is to be satisfied, these vectors (the streamlines) whose directions are the flow directions and whose lengths are proportional to the flow magnitudes can be easily determined. The method of isoclines may be used to sketch these streamlines; however, for computational purposes it is desirable to describe these lines in a more analytical fashion by assuming that for a given panel the flow direction across this panel is constant and that the quantity of flow is dependent on the distance and average

*To adjacent streamlines form the boundaries of the flow of a given quantity of fluid. From the magnitude and direction of the flow over the surface, the position of these streamlines on the body may be determined.

velocity between adjacent streamlines. Therefore it is noted that since the quantity of fluid between two streamlines is always constant, the flow velocity is increased for converging streamlines and is decreased for diverging streamlines. Also, this assumption is seen to be true only for infinitesimal panel sizes.

After fitting a section of the prolate spheroid to a section of the fuselage, as described by Smetana et al. [4], the boundary layer equations written in general curvilinear coordinates are used with the local values of the section to determine the effects of body curvature on the displacement thickness and wall shear using a momentum integral formulation. At this point, the necessary means to describe the local streamwise and crossflow coordinates on the body in terms of the reference coordinate system are available (as well as to write the boundary layer equations in a general curvilinear coordinate system).

To preserve the metrics of the general curvilinear coordinate system, the displacement thickness must be added normal to the body surface. In essence, a surface panel is translated parallel to its normal vector by an amount equal to the value of the displacement thickness calculated at the point where the boundary condition was satisfied. As shown in Figure 4, adjacent panels after the addition of the displacement thicknesses may not have coincident edges. This difficulty is quickly eliminated by simply averaging the new edge points 1 and 2 to yield a new point. It is also observed in Figure 5 that a single line* dividing two strips of elements now becomes two lines. Again this difficulty is remedied by averaging corresponding points on these lines to yield

*The connotation used above of "line" or "lines" actually represent a curve or curves in three-dimensional space. The sole purpose of this usage is the simplicity in viewing.

ORIGINAL PAGE IS
OF POOR QUALITY

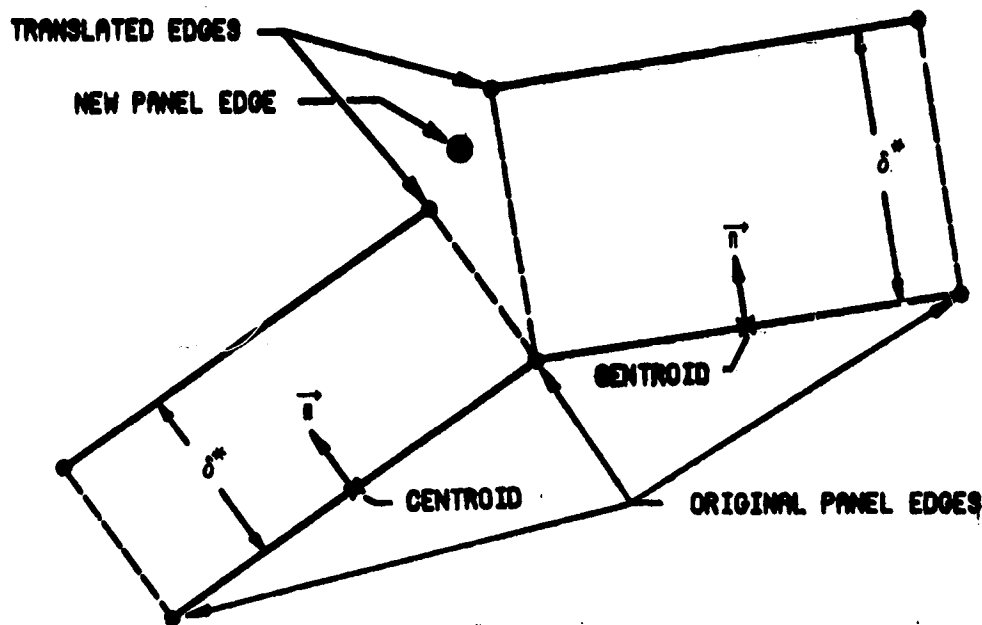


Figure 4. Displacement thickness addition to a body

a single line. A word of caution should be mentioned at this point. It is recognized in Figures 4 and 5 that the averaging procedure can translate and rotate the panels. Therefore the metrics of the general curvilinear coordinate system are no longer preserved. The error introduced may be quite significant if the surface curvature varies rapidly from panel to adjacent panels.

Since this method for determining the pressures and velocities over the surface of the body is an inviscid one, it always places a stagnation point at the downstream end of the closed body. As a result, the method predicts stagnation pressures at the aft end of the body in what is physically a wake region. The pressures in this wake region is generally less than atmospheric. This relatively low pressure on the aft portion of the body as opposed to the high

ORIGINAL PAGE IS
OF POOR QUALITY

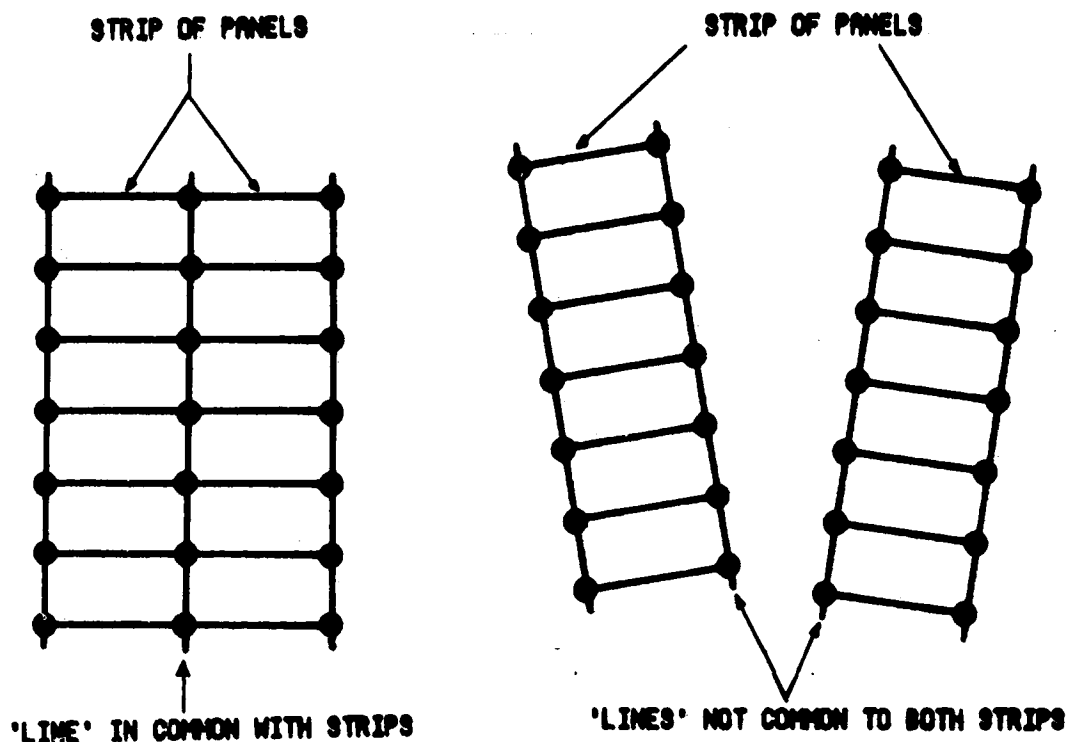


Figure 5. Illustration of separated strips of elements

pressure region near the nose resolves into a force acting in the flow direction which is commonly known as form or pressure drag. It is apparent that for bodies producing regions of flow separation a reasonably accurate model to represent the wake effects must be used if meaningful drag results are to be obtained.

Smetana et al. [4] replaced the physical wake by a solid extension of the physical body since the wake may be considered as a region of "dead" air relative to the remaining flow field. They also assumed, rather arbitrarily,

ORIGINAL PAGE IS
OF POOR QUALITY.

that this solid extension (or wake-body) begins at about the last ten percent of the length of the physical body, and that the wake-body surface gradually tapers via an exponential function.

The surface of this wake-body is assigned quadrilaterals or panels of approximately the same area as those on the physical body, as depicted in Figure 6.

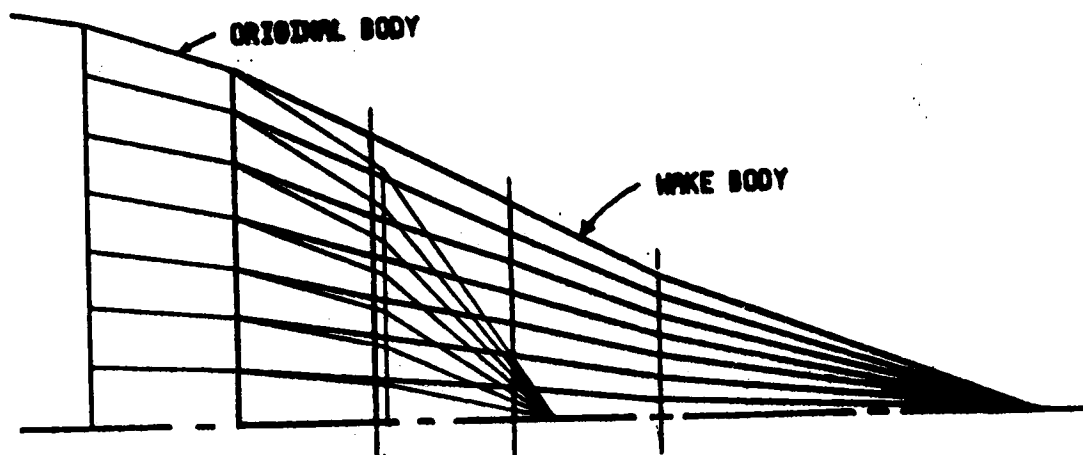


Figure 6. Definition of wake body

The pressures, as determined by the inviscid flow method, on those panels of the wake-body which lie immediately above the equivalent panels on the physical body are applied to the panels on the physical body along the normals to the physical body. The pressures are integrated over the body surface, and the resulting forces acting on the physical body can be summed to find a lift and a drag. Since the pressures on the upstream portion of the wake-body will generally be less than those on the rear of the physical body according to the inviscid flow computation, the integration of forces will indicate a net drag on the body. The total drag on the body is, of course, the sum of the pressure drag and the skin friction drag.

The method discussed above is thereby characterized by the following steps:

- (1) The surface of the isolated fuselage is represented by a sufficiently large number of quadrilaterals or four-sided panels.
- (2) All four corners of the panel are moved into the same plane through a procedure which determines the direction of the normal.
- (3) A source of undetermined strength is placed on each panel, and the prescribed normal boundary condition is required to be satisfied.
- (4) The resulting system of equations are solved for the source strengths.
- (5) The velocity over the body surface is calculated, and the streamlines and surface pressures are determined.
- (6) Two-dimensional, momentum-integral-type boundary layer computations are performed along streamlines to find the local values of displacement thickness and wall shear.
- (7) The wall shear is integrated over the surface to find the skin friction drag of the isolated fuselage.
- (8) The body shape is modified by attaching a wake-body toward the trailing edge and by accounting for the displacement thickness effects.
- (9) A new set of source strengths and surface pressures corresponding to the wake-body shape is calculated.
- (10) The surface pressures are integrated to find the lift and pressure drag.
- (11) The total drag is determined from the sum of the skin friction drag and the pressure drag.

This method does have imposed restrictions and limitations as discussed in [4]. It should be observed that the boundary-layer computations were allowed to iterate only once because of the great amount of work involved in successively

modifying the body shape to account for displacement thickness effects. The displacement thickness over the forward part of the body is usually small and the use made of this information over the aft portion of the body in the present method's drag calculations is rather approximate. If the fuselage geometry is adequately presented to the inviscid flow field computation or if pressure gradients are such that flow separation is imminent only over the far aft portion of the body, the calculated results are quite acceptable and compare very well to experimental results. Otherwise, the user must examine the results with caution and, based on experiments and engineering judgement, decide their reliability.

PROPELLER WAKE SIMULATION

Flow visualizations of a typical wake (or slipstream) generated by an aircraft propeller verify that proper modeling of such a phenomenon is mathematically extremely difficult, if not impossible. For decades investigators have been studying this problem in the attempt to develop adequate mathematical models to predict the flow characteristics within the wake and the wake's influence on its surroundings. Significant advancements have been made through the research on helicopter rotors, summarized by Stepniewski [7]. Effectively, the wake of helicopter rotors (in the hovering mode) may be considered to be synonymous with that of aircraft propellers, assuming of course that their differences are noted and understood.

It is not the intent of this report to expound on the various methods devised through the decades or to present a new one. It is of concern to simulate the effects of a propeller-like wake upon the inviscid potential flow calculations of a three-dimensional body, namely, an aircraft fuselage or nacelle. The method to be utilized is that commonly known as a prescribed, rigid wake.*

In the study of wake structures, vortex theory is especially useful since the observed behavior of physical wakes can be mathematically explained through its fundamental concepts. Classical expressions of the Biot-Savart law can be

* A prescribed wake is one that is defined empirically rather than allowing it to form freely. A rigid wake is one that remains invariable with time.

applied when establishing the relationships between the strength and geometry of the vortices, and the velocities induced by them in the surrounding fluid. The basic definitions and laws of vortex motion will be presently stated for later convenience.

Even though one of the principal characteristics of ideal-fluid motion is its irrotationality, it is often necessary to consider flows in which a few points, lines, or regions of locally rotational flow exist. It is often possible to analyze viscous fluid motions as being irrotational, except at the locations where the rotation is concentrated.

The vorticity vector is simply defined to be twice the fluid rotation vector or to be the curl of the velocity vector. A *vortex line* is a line in the fluid giving the direction of the vorticity at every point on that line. A *vortex tube* is a tube of finite cross-sectional area on whose surface (known as a *vortex surface*) the vorticity vector is always tangential. A *vortex filament* is a "vortex tube" with an infinitesimal cross-sectional area, whose axis is a vortex line, and a finite value of circulation.

The behavior of vortex filaments in an ideal fluid is governed by the following theorems or laws of Helmholtz and Kelvin:

1. The strength of vortex filament or tube is invariant at all cross sections along the axis.
2. A vortex filament or tube cannot end in the fluid; that is, it must extend to the boundaries of the motion or form a closed loop.
3. If an inviscid fluid, subject to conservative external forces, is originally irrotational, it will remain irrotational.

As the tool for the determination of the induced flow field of a three-dimensional vortex system, the Biot-Savart law can be developed by using the

where the line integral indicates that the integration is performed along the line of the filament L in the direction of $d\vec{l}$ with a clockwise circulation around L , and \vec{r} is the distance between the point P and the element $d\vec{l}$. As indicated in the above figure and by the cross product $d\vec{l} \times \vec{r}$, the velocity increment (13) due to the element is perpendicular to the plane of \vec{r} and $d\vec{l}$.

Baskin et al. [8] suggested the following procedure: The induced velocity vector (14) is resolved into the Cartesian components u , v , and w along the x , y , and z axes, respectively. Let the equation of the line L be given in the parametric form

$$\xi = \xi(\theta), \quad \eta = \eta(\theta), \quad \zeta = \zeta(\theta) \quad (15)$$

where θ is the parameter (being suggestive as an angle for the curved filament). As the parameter θ varies from its initial value θ_i to its final value θ_f , point $Q(\xi, \eta, \zeta)$ describes the curve L . The vectors \vec{r} and $d\vec{l}$ can be expressed as

$$\begin{aligned} \vec{r} &= (\xi - x)\hat{i} + (\eta - y)\hat{j} + (\zeta - z)\hat{k} \\ d\vec{l} &= \left(\frac{d\xi}{d\theta} d\theta\right)\hat{i} + \left(\frac{d\eta}{d\theta} d\theta\right)\hat{j} + \left(\frac{d\zeta}{d\theta} d\theta\right)\hat{k} \end{aligned} \quad (16)$$

where \hat{i} , \hat{j} , and \hat{k} are unit vectors of the x , y , z coordinate system.

Substituting the above expression into (14), the x , y , and z components of the induced velocity are determined to be

$$u = \frac{\Gamma}{4\pi} \int_{\theta_i}^{\theta_f} \left[\frac{d\eta}{d\theta} (\zeta - z) - \frac{d\zeta}{d\theta} (\eta - y) \right] \frac{d\theta}{d^3} \quad (17)$$

$$v = \frac{\Gamma}{4\pi} \int_{\theta_i}^{\theta_f} \left[\frac{d\zeta}{d\theta} (x - \xi) - \frac{d\xi}{d\theta} (\zeta - z) \right] \frac{d\theta}{d^3} \quad (18)$$

ORIGINAL PAGE IS
OF POOR QUALITY

$$w = \frac{\Gamma}{4\pi} \int_{\theta_1}^{\theta_2} \left[\frac{d\xi}{d\theta} (y - \eta) - \frac{d\eta}{d\theta} (x - \xi) \right] \frac{d\theta}{d^3} \quad (19)$$

where

$$d = \sqrt{(x - \xi)^2 + (y - \eta)^2 + (z - \zeta)^2} . \quad (20)$$

Emanating from the blades of the propeller, free vortices form the wake. These free vortices can be subdivided into shed vortices which, at the moment of leaving the blade, are parallel to its axis, and trailing vortices outflowing along the blade span in the direction either perpendicular or approximately perpendicular to the blade axis as depicted by Figure 8. Among the trailing vortices, the tip vortices (those leaving the blade tips) usually dominate the

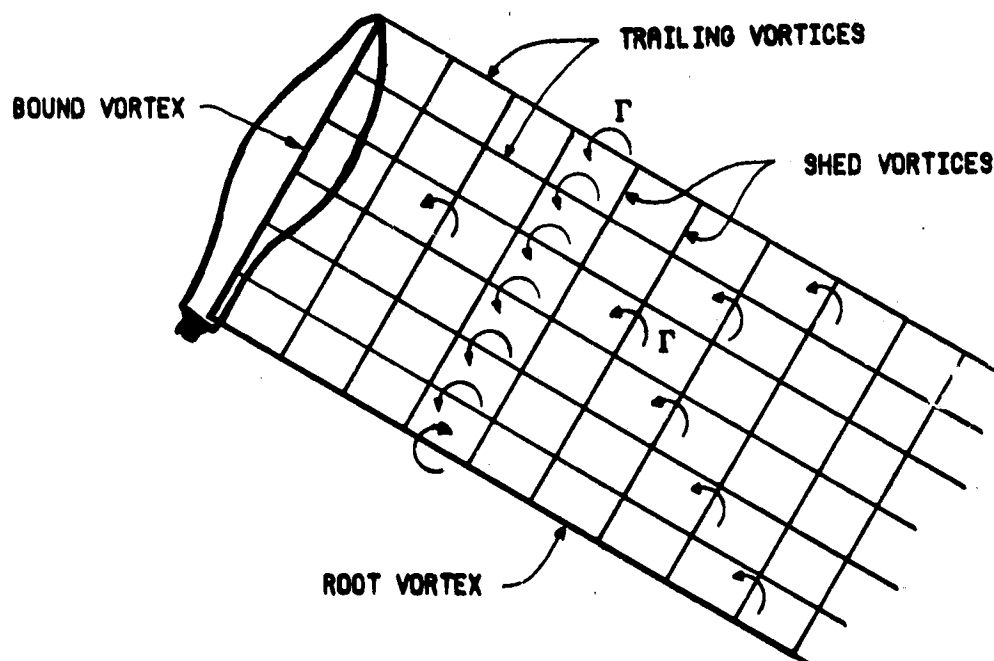


Figure 8. Formation of the wake by free vortices

ORIGINAL PAGE IS
OF POOR QUALITY.

flow picture in all regions of operation. In the complete vortex system the shed and trailing vortices may form a surface of vorticity of a generally helical shape behind each blade as indicated by Figure 9.

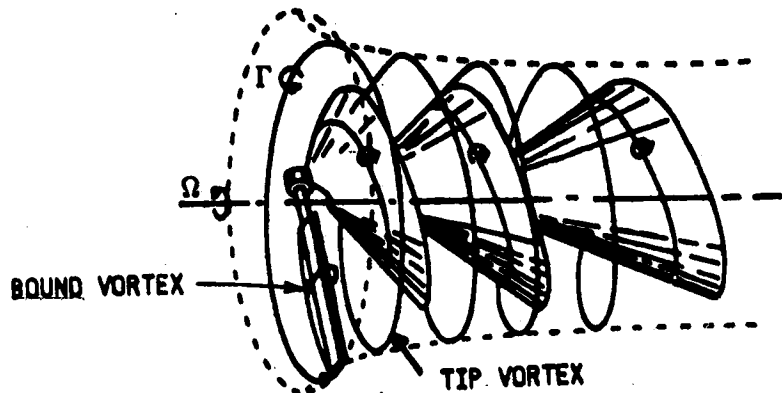


Figure 9. Helical-shaped surface of vorticity

It is easy to comprehend that, in reality, the geometry of the wake and the strengths of the vortices forming that wake may vary with time because of the interaction between the vortices, flow fluctuations, blade rotation, etc.

In this report a simple concept* of the wake will be used since the sole purpose of the simulation is to superimpose the resulting nonuniform induced flow field on a three-dimensional body for an inviscid potential flow calculation. Since the tip vortices are most prevalent, it seems natural to assume

*More sophisticated physicomathematical methods for modeling the wake structure are available for computer implementation. These techniques, as applied to the analysis of helicopter rotors, are discussed by Stepniewski [7].

that the circulation around the blade remains nearly constant along its entire span and to approximate the wake structure by modeling only the tip vortices. The tip vortices will trace out roughly the paths traveled by the tips of the propeller blades. For a two-bladed propeller, Figure 10 represents the system of trailing vortices of a propeller with a constant circulation from the root to the tip of the blades.

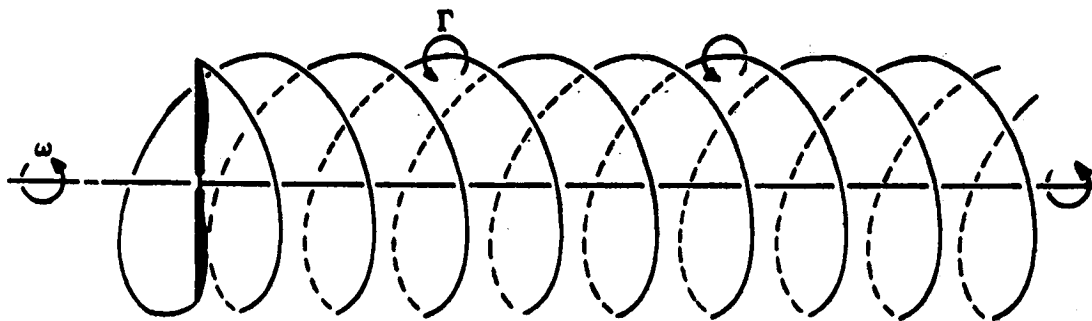


Figure 10. System of trailing vortices of a propeller with a constant circulation

These vortex lines or filaments constitute the slipstream (wake), and the fluid motion in this slipstream can be determined as the induced velocity of the system of vortices. The fluid in the slipstream has an increased axial velocity, and the rotational velocity is in the same sense as the rotation of the propeller. Therefore, the general behavior of the flow is the same as that postulated by the momentum theory.

Physically, the strength of the circulation will vary along the blade. Due to this variation, trailing vortices will arise, not only at the root and tip of the blade, but from every point of its trailing edge as shown in Figures 8 and 9. Since the induced velocity of a system of helical-shaped vortex surfaces which constitute the propeller's slipstream is difficult to calculate,

ORIGINAL PAGE IS
OF POOR QUALITY

the usual procedure is to assume that the propeller has a very large number of blades or that the propeller has a near-zero advance angle. This assumption implies that the vorticity of the slipstream is distributed throughout the system instead of being concentrated on a small number of vortex surfaces.

Instead of the helical surfaces, the slipstream may be considered as a close succession of vortex rings. These vortex rings can be applied to and within the boundaries of the slipstream as shown in Figure 11.

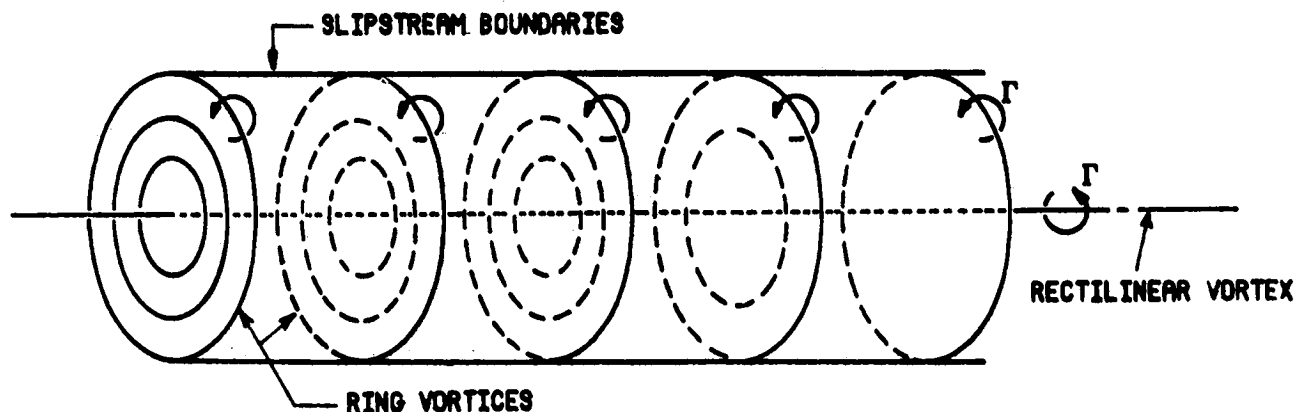


Figure 11. Application of vortex rings

The vortex rings applied at the boundaries of the slipstream represent the tip vortices while those applied within the boundaries represent the trailing vortices springing from the blade due to the variation of circulation along the blade. The vorticity of such systems of vortex rings represents the increased axial velocity of the slipstream, and the vorticity of the rectilinear vortex, constituting the sum of the root trailing vortices, represents the rotation of the slipstream. The whole slipstream can be considered to be full of vortex systems of this simple type.

If the slipstream is allowed to contract as it would in real flows, the condition of continuity of the flow requires that the axial velocity and the

angular velocity must increase as the radius of the slipstream decreases. If the contraction of the slipstream can be ignored, the axial velocity in the ultimate wake must be equal to twice that at the plane of the propeller.* This result is exactly that found by the momentum theory for propellers [9].

According to the theorems of Helmholtz and Kelvin, there is no exchange of either mass or momentum between the vortex filament and the rest of the fluid. Hence, if a vortex filament were located in a mass of moving fluid, it would move with the fluid. Thus velocity fields induced by a system of vortices can, in turn, produce motion of those vortices belonging to the system.

At this point it is informative to discuss the motion of ring vortices if the vortices are free to convect in the fluid. For a single ring vortex (Figure 12a), the streamlines of the induced velocity (Figure 12b) may be divided into their velocity components and vectorially summed to obtain only an axially-directed velocity, since the y- and z-components sum to zero. Therefore, a single ring vortex translates along its axis due to its own induced velocity field.

The motion of two ring vortices of equal strength, size, and sense on the same axis is easily comprehended by considering their mutual influences. Each ring induces components of velocity into the core of the other as sketched for a meridional plane in Figure 13. The forward ring receives an outward induced

*With no slipstream contraction, the vortex system is simply a long cylinder of vorticity extending indefinitely in one direction from the propeller disc. The induced axial velocity at a point in the wake, where the cylinder extends indefinitely in both directions, must be double that at the corresponding point in the propeller disc.

ORIGINAL PAGE IS
OF POOR QUALITY.

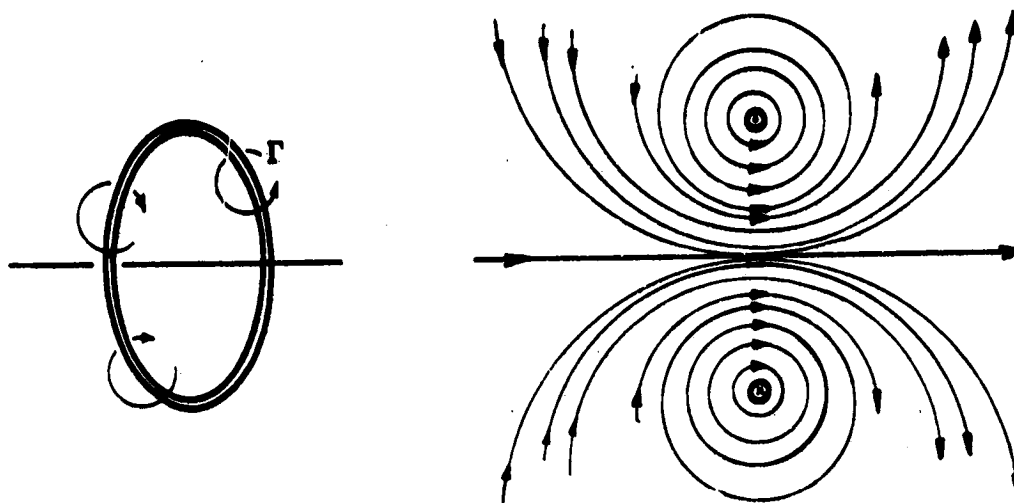


Figure 12. Motion of a single ring vortex

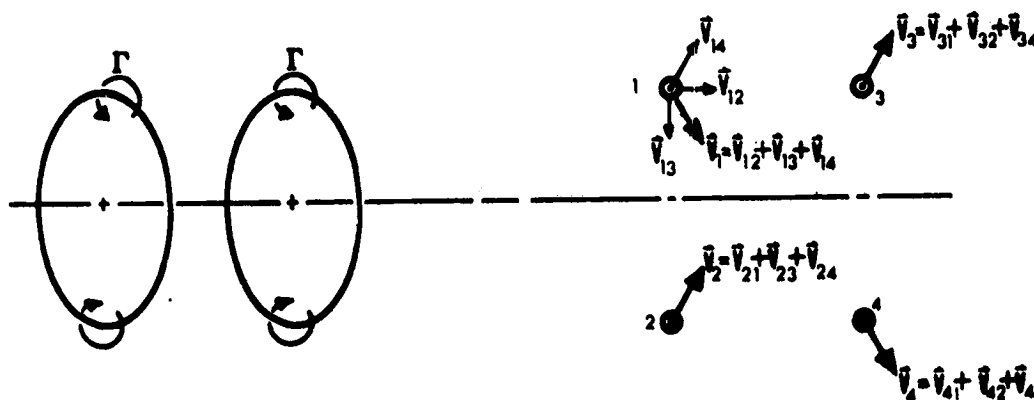


Figure 13. Mutual influences of two ring vortices

velocity component, while the rearward ring receives an inward component. As its diameter increases, the forward ring decreases in speed, according to equation (14), while for the same reason the rearward ring increases in speed

ORIGINAL PAGE IS
OF POOR QUALITY

due to its decreasing diameter. Soon the smaller, faster rearward ring passes through the larger, slower forward ring. The roles of the vortices are now reversed. The smaller ring enlarges and its speed decreases, while the larger one decreases in diameter and speeds up. This leapfrog process, sketched in Figure 14, continues endlessly in an inviscid fluid.

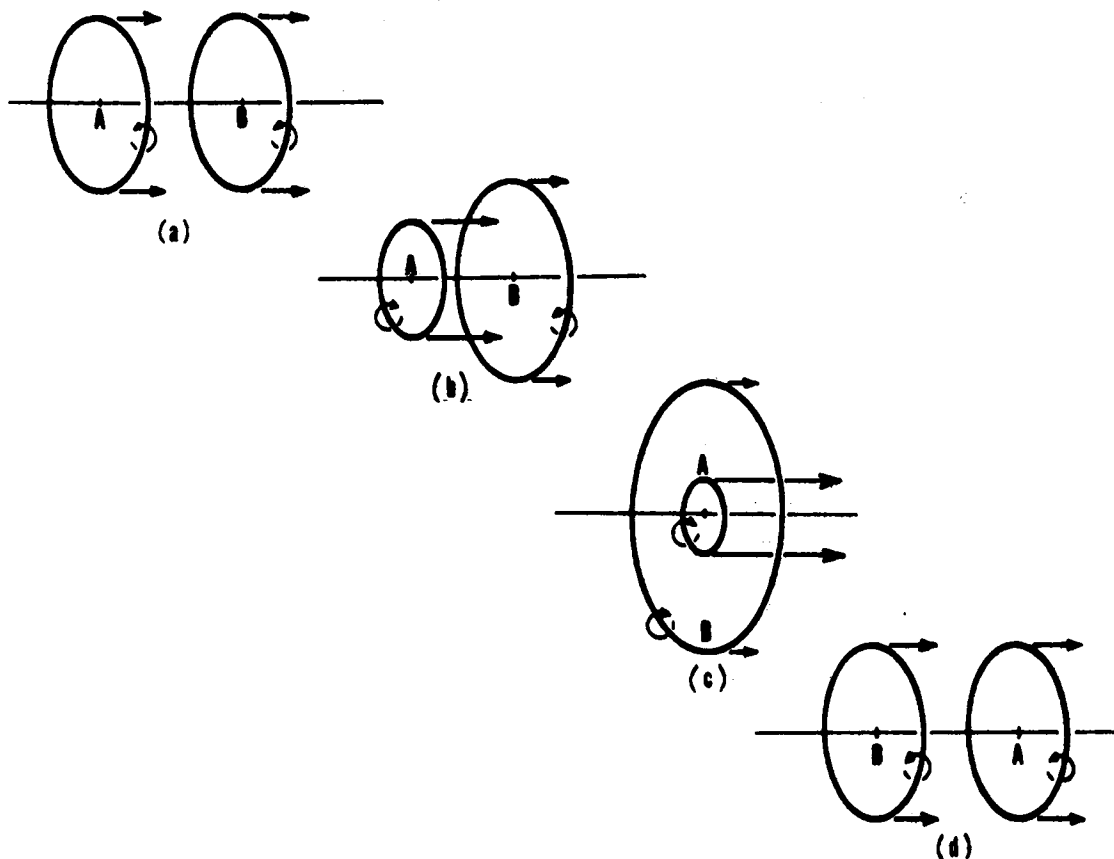


Figure 14. Leapfrog action of two free vortex rings

In the present method the propeller is assumed to have a large number of blades. The approaching flow to the propeller is to be steady and uniform, while the receding flow within the propeller wake is to be nonuniform. The wake is also assumed to be a three-dimensionally rigid and prescribed one consisting of a succession of ring vortices representing only the trailing

vortices, with the exception of the root trailing vortices, emanating from along the span of the blades. The root trailing vortices, which are simply rectilinear vortices coexisting along the propeller axis, would be the primary contributors to the angular motion of the slipstream, and there are basically two reasons for not including them in this method. The first and foremost reason is that the boundary layer method described earlier does not allow for crossflows on the body. Secondly, flow visualization studies indicate that the self-induced effects of the vorticity rapidly carry the root vortices up through the center of the slipstream where they are dissipated. It is further assumed that the remaining trailing vortices quickly roll up within a few chord lengths from the plane of the propeller to form a single concentrated vortex trailing from near the tip of each blade. This analytically-simplifying assumption is also verifiable from flow visualization studies.

Since the slipstream is to be rigidly prescribed, certain aspects must be considered for the proper location and strengths of the vortex rings. As stated earlier, the trailing vortices quickly roll up to form a single trailing vortex. It therefore seems plausible that in the plane of the propeller several concentric ring vortices, each of different radius and strength, may be specified, while fewer and fewer vortex rings may be specified further downstream. The location of the downstream vortices may be specified rather arbitrarily*, but their strengths should satisfy some mathematical requirement or some physical phenomenon. The laws of Helmholtz and Kelvin state that the circulation is conserved. In other words, if a plane of the slipstream contains two vortex

*An attempt should be made to approximate the results of momentum theory for propellers: i.e., the induced velocity in the ultimate wake be twice that in the plane of the propeller.

rings of circulation strengths Γ_1 and Γ_2 while another plane further downstream contains only one ring, then the strength of the single ring of the downstream plane must be $\Gamma_1 + \Gamma_2$. Under the present method, the strengths of the vortex rings may be arbitrarily specified, with the differences between their theoretical strengths and those actually used being accounted for by assuming some type of viscous dissipation.

The effect of a ring vortex at a sufficient distance from itself is approximately the same as that of a three-dimensional doublet of strength $1/2 \Gamma r^2$, where Γ is the strength of the vortex ring and r is its radius [10]. This statement results from the observation that as the distance from the ring vortex becomes greater and greater, the details of the ring's shape become less and less important. Since reductions in computational times are always desirable, the present method incorporates doublet flow whenever possible. The computational savings are quite substantial since the calculation of the velocity induced by a doublet does not require integration.

In order to apply doublet flow, its theory will be discussed briefly: Consider the situation where a source of strength q and a sink of equal strength are located a very small distance ℓ apart. Letting the distance ℓ go to zero while q is allowed to increase indefinitely in such a way that the product $q\ell$ remains finite and equal to a constant μ , then the potential at a point P due to this so-called *doublet* at \vec{s} is given by [Figure 15].

$$\begin{aligned}\phi(P) &= -\frac{1}{4\pi} \frac{\vec{\mu} \cdot \vec{r}}{|\vec{r}|^3} \\ &= -\frac{1}{4\pi} \frac{\vec{\mu} \cdot (\vec{R} - \vec{s})}{|\vec{R} - \vec{s}|^2}\end{aligned}$$

ORIGINAL PAGE IS
OF POOR QUALITY

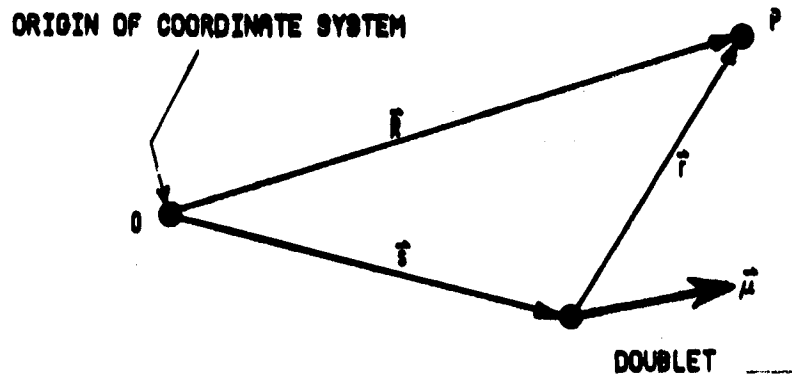


Figure 15. Doublet potential definition

where $\vec{\mu}$ is strength of the doublet in the direction of its axis. The positive doublet axis is simply the direction from the sink to the source.

The velocity field induced by a doublet is readily obtained from the equation

$$\vec{V} = \text{grad } \phi = -\frac{1}{4\pi} \text{grad} \left(\frac{\vec{\mu} \cdot \vec{r}}{r^3} \right).$$

The velocity components in Cartesian coordinates are thus

$$u = -\frac{\mu_x}{4\pi} \frac{-2r_x^2 + r_y^2 + r_z^2}{(r_x^2 + r_y^2 + r_z^2)^{5/2}}$$

$$v = -\frac{\mu_y}{4\pi} \frac{r_x^2 - 2r_y^2 + r_z^2}{(r_x^2 + r_y^2 + r_z^2)^{5/2}}$$

$$w = -\frac{\mu_z}{4\pi} \frac{r_x^2 + r_y^2 - 2r_z^2}{(r_x^2 + r_y^2 + r_z^2)^{5/2}}$$

where μ_x , μ_y , and μ_z are the doublet's strength in the x, y, z directions, respectively, and r_x , r_y , and r_z are the x, y, z components, respectively, of the vector \vec{r} (Figure 15).

The substitution of doublet flow for ring vortex flow requires that the origin of the doublet be the same as that of the ring vortex, the doublet axis be perpendicular to plane of the ring vortex and is directed so that the induced velocity is of the same sense as that of the ring vortex, and the doublet strength μ be a "suitable" function of the ring vortex strength Γ .

At sufficiently large distances from the origin of a doublet of strength $1/2 \Gamma r^2$, the induced velocity of the doublet approximates that of a ring vortex with its origin the same as that of the doublet. Unfortunately this doublet strength is only valid at large distances. In the present method, the doublet strength $1/2 \Gamma r^2$ was reduced by a factor of 0.00932 so that the velocity induced by the doublet closely matches that of a ring vortex of strength Γ at and beyond a distance of 1.5 times the diameter of the vortex ring (Figure 16). For all points at a distance greater than 1.5 times the vortex ring diameter, the induced velocity is calculated by the doublet flow equations. Otherwise, the vortex ring equations are used.

Since vortex filaments are discontinuities in an inviscid fluid, it is important that no filament intersects with the body's surface. Otherwise, extremely large induced velocities exist on the surrounding surface, as predicted by equations 13, 14, 17, 18, or 19 since $d \rightarrow 0$. In determining the potential flow solution of a body in the slipstream of a propeller, the present method calculates the diameters of the vortex rings so that no vortex intersects with the body and that the mass flow between the body and the

ORIGINAL PAGE IS
OF POOR QUALITY.

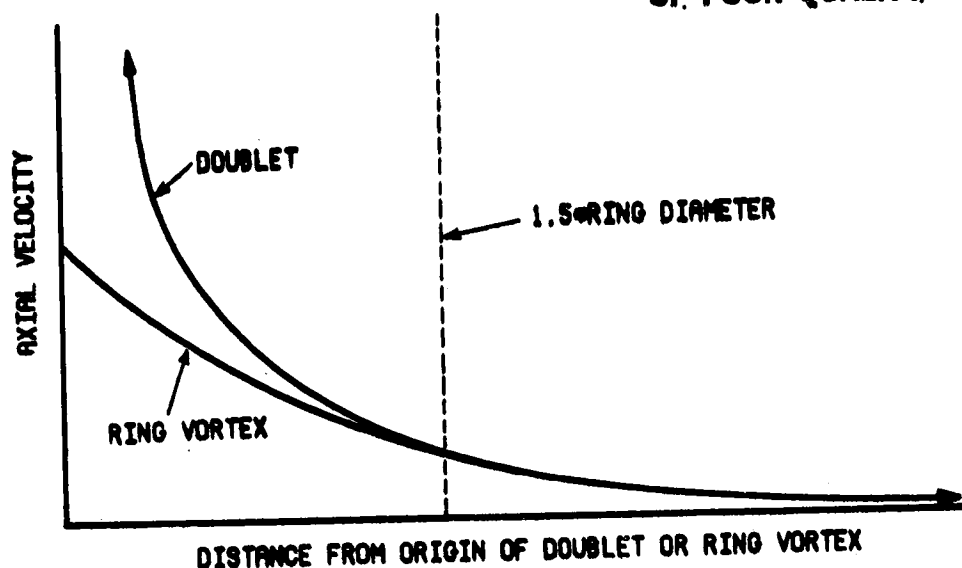


Figure 16. Matching doublet flow to vortex flow

boundary of the slipstream is constant. These requirements are sufficiently satisfied by the following procedure:

Each axial station of the body is described by a set of Cartesian points, each point having an identical x-coordinate value (Figure 17). In other words, an axial station is contained in a plane perpendicular to the x-axis. Assuming that each body cross-section is symmetrical about the x-z plane and contains the same number of points, only half of the total number of points must be supplied. The body must be closed at both ends, i.e., the first and last axial stations must not only contain the same number of points, each point of the same station must be equal.

For each axial station, the cross-sectional area is computed by summing the individual areas of plane triangles of the cross-section. Each plane triangle is defined by the origin of the cross-section and two consecutive points on the body's surface. The maximum distance and the average distance

ORIGINAL PAGE IS
OF POOR QUALITY

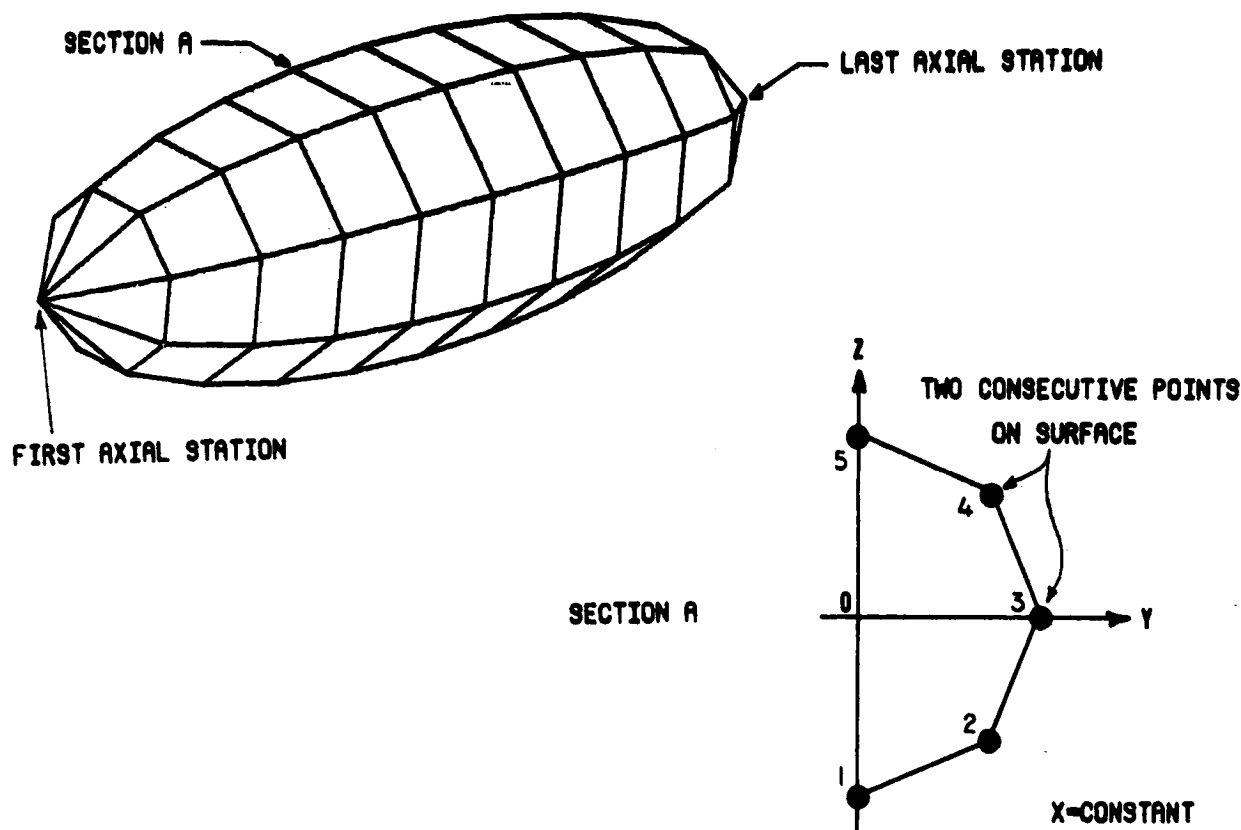


Figure 17. Denotation of first and last body axial station with illustration of point numbering

are also computed. The maximum distance is that from the origin to the farthest surface point, while the average distance is considered to be the radius of a circle equal in area as that of the cross-section of the body. With the maximum and average distances and the cross-sectional areas now known, an equivalent circular body is produced by letting the average distances be the radii of area-equivalent circles. This assumption allows for a crude, but sufficiently accurate*, method to satisfy the mass flow requirements and to guarantee that the vortex rings do not intersect with the body.

*The present method would not produce satisfactory flow fields for wide flat bodies with the equivalent circular-body concept. For these cases the use of an equivalent ellipsoidal-body concept along with elliptically-shaped vortices would be more suitable and realistic.

Consider an equivalent circular body within a slipstream (Figure 18a) and a typical cross-section (Figure 18b). The mass flow at the beginning of the slipstream is given by

$$\rho \pi d^2 V / 4$$

where ρ is the density of the fluid, V is the mass-mean velocity of the fluid across the cross-section, and d is the diameter of the circular slipstream at its beginning. Similarly, the mass flow in an annular ring is given by

$$\rho \pi (a^2 - z^2) V$$

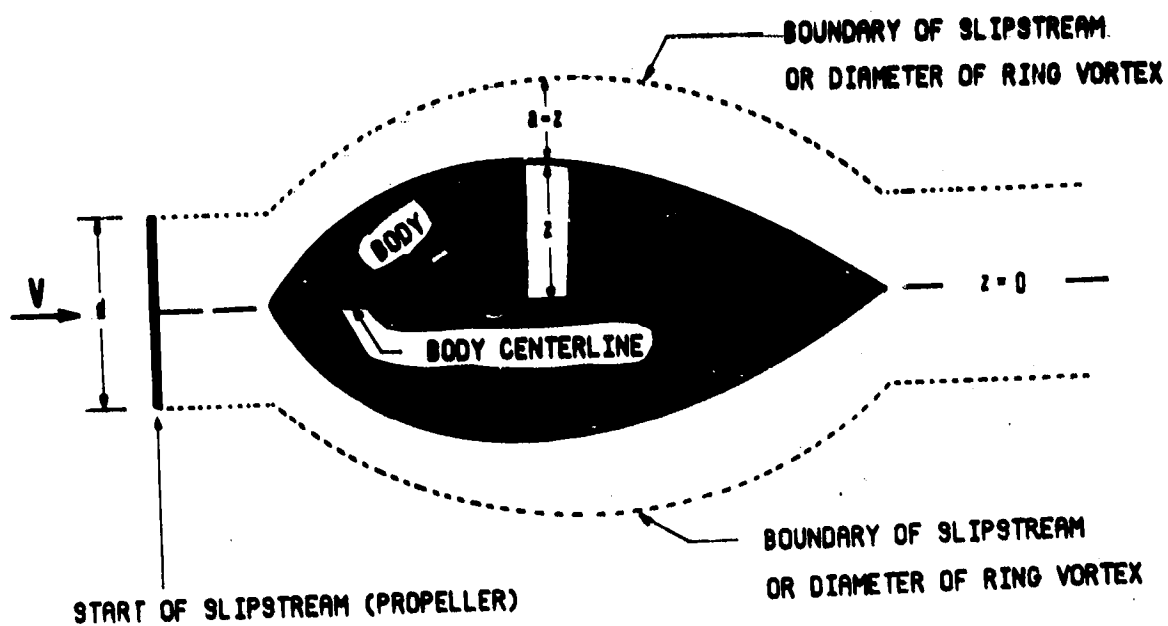
where a is the distance from the body centerline to the boundary of the slipstream, and z is the distance from the body centerline to the body surface. Requiring that these two mass flows be equal, it is found that the diameter of the vortex ring (or the boundary of the slipstream) must be given by

$$a = \sqrt{d^2/4 + z^2} \quad (21)$$

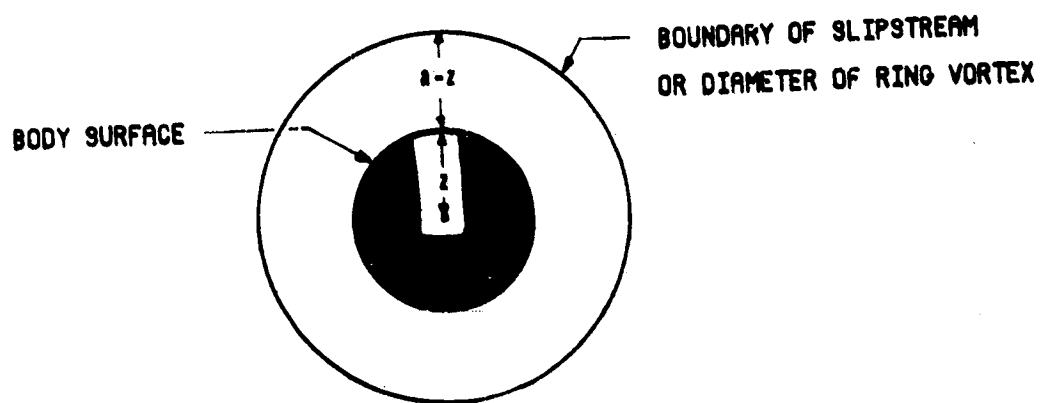
As the body radius z varies, the diameter of the vortex ring varies accordingly. It should be noted that this is another way of saying that the radius and circulation were changed in such a way that the velocity induced on the body surface is the same as that at $z = 0$ if the body were not present.

The origins of the various ring vortices may be assigned arbitrarily along the centerline of the body. Therefore, appropriate averages of the relative distances and areas must be calculated not only to suitably fair the given cross-sections, but to determine the diameters of the vortices.

ORIGINAL PAGE IS
OF POOR QUALITY.



(a)



(b)

Figure 18. Equivalent circular body

Even though equation (21) satisfies the continuity requirements at each position along the body, it does not guarantee that the vortex rings do not intersect with the body because of the assumption of the equivalent circular body. To eliminate this problem, a comparison is made between the diameters calculated by equation (21) and the maximum diameters of the original body. The largest diameter is always used. At this point it is clear that if the cross-sections of the original body is greatly different from circular ones, the present method may not be sufficiently accurate for the mass flow calculations.

The method also has an automated procedure to generate additional vortex rings about and aft of a body by using exponential functions to assign the locations of their origins. The exponential functions are in turn expressions of the varying body dimensions. These functions may be terminologically defined as "weak forcing function" since their detailed behaviors are body-dependent, while their broad overall behaviors are set a priori. Basically, the method contains two such functions: one relevant from the start of the slipstream to the plane of maximum body width, and the other relevant from the maximum body-width plane to the assigned maximum axial extent of the vortices. Figure 19 depicts a vortex ring distribution and diameter variation about an aircraft fuselage in the wake of a propeller.

As may be evident from the discussion above, accurate modeling of a propeller's wake or slipstream is a very difficult task. Such a physico-mathematical model would necessarily be unduly elaborate (for the use intended here) and its computational requirements enormous. Since a major objective of the present work is to simulate the effects of the nonuniform flow field

ORIGINAL PAGE IS
OF POOR QUALITY

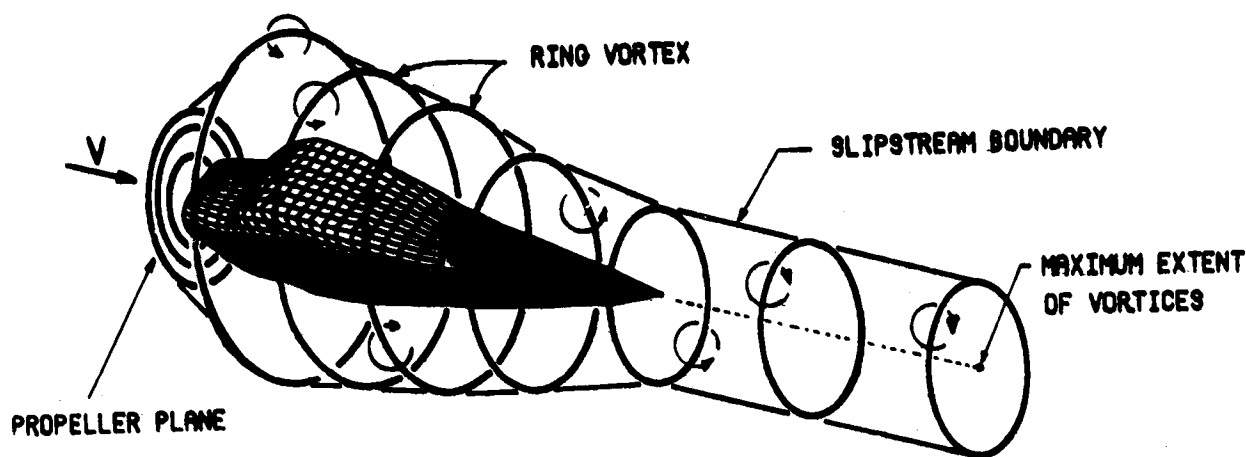


Figure 19. Vortex-ring distribution and diameter variation about an aircraft fuselage in the wake of a propeller

of a propeller-like wake within the context of the inviscid potential flow calculations over a three-dimensional body, accurate modeling does not seem to be warranted. Although no claims of accuracy are professed for this wake analysis, it would seem to provide at least some insights into the flow behavior within a slipstream.

FLOW PORT LOCATIONS FOR MINIMUM DRAG AND EFFECTIVE ENGINE COOLING

Properly-located air intake and exhaust sites provide adequate cooling and carburetor induction and minimum pressure loss. Since the pressure loss (or "cooling" drag) is larger than necessary in many general aviation designs, the present method can be directed to determine cowl air intakes and exhaust sites that produce favorable interactions with the external flows and also provide good entrapment and extraction of cooling air. Favorable interactions with external flows may be interpreted as those where the inlet will capture sufficient cooling and carburetor air mass with a minimum disruption to the external flow and the exhaust will provide adequate extraction and contribute, if possible, to the streamlining of the aircraft.

In this analysis the flow is assumed to be incompressible and its free-stream velocity equal to unity. It is also assumed that a suitable schematic of the cowl interior of a body with inlet and exhaust flow may be given by Figure 20. In this figure and in the following equations, C_{p_x} and $C_{p_{xx}}$ denote interior pressure coefficients and EOA denotes the effective orifice area.

An interior pressure coefficient may be defined as the pressure coefficient required to balance the mass flows between the inlet and exhaust. In the absence of an engine, the interior pressure coefficient is constant everywhere throughout the cowl interior. Since an engine occupies a large region of the interior, it obstructs the mass flow with its presence felt throughout the interior. A pressure drop will therefore arise between the pressure just inside the flow inlet and that just inside the flow exhaust as a result of

ORIGINAL PAGE IS
OF POOR QUALITY

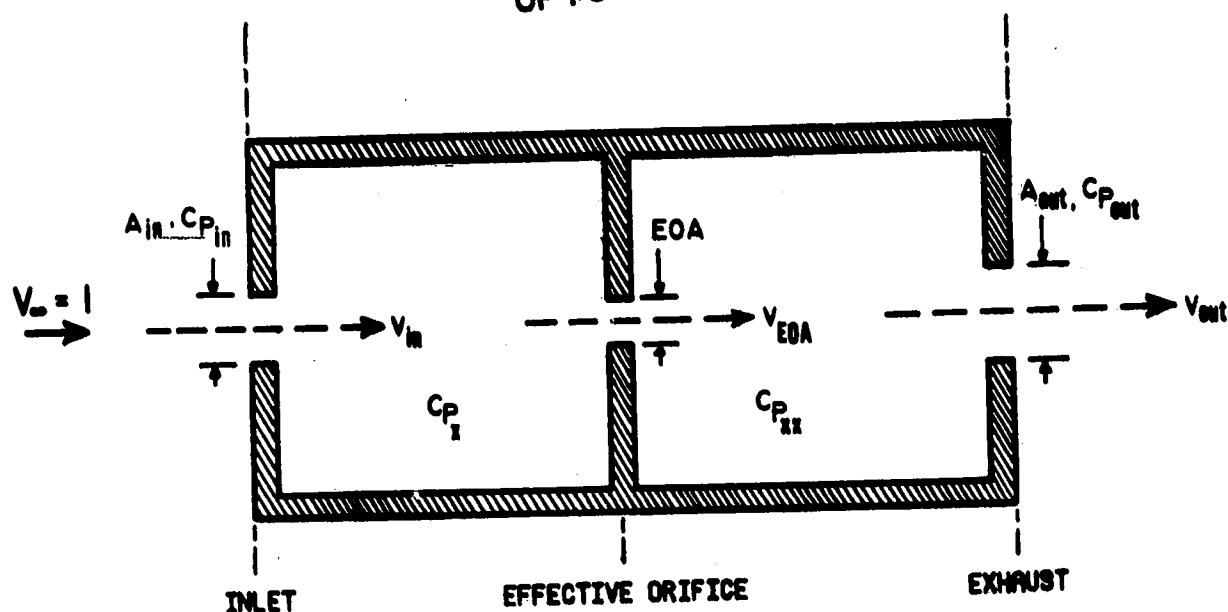


Figure 20. Schematic of cowl interior

viscous losses incurred by the fluid as it moves through the engine fins and around baffles. With an engine present, two "different" interior pressure coefficients are thus necessary to include the effects of engine fin and baffle pressure drops.

The effective orifice area depends directly on the engine geometry and the "tightness" of the engine inside the cowl. The tightness of an engine inside the cowl refers to the spacing between the cowl and engine. If this space exists, air mass will tend to leak around (or about) the engine instead of flowing through its fins and baffles and, therefore, reducing the cooling capacities of the air flow. With the assumption of a tight engine, the effective orifice area is that "area" seen by the mass flow through the fins and baffles to provide engine cooling. Without the assumption, the effective orifice area must be some compromise of the leakage and cooling flows.

From Figure 20, the mass flow \dot{m} at each opening must be given by

$$\dot{m} = \rho AV \quad (22)$$

where ρ , A , and V are the fluid density, the cross-sectional area, and the fluid velocity normal to the opening, respectively. Since mass is conserved the mass flow at each opening must be equal. That is,

$$\dot{m} = \rho \cdot A_{in} \cdot V_{in} = \rho \cdot EOA \cdot V_{EOA} = \rho \cdot A_{out} \cdot V_{out} = \text{constant} \quad (23)$$

By Bernoulli's equation for incompressible flow,

$$p_{\infty} + \frac{\rho}{2} V_{\infty}^2 = p + \frac{\rho}{2} V^2 \quad (24)$$

where p_{∞} and V_{∞} denote the reference freestream pressure and velocity, respectively. Rearranging (24) and dividing by the reference dynamic pressure ($1/2 \rho V_{\infty}^2$) yields the pressure coefficient

$$C_p = \frac{p - p_{\infty}}{1/2 \rho V_{\infty}^2} \quad (25)$$

For incompressible flows, the dynamic pressure is simply a difference of two pressures. Thus,

$$\text{Dynamic pressure} = 1/2 \rho V^2 = \Delta p = p_2 - p_1 = \text{pressure difference}$$

or

$$V^2 = \frac{2}{\rho} [p_2 - p_1] \quad (26)$$

Subtracting p_{∞} from p_2 and adding p_{∞} to p_1 of (26) yields

$$V^2 = \frac{2}{\rho} [(p_2 - p_{\infty}) - (p_1 - p_{\infty})] \quad (27)$$

Multiplying and dividing the right-hand side of (27) by V_{∞}^2 produces

ORIGINAL PAGE IS
OF POOR QUALITY

$$v^2 = v_\infty^2 \left[\frac{(p_2 - p_\infty)}{1/2 \rho v_\infty^2} - \frac{(p_1 - p_\infty)}{1/2 \rho v_\infty^2} \right]$$

$$= v_\infty^2 [Cp_2 - Cp_1]$$

or

$$v = v_\infty \sqrt{Cp_2 - Cp_1} \quad (28)$$

Thus, equation (28) relates the velocity normal to an opening with the pressure coefficients on each side of the opening.

At this point it is important to recapitulate on the representation of the body and to define parameters pertinent for the continuance of this method. As stated in the previous sections and shown in Figure 3, the three-dimensional body is constructed of an orderly arrangement of plane quadrilaterals or panels. This body representation facilitates the assignment of the inlet and exhaust sites because any panel or combination of panels may be declared as either inlet openings or exhaust openings. Since stagnation flows are not considered, a body with an inlet site must, in turn, have an exhaust site.

The total inlet area A_{in} is assumed to be the sum of the individual inlet panel areas, while the total exhaust area A_{out} is assumed to be the sum of the individual exhaust panel areas. Since the interior of the body (or cowl) is treated essentially as a black box, it is necessary to propose a single inlet pressure coefficient Cp_{in} and a single exhaust pressure coefficient Cp_{out} . These pressure coefficients are surmised to be area-averaged values of the relevant pressure coefficients of the selected inlet and exhaust panels from a solid-body (no inlet or exhaust) potential flow solution. That is,

ORIGINAL PAGE IS
OF POOR QUALITY

$$C_{p_{in}} = \frac{\sum_{i=1}^{\text{Inlets}} A_i C_{p_i}}{\sum_{i=1}^{\text{Inlets}} A_i}$$

and

$$C_{p_{out}} = \frac{\sum_{i=1}^{\text{Exhausts}} A_i C_{p_i}}{\sum_{i=1}^{\text{Exhausts}} A_i}$$

The solid-body pressure coefficients are implied to remain equal for the opened body. This implication is only valid if the inlet and exhaust panel geometries are relatively small compared to the overall body geometry. For this reason a "grid" refinement may be necessary to accurately model or shape the body particularly in the neighborhood of the inlet/exhaust areas.

It is now possible to rewrite (23) by using (28). Hence, ($V_\infty = 1$)

$$\rho A_{in} \sqrt{C_{p_{in}} - C_{p_x}} = \rho EOA \sqrt{C_{p_x} - C_{p_{xx}}} = \rho A_{out} \sqrt{C_{p_{xx}} - C_{p_{out}}}$$

or

$$A_{in} \sqrt{C_{p_{in}} - C_{p_x}} = EOA \sqrt{C_{p_x} - C_{p_{xx}}} = A_{out} \sqrt{C_{p_{xx}} - C_{p_{out}}} \quad (29)$$

To eliminate the square root, each "term" of (29) is squared:

$$\begin{array}{ccc} \textcircled{1} & \textcircled{2} & \textcircled{3} \\ A_{in}^2 (C_{p_{in}} - C_{p_x}) & = EOA^2 (C_{p_x} - C_{p_{xx}}) & = A_{out}^2 (C_{p_{xx}} - C_{p_{out}}) \end{array} \quad (30)$$

The rearrangement of terms $\textcircled{1}$ and $\textcircled{2}$ of equation (30) yields

ORIGINAL PAGE NO.
OF POOR QUALITY

$$A_{in}^2 Cp_{in} - Cp_x (A_{in}^2 + EOA^2) = -EOA^2 Cp_{xx} \quad (31)$$

while the rearrangement of terms (2) and (3) yields

$$-A_{out}^2 Cp_{out} + Cp_{xx} (A_{out}^2 + EOA^2) = EOA^2 Cp_x \quad (32)$$

Upon solution of equations (31) and (32),

$$Cp_{xx} = \left\{ A_{out}^2 Cp_{out} + \frac{EOA^2 \cdot A_{in}^2 \cdot Cp_{in}}{A_{in}^2 + EOA^2} \right\} \frac{A_{in}^2 + EOA^2}{A_{in}^2 \cdot A_{out}^2 + EOA^2 (A_{in}^2 + A_{out}^2)} \quad (33)$$

and

$$Cp_x = \frac{A_{in}^2 Cp_{in} + EOA^2 Cp_{xx}}{A_{in}^2 + EOA^2} \quad (34)$$

Equations (33) and (34) satisfy the limiting conditions of the effective orifice area:

$$(1) \quad EOA = 0 \quad Cp_{xx} = Cp_{out}, \quad Cp_x = Cp_{in}$$

$$(2) \quad EOA \rightarrow \infty \quad Cp_{xx} \approx Cp_x$$

The first condition implies complete flow blockage or no mass flow, while the second condition implies essentially unrestricted mass flow.

Since the engine is far less than 100 percent efficient, it is necessary in a constant density representation to add to the cooling flow a quantity representing the internal heat addition to the air mass. This quantity is assumed to be physically represented by the difference between the maximum energy content of the fuel being used and the actual energy converted to

ORIGINAL PAGE IS
OF POOR QUALITY

kinetic energy (developed engine power). The energy difference is surmised to be transferred to the surroundings directly in the form of heat which in turn leads to an increase in temperature.

The heat quantity Q is equal to the change in enthalpy H ; i.e.,

$$Q = \Delta H \quad (35)$$

Assuming that air is an ideal gas and the temperature variation is relatively small,

$$\Delta H = mC_{p_{air}}\Delta T \quad (\text{constant-pressure process}) \quad (36)$$

where m is the air mass, $C_{p_{air}}$ is the constant-pressure specific heat of air, and ΔT is the temperature difference. In terms of their rates, equation (35) becomes

$$\dot{Q} = \Delta \dot{H} ,$$

while equation (36) becomes

$$\Delta \dot{H} = \dot{m}C_{p_{air}}\Delta T .$$

Thus

$$\dot{Q} = \Delta \dot{H} = \dot{m}C_{p_{air}}\Delta T$$

or

$$\Delta T = \frac{\dot{Q}}{\dot{m}C_{p_{air}}} \quad (37)$$

Dividing (37) by the reference temperature T_{∞} yields

$$\frac{\Delta T}{T_{\infty}} = \frac{T - T_{\infty}}{T_{\infty}} = \frac{\dot{Q}}{\dot{m}C_{p_{air}}T_{\infty}} \quad (38)$$

ORIGINAL PAGE IS
OF POOR QUALITY

The heat transfer \dot{Q} is now assumed to be

$$\dot{Q} = H_f \cdot \text{ffr} - P$$

where H_f is the heat of combustion of the fuel, ffr is the fuel flow rate, and P is the developed engine power. The fuel flow rate, though, is the product of the specific fuel consumption c and the developed engine power:

$$\text{ffr} = c \cdot P$$

The mass flow rate \dot{m} is by definition equal to equation (22) where ρ is taken to be the freestream density, A the total inlet area A_{in} , and V the velocity normal to the inlet ($= V_{\infty} \sqrt{Cp_{in} - Cp_x}$). Therefore, equation (38) now becomes

$$\frac{T - T_{\infty}}{T_{\infty}} = \frac{P[H_f \cdot c - 1]}{\rho_{\infty} T_{\infty} Cp_{air} V_{\infty} \sqrt{Cp_{in} - Cp_x}}$$

or

$$\frac{T}{T_{\infty}} = \frac{P[H_f \cdot c - 1]}{\rho_{\infty} T_{\infty} Cp_{air} V_{\infty} \sqrt{Cp_{in} - Cp_x}} + 1 \quad (39)$$

Air has been assumed to be an ideal gas, and hence any increase in its temperature decreases its density. Since the incompressible theory on which this method is based assumes a constant density, the internal heat release must be represented by a compensating increase in the flow velocities in order to balance the mass flows. This compensation may be accomplished by varying the effective orifice area which, consequently, varies the effective flow velocities. The effective orifice area variation is determined as follows: The mass flow rate in the effective orifice region is given by (22) where A is the effective orifice area EOA and V is determined from (26) to be

ORIGINAL PAGE IS
OF POOR QUALITY

$$v = \sqrt{\frac{2\Delta p}{\rho_{\infty}}} \quad (40)$$

The density change with temperature for an ideal gas is given by the equation of state to be

$$\frac{\rho_1}{\rho_{\infty}} = \frac{T_{\infty}}{T_1}$$

or

$$\rho_1 = \rho_{\infty} \frac{T_{\infty}}{T_1} \quad (41)$$

A "new" mass flow rate \dot{m}_1 is calculated by assuming the density of (22) and (40) to be the density ρ_1 of (41):

$$\dot{m}_1 = \left(\rho_{\infty} \frac{T_{\infty}}{T_1} \right) EOA \sqrt{\frac{2\Delta p}{(\rho_{\infty} T_{\infty}/T_1)}}$$

or

$$\dot{m}_1 = \left\{ \rho_{\infty} EOA \sqrt{\frac{2\Delta p}{\rho_{\infty}}} \right\} \sqrt{\frac{T_{\infty}}{T_1}} \quad (42)$$

The mass flow rate (42) is seen to be the product of the original orifice flow rate and the square root of the temperature ratio T_{∞}/T_1 . Associating the temperature ratio with the original orifice area produces a new effective orifice area

$$EOA_{NEW} = EOA \sqrt{\frac{T_{\infty}}{T_1}}$$

Applying EOA_{NEW} to equations (33) and (34), new interior pressure coefficients are calculated. With $T_1 > T_\infty$ (heat added),

$$EOA_{NEW} < EOA.$$

Consequently, the flow velocities must vary in a constant density analysis in order to balance the mass flows.

The typical behaviors of the interior pressure coefficients due to variations in the freestream density, the inlet velocity, the freestream temperature, or the effective orifice area are shown in Figure 21a, while those due to variations in the fuel's heat of combustion, the specific fuel consumption, or the developed engine power are shown in Figure 21b.

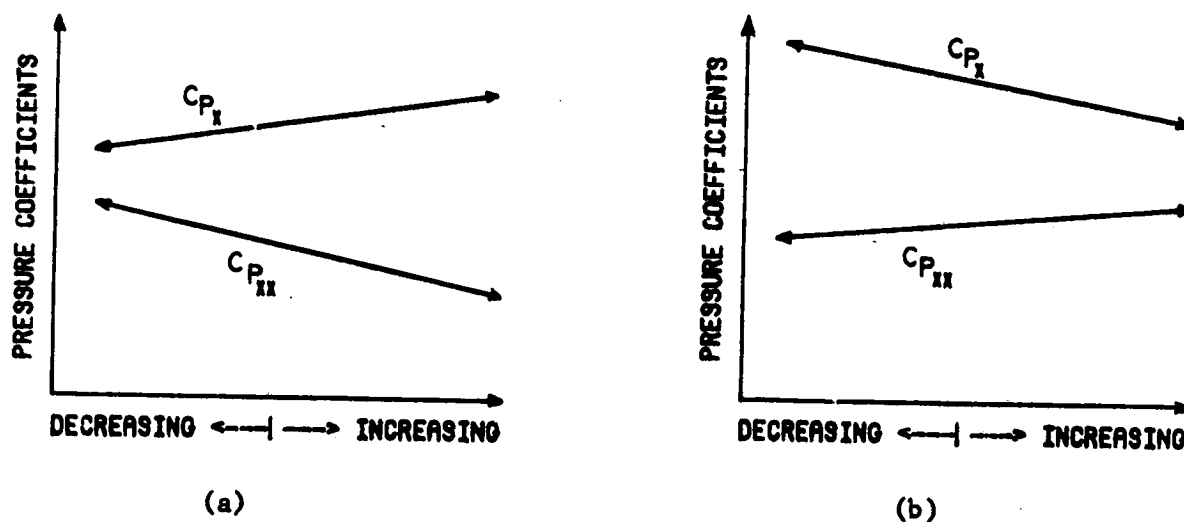


Figure 21. Typical behaviors of the interior pressure coefficients with parameter variation.

On a percent basis, a variation in the effective orifice area or the specific fuel consumption had the most pronounced effect on C_{p_x} and $C_{p_{xx}}$. Not only does Figure 21 indicate the slopes of the "lines" representing C_{p_x} and $C_{p_{xx}}$,

it should be noticed that a measure of the "driving potential" of the air mass can be observed. This "driving potential" or pressure difference of Figure 21a is seen to become smaller with increasing values of the pertinent parameters, while that of Figure 21b is seen to become greater with increasing values of its pertinent parameters. Consequently, a measure of control over the quantity of air flow is possible by a strategic selection of the parameters.

It is now possible to calculate the normal velocities on the specified inlet and exhaust panels and apply them as the complementary boundary conditions for the potential flow calculations. The normal velocities on the inlet and exhaust panels are surmised to be functions of the interior pressure coefficients and the pressure coefficients that existed on those panels when the body was closed (with no internal mass flow). Thusly,

$$V_i = V_\infty \sqrt{C_{p_i} - C_{p_x}} \quad (43)$$

for the inlet panels and

$$V_i = V_\infty \sqrt{C_{p_{xx}} - C_{p_i}} \quad (44)$$

for the exhaust panels, where C_{p_i} is panel i 's closed-body pressure coefficient and $V_\infty (= 1)$ is the freestream velocity. Attributable to the proposition of a single inlet pressure coefficient $C_{p_{in}}$ and a single exhaust pressure coefficient $C_{p_{out}}$ in the determination of C_{p_x} and $C_{p_{xx}}$, the discriminants of (43) and (44) is occasionally negative. This difficulty of imaginary numbers is eliminated by proposing that (43) and (44) are essentially

$$V_i = V_\infty \sqrt{|C_{p_i} - C_{p_x}|} \quad (45)$$

for the inlet panels and

$$V_1 = V_\infty \sqrt{C_{p_{xx}} - C_{p_1}} \quad (46)$$

for the exhaust panels. The normal velocities of (45) and (46) are assumed to be the complementary boundary conditions for the potential flow solution discussed earlier. These normal velocities are inserted into (8) as the now-known function F .

In summary, the mass flow of air through a body is dependent in this treatment upon (a) the pressures which existed when the inlet and exhaust panels were closed, (b) any internal pressure drops due to engine fins and baffles, (c) the internal heat addition, and (d) the area ratios of the inlet, the effective orifice, and the exhaust. The present method consists basically of the following steps:

- (1) Panels are chosen to represent the inlet and exhaust sites.
- (2) The total inlet and exhaust areas are determined by summing the individual areas.
- (3) An area-averaged pressure coefficient is calculated for the inlet site and the exhaust site.
- (4) Internal heat addition is invoked through appropriate changes in the effective orifice area.
- (5) The interior pressure coefficients are determined, and the normal velocities on each individual inlet and exhaust panels are calculated.

A GRID REFINEMENT SCHEME FOR MODIFICATION OF A BODY'S GEOMETRIC DATA

Since the preparation or modification of the geometric data of a three-dimensional body for input into a potential-flow program is tedious and time-consuming, a scheme has been developed to simplify this task. Given a set of Cartesian-coordinate data descriptive of the body, this scheme may be used to correct body misrepresentations, to change the body geometry, to refine the network (or grid) of the panels or quadrilaterals that form the surface of the body, and to plot various orthographic, perspective, and stereoscopic views of the original and the modified body.

The general procedure for specifying (or inputting) body points is the same as that given in Reference 4 for the NCSU BODY program. For clarity, this procedure is now reviewed:

The body's surface is constructed by an arrangement of quadrilaterals with their corner points forming a network of intersecting lines to be called, from this time on, M-lines and N-lines (Figure 22). The M-lines are those connecting corresponding points on the N-lines and are generally those running along in a direction near to that of the major body axis, while the N-lines are those surrounding the perimeter of the body in parallel planes perpendicular to the major body axis. Every N-line or M-line must have the same number of "defining" points as every other N-line or M-line with the stipulation that no N-line crosses another N-line and no M-line crosses another M-line, although they may converge to a common point.

Since the primary purpose of the scheme is to generate data compatible to the NCSU BODY program and the present report's potential-flow program which

ORIGINAL PAGE IS
OF POOR QUALITY

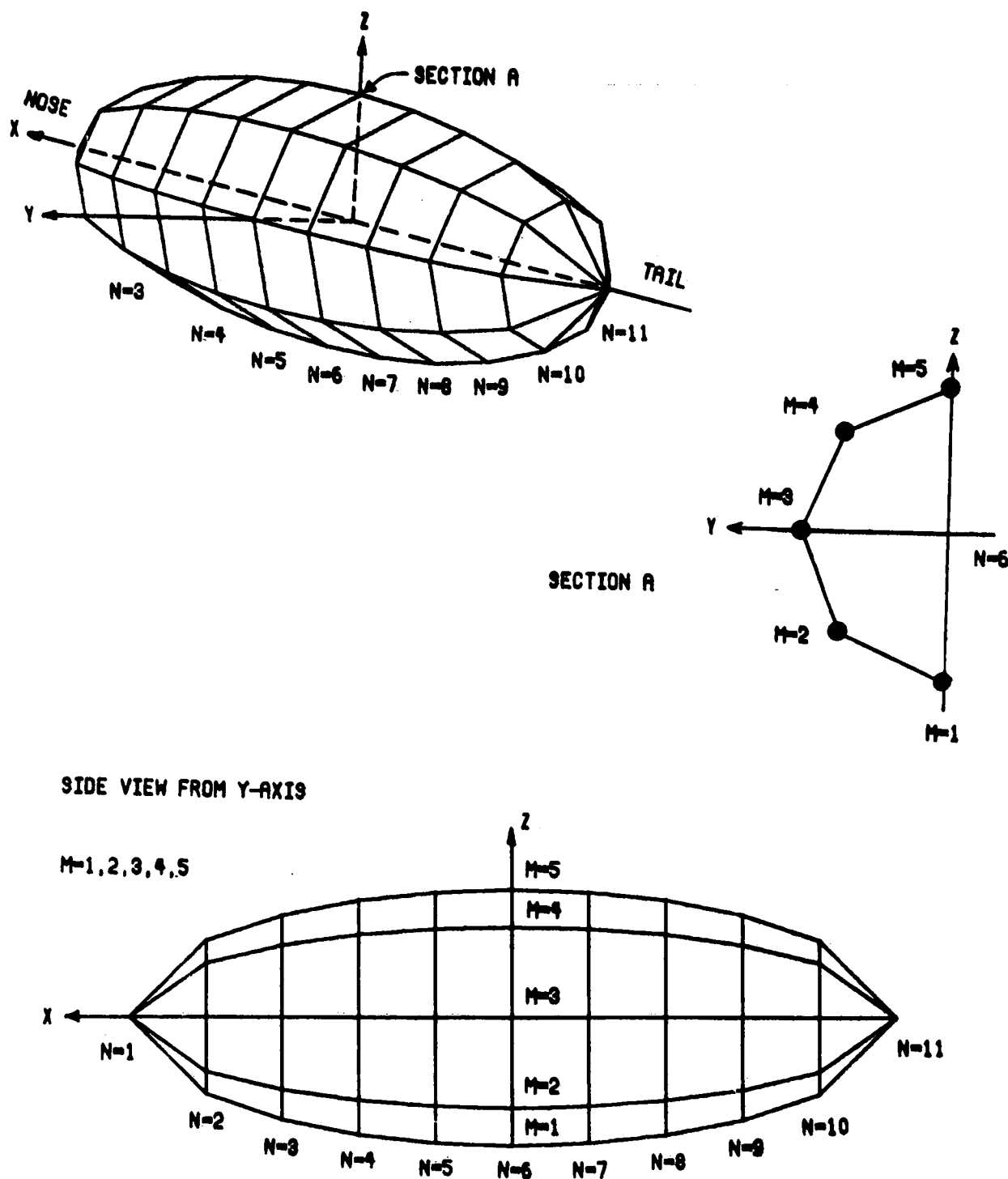


Figure 22. Schematic of indexing scheme used for a 3-1 ellipsoid with 40 panels describing the half-body

assumes the body is symmetrical about the X-Z plane, only half of the body is necessary for input. For compatibility, the first N-line must be that at the front of the body (first to encounter freestream air flow) with the remaining N-lines numbered consecutively from front to back. The points on each N-line are ordered such that the first point lies in the lower portion of the X-Z plane at the "bottom" of the body (Figure 22, Section A) with the remaining points consecutively increasing counter-clockwise (looking aft) to the upper portion of the X-Z plane at the "top" of the body. These points, i.e., the corresponding points on successive N-lines, generate the M-lines.

The workhorse of this scheme is a cubic-spline curve-fitting method [11] coupled to a coordinate-system rotation-translation technique. Although cubic-spline fits are generally considered to be the smoothest of all curve fits [12], they often have difficulty in regions of extremely high curvature, where oscillations become magnified. Splining points against arc length alleviates the oscillations; the present investigators, however, chose to remove the oscillations by rotating and translating the body points in the reference coordinate system to points in the new coordinate system.

As an illustration of the rotation and translation of the body points, consider the upper M-line* of the X-Z plane for some typical three-dimensional body (Figure 23). A curve fit of the points 1 through 23 - with their values given with respect to the reference coordinate system XYZ - may not be satisfactory between points 1, 2, and possibly 3 due to the presence of the high

*A three-dimensional body contains two M-lines in the X-Z plane - an upper one and a lower one. Since M-lines are increasingly numbered consecutively from the body's bottom to its top, the upper M-line corresponds to the maximum-number M-line whereas the lower M-line corresponds to the minimum-number M-line.

ORIGINAL PAGE IS
OF POOR QUALITY

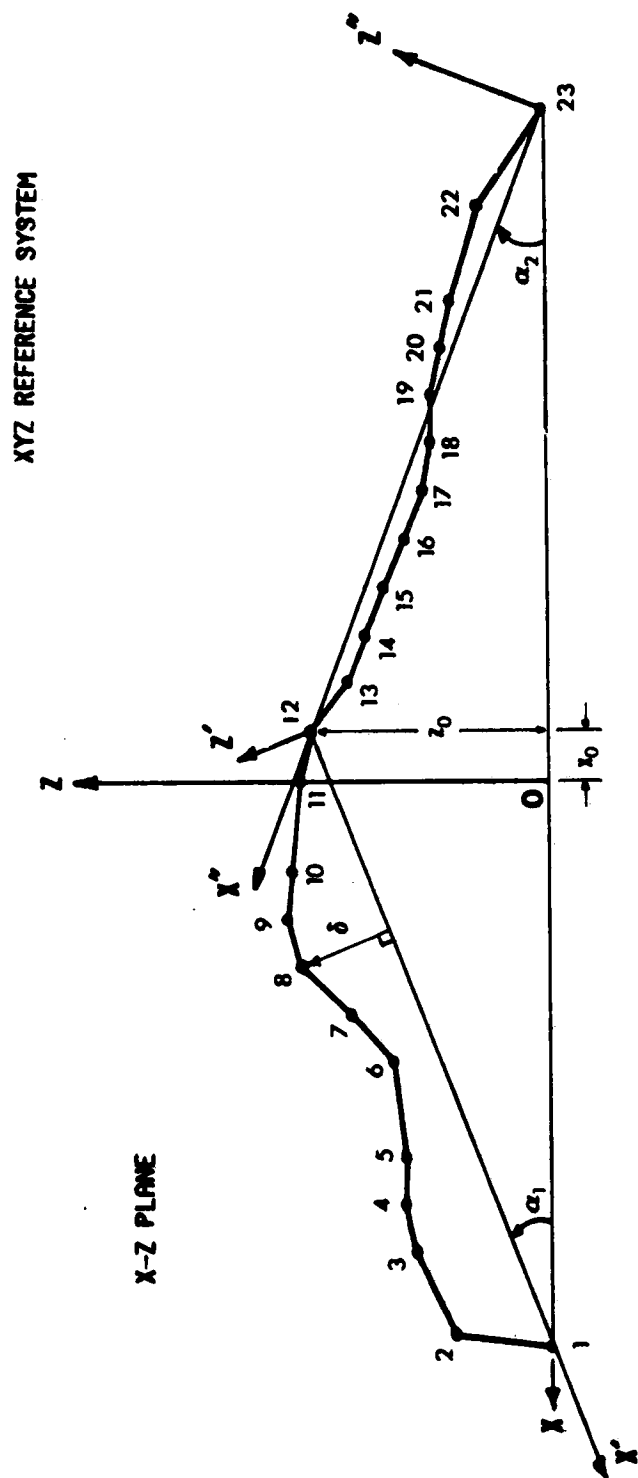


Figure 23. Typical translation and rotation scheme of reference coordinate system

ORIGINAL PAGE IS
OF POOR QUALITY

slope between points 1 and 2. The alternative procedure is to transform the body points to those appropriate to the new coordinate systems. For instance, for the transformation of points 1 through 12 to those in the $X'Y'Z'$ system, the following equations may be used:

$$X'_1 = (X_1 - X_{12})\cos \alpha_1 + (Z_1 - Z_{12})\sin \alpha_1 \quad (47)$$

$$Z'_1 = (Z_1 - Z_{12})\cos \alpha_1 - (X_1 - X_{12})\sin \alpha_1 \quad (48)$$

where

$$\alpha_1 = \tan^{-1} \left[\frac{Z_1 - Z_{12}}{X_1 - X_{12}} \right], \quad i = 1, 2, \dots, 12$$

For the transformation of points 12 through 23 to those in the $X''Y''Z''$ system, the following equations may be used:

$$X''_1 = (X_1 - X_{12})\cos \alpha_2 + (Z_1 - Z_{12})\sin \alpha_2 \quad (49)$$

$$Z''_1 = (Z_1 - Z_{12})\cos \alpha_2 - (X_1 - X_{12})\sin \alpha_2 \quad (50)$$

where

$$\alpha_2 = \tan^{-1} \left[\frac{Z_{12} - Z_{23}}{X_{12} - X_{23}} \right], \quad i = 12, 13, \dots, 23$$

The (X'_1, Z'_1) and (X''_1, Z''_1) points are curve-fitted and additional points are generated. Since these points must be transformed back to the reference system, equations (47) and (48) are solved for X_j and Z_j yielding

$$X_j = X'_j \cos \alpha_1 - Z'_j \sin \alpha_1 + X_{12}$$

$$Z_j = X'_j \sin \alpha_1 + Z'_j \cos \alpha_1 + Z_{12}$$

ORIGINAL PAGE IS
OF POOR QUALITY

while equations (49) and (50) are solved for X_k and Z_k yielding

$$X_k = X_k'' \cos \alpha_2 - Z_k'' \sin \alpha_2 + X_{12}$$

$$Z_k = Z_k'' \sin \alpha_2 + Z_k'' \cos \alpha_2 + Z_{12}$$

where the subscripts j and k denote appropriate, but different, point counters.

Often during the preparation of data, errors are made either during the process of keypunching the data or through the lack of a clear visual or mental conception of the body's shape, which may be disastrous to the potential-flow calculations. These errors in the input are difficult to recognize until the data is plotted.

The present method contains three techniques (options) to effectually correct these mistakes in a simple fashion. The first option modifies the data by explicitly changing the coordinates of individual originally-inputted body points through additionally-supplied coordinate information. By the second option, a body point P is replaced either by the average of the two points 1 and 2 (Figure 24a) of the M -line intersecting point P , the average of the two points 1 and 2 (Figure 24b) of the N -line intersecting point P , or the average of the four points 1, 2, 3, and 4 (Figure 24c) of the P -intersecting M - and N -lines. The third option uses the same point-identification arrangement as that of the second option, but replaces a body point P by linear interpolation(s). Utilizations of these options are shown in Figure 25 for a body assumed to be significantly in error at one point.

The present method incorporates two more geometry-related options to aid in the refinement of the grid network. These options are important since the panel geometries of the inlet and exhaust sites must be relatively small

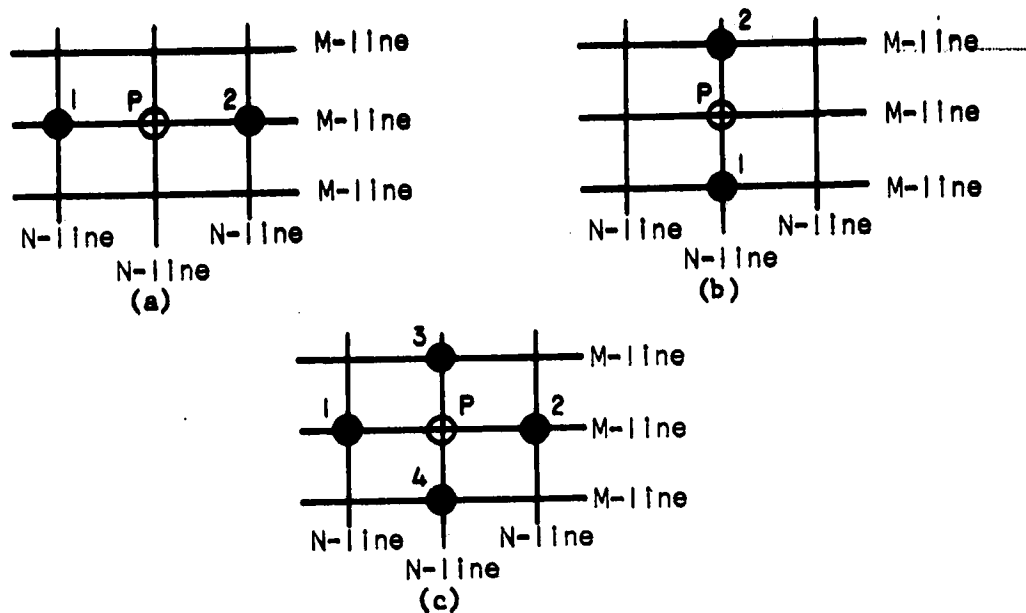


Figure 24. Coordinate information for averaging techniques

compared to the overall body geometry to allow for the assumption that the opened-body pressure coefficients (see previous section) to remain essentially equal to those of the closed body. The first of these options augments the number of M-lines and/or N-lines by equally distributing the user-specified number of additional M- and/or N-lines along the arc length (assumed to be the linear distance) of every two successive M-lines for additional M-lines and along the perpendicular distance of every two successive N-lines for additional N-lines. The points on the additional M- and N-lines (equal in number and order to those on the original M- and N-lines) are calculated by cubic-polynomial spline-fit interpolations. This scheme, to be called the "equal-line augmentation", should be recognized to have the ability to increase the number of quadrilaterals (panels) manifold with a corresponding decrease in the individual panel areas (Figure 26). Although potential-flow calculations become more and more accurate as more and more panels are used to describe a

ORIGINAL PAGE IS
OF POOR QUALITY

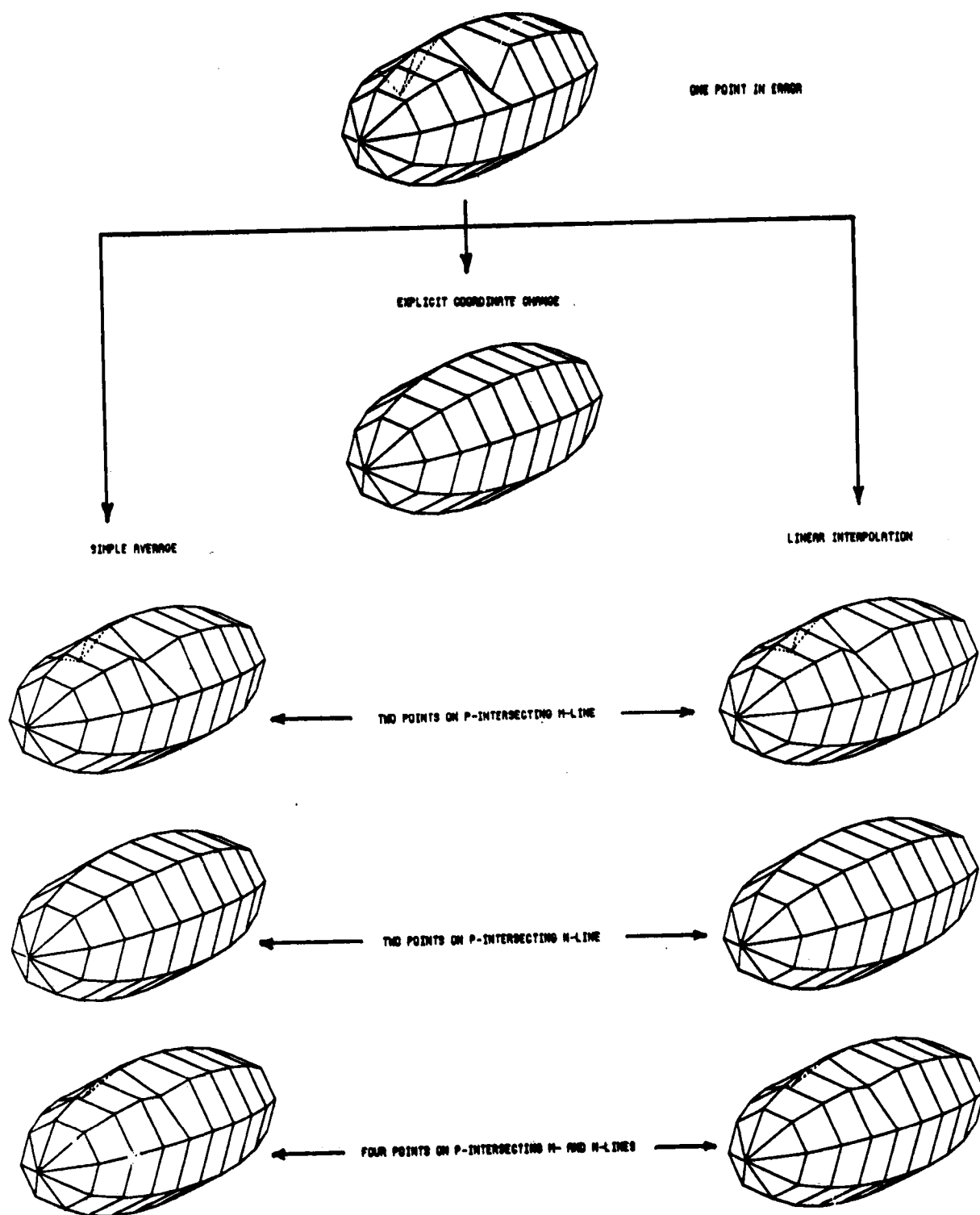
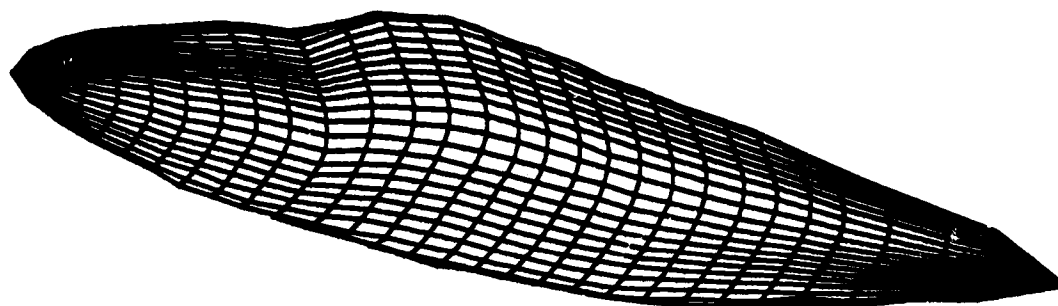


Figure 25: Examples of input-data modifications

ORIGINAL PAGE IS
OF POOR QUALITY.

ORIGINAL BODY



MODIFIED BODY

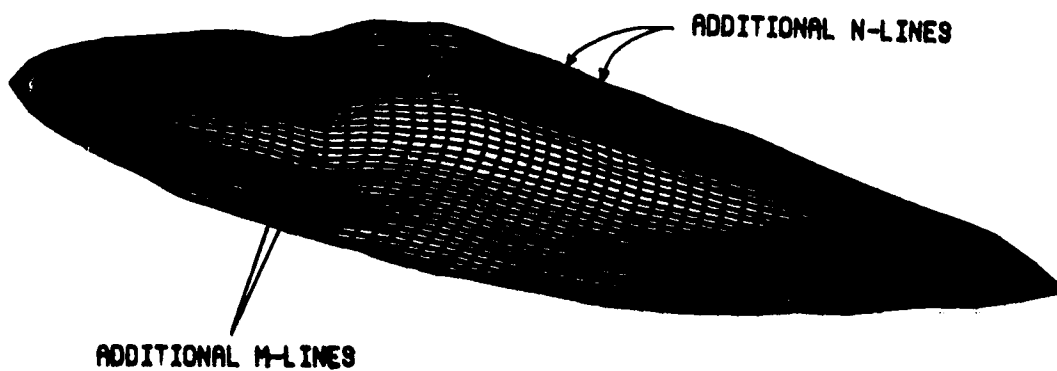


Figure 26. Example of equal-line augmentation scheme

body, care must be taken not to exceed the available computer storage capabilities.

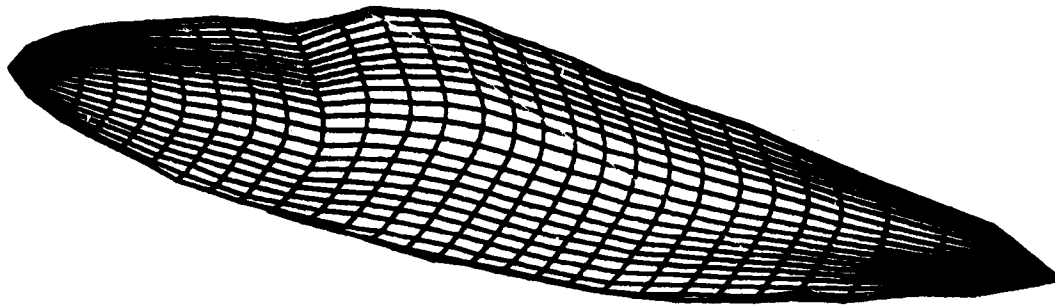
For the above reason and that only a grid network refinement in the neighborhoods of the inlet and exhaust sites is usually desired, a second option has been included. Although it uses the same M- and N-line distribution techniques and point calculations of the first option, the second option augments the total number of M-lines and/or N-lines only by generating additional lines between any two specific M-lines and/or N-lines chosen by the user. Without a drastic increase in the total number of body panels, this scheme, to be called the "user-specified line augmentation", has the ability to generate additional lines on specific regions of the body while increasing the number of panels in these regions with individual areas smaller than the original panels (Figure 27). If the user prefers, this option may be used to duplicate the results of the first option.

For a given body, aspects of both line augmentations may be used simultaneously if the preferences of one do not override those of the other. That is, sometimes the equal-line augmentation scheme may be desired for M-lines (or N-lines), while the user-supplied line-augmentation scheme may be desired for N-lines (or M-lines). The implementation of these preferences are easily accomplished through the present method's computational logic.

Containing the coordinates of the points describing the original body (with the modifications invoked by the first three geometry options) and/or the final modified-body, cards may be punched in two different forms. The first form is compatible as input to the NCSU BODY potential-flow program [4] and that of the present report, while the second form is compatible as input to the NCSU PLOT program [4] for plotting complete configurations.

ORIGINAL PAGE IS
OF POOR QUALITY

ORIGINAL BODY



MODIFIED BODY

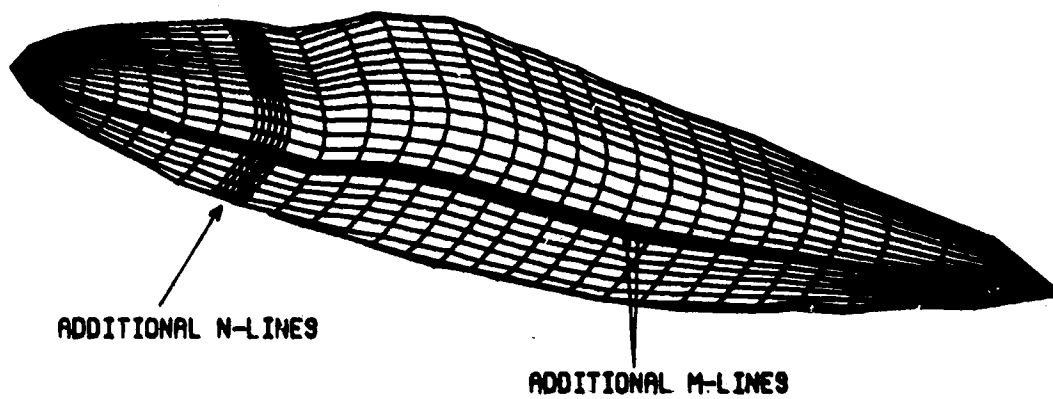


Figure 27. Example of user-specified line-augmentation scheme

Given a set of body data (either input or final), the grid-refinement program contains a plot option that allows for the generation of the necessary instructions for automatic plotting of the body and can be used to draw three-view and oblique orthographic projections, as well as perspective and stereoscopic projections. This option is a valuable tool for checking for inputted errors and for displaying the body modifications. Although examples of this plotting routine (originally written and programmed by Craidon, Reference 13) have been presented throughout this report, explicit examples are presented in Figures 28, 29, 30, and 31.

A geometry package has been developed by Halsey and Hess [Reference 14] which semi-automatically panels isolated components, such as wings, fuselages, etc., of complete aircraft configurations by using one of several element (quadrilateral) distribution algorithms. Among other options for repaneling components, the Halsey-Hess program is similar to that of the present work since both programs allow the input of sparse coordinate data, use independent cubic-spline curve fits for interpolations, and provide many schemes for the point distributions on M- and N-lines. However, significant differences do exist. The curve-fit method used by Halsey and Hess does not insure continuity of the second derivative and thus is not a true cubic-spline fit in the usual sense. They claim their method gave consistently superior results to those of a true cubic spline. Their point-distribution schemes are also significantly different but are logical and perform to a fair degree of accuracy. In addition, their geometry package contains a feature to calculate curves of intersection among components and consequently repanel the regions of the components at the intersections. This feature should be extremely useful for design of complete configurations and the study of interference effects among the

ORIGINAL PAGE NO.
OF POOR QUALITY

BEST CESSNA 182 WITH $M=21$ AND $N=29$

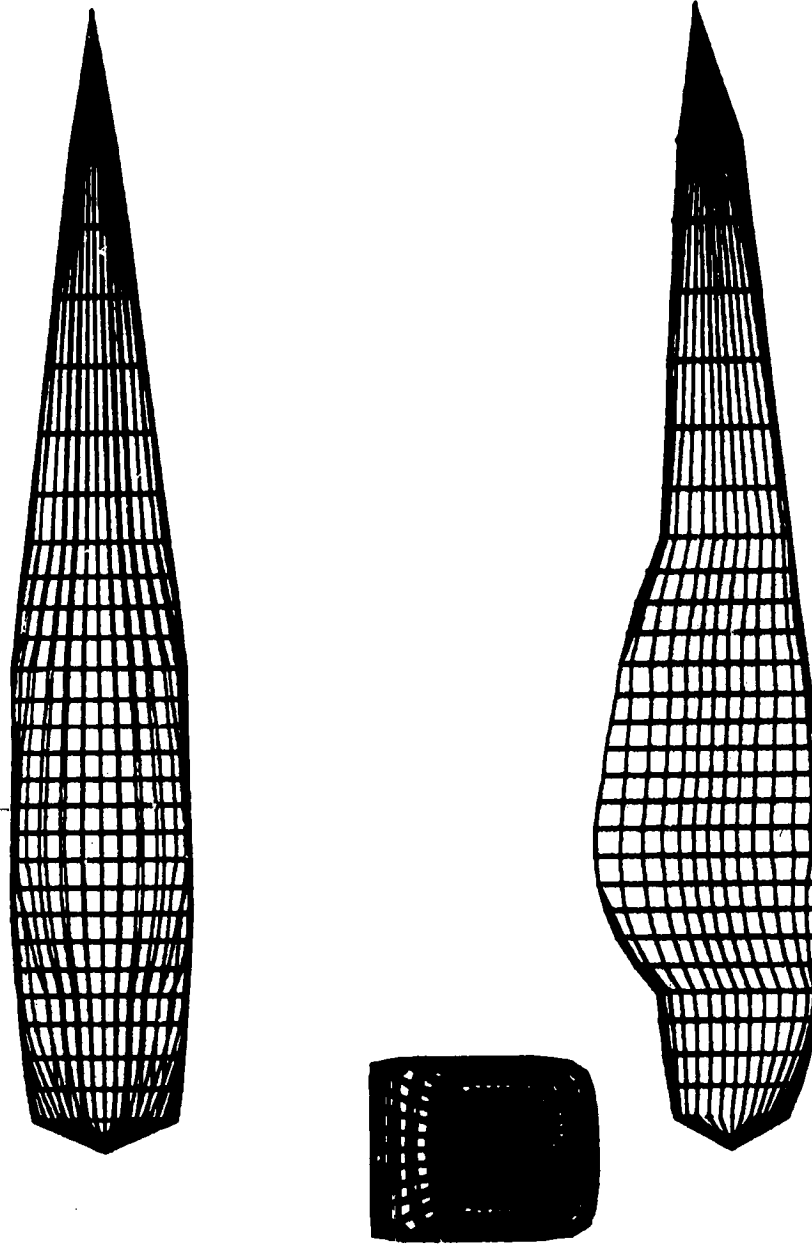
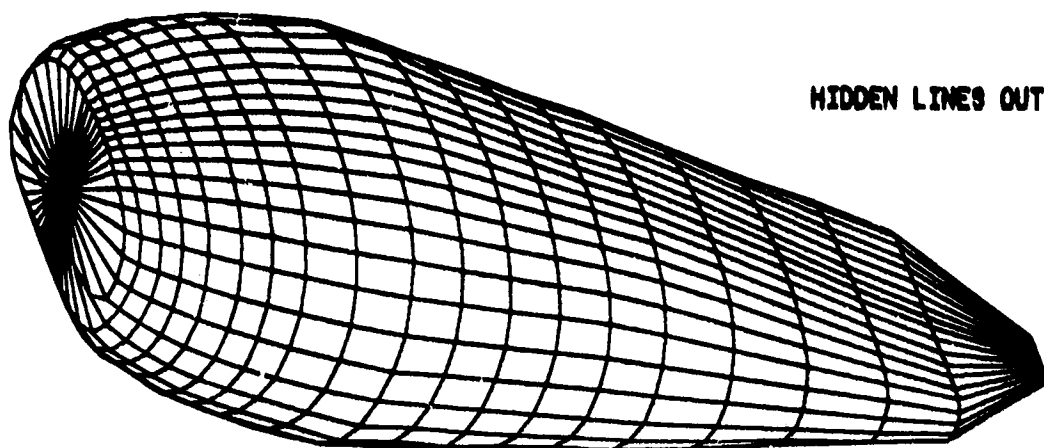


Figure 28. Example of a three-view orthographic projection

ORIGINAL PAGE IS
OF POOR QUALITY



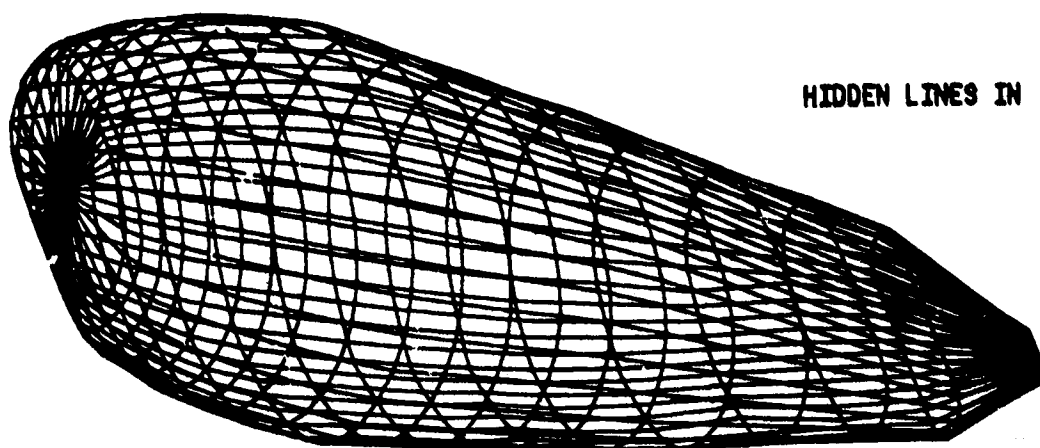
HIDDEN LINES OUT

NEW FAT NACELLE FOR LESS DRAG WITH N=21 AND M=21 YIELDING 400 PANELS --

X Z OUT 45. 10. 30.

6.0 ORT

0



HIDDEN LINES IN

NEW FAT NACELLE FOR LESS DRAG WITH N=21 AND M=21 YIELDING 400 PANELS --

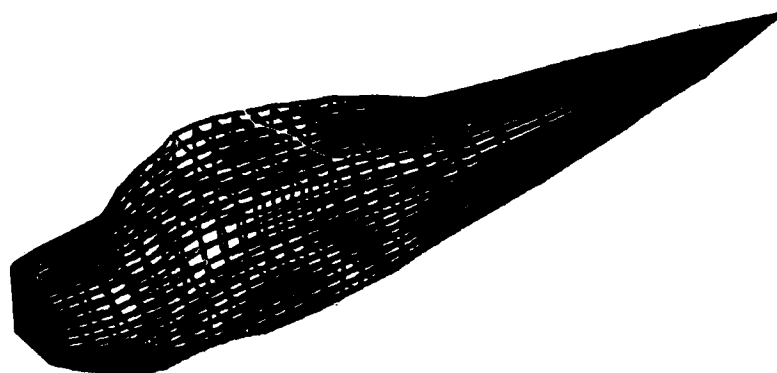
X Z 45. 10. 30.

6.0 ORT

1

Figure 29. Example of a oblique orthographic projection

ORIGINAL PAGE IS
OF POOR QUALITY



BEST CESSNA 182 WITH M-21 AND N-29 YIELDING 560 PANELS -- FUSELAGE ONLY

-20. -50. 50. 12. 0.0 0.0 14. 1.0 8.0 PER

1

Figure 30. Example of a perspective projection

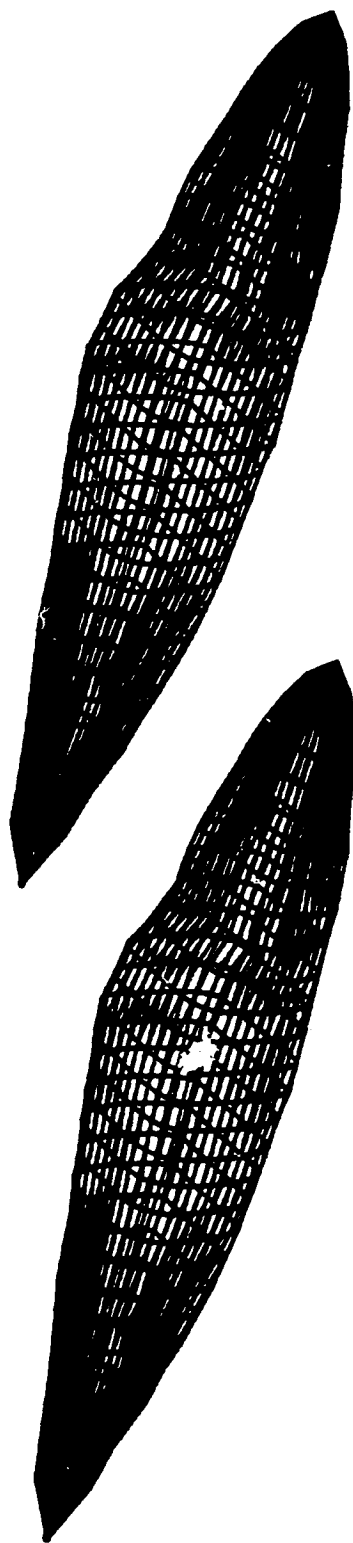


Figure 31. Example of stereoscopic projection

ORIGINAL PAGE IS
OF POOR QUALITY

components. Since only isolated components are analyzed by the present work, this option is not available.

For a geometry program to be efficient, it must be simple to use, have accurate but expeditious algorithms, and present results logically for immediate evaluation. While both programs are simple to use and have rapid and accurate algorithms, the present program contains its own built-in plotting routines that allow the user to visually inspect the point modifications and line augmentations. This feature eliminates the wasteful intermediate punching* of cards as input to separate plot programs, and therefore the overall time (program execution plus real time) to analyze body data is significantly reduced. The specialization of the program to the specific analysis capability described in previous sections also reduces the size of the geometry program and may provide more expeditious execution as well.

*The recording of data to magnetic tape or disk is common practice to avoid card punching.

COMPUTER IMPLEMENTATION OF METHODS

The aforementioned methods have been implemented into computer programs. In addition to the boundary layer, the nonuniform propeller slipstream, and the cooling interior-mass-flow simulations, a program performing the potential flow calculations has been named FLOWBODY, while a program performing the grid modifications has been named GRIDPLOT. The listings of both programs - along with their user's instructions, sample input, and sample output - are provided in Volume 2.

With logic easily adaptable to other computer facilities, both programs have been written in single-precision FORTRAN language. Single-precision arithmetic was chosen for two reasons. The first reason is that any smooth body represented by an arrangement of finite-sized plane quadrilaterals is inevitably crude, while the second is that the increase in computational times (and therefore costs) for additional precision is undesirable.

DISCUSSION OF RESULTS

An investigation has been made of means to reduce the drag of light aircraft fuselages and nacelles by recontouring the body and altering locations for the air intake and exhaust sites. Six bodies* were investigated with recontouring performed on only one because of time limitations. A general pattern has emerged that satisfies intuition as well as the physical phenomena. As an aid in the discussion of the forthcoming results of the present method, certain aspects of theoretical and physical flow behavior will be reviewed briefly.

The *total* or *over-all* drag on a body placed in a stream of fluid consists of *skin friction* (equal to the integral of all shearing stresses taken over the surface of the body) and of *form* or *pressure drag* (integral of components of the normal forces). Since it is important to determine the origin and magnitude of the skin friction and pressure drag, boundary-layer theory provides a means to explain these quantities in a rational fashion and also offers insight into what shape a body must take to minimize the total drag.

In the immediate neighborhood of a solid wall, boundary-layer flow (laminar or turbulent) may, under certain conditions, become reversed causing the external flow to separate from the wall. Accompanied by the formation of eddies and large energy losses in the wake of the body, this separation phenomenon changes the pressure distribution which differs markedly from that in a frictionless flow stream. The pressures on the lee side of the body are those of the

*Three-dimensional bodies with a X-Z plane of symmetry (plane parallel to the flow direction.)

wake and substantially below those on the windward side of the body which experience near-stagnation pressures. Integration of such a pressure distribution shows a large drag. Hence, a large pressure drag may be explained by the existence of a large pressure deviation.

Schlichting [15] gives an excellent description of boundary-layer separation by considering the flow about a blunt body, e.g., about a circular cylinder. In frictionless (perfect fluid) flow, the fluid particles are accelerated on the upstream half and decelerated on the downstream half. Hence, in accordance to Bernoulli's theorem, the pressure decreases along the upstream half, while it increases along the downstream half. So long as the boundary layer remains thin, the flow is frictionless and pressure is constantly being transformed into kinetic energy along the upstream half. On the downstream half, kinetic energy reverts back to pressure in proper amounts such that the pressure at the rearmost stagnation point exactly equals that of ambient conditions. Since the fluid particles in the boundary layer remain under the influence of the same pressure field as that prevailing externally, the pressure distributions are ideal and the body does not experience a pressure drag.

When viscosity (friction) is introduced, the particles expend so much of their kinetic energy during their travel along the upstream half of the cylinder that the remaining kinetic energy is sufficient for the particles to overcome the adverse pressure gradient on the cylinder's downstream half. Under this condition, the fluid motion within the boundary layer in the vicinity of the wall is eventually stopped and reversed by the external pressure field, resulting in separated flow. The wide separation of the streamlines behind the cylinder and their failure to merge smoothly indicate that the flow is not of the constant-energy type, and therefore Bernoulli's equation is unsuitable for the determination of pressures on the surface in the wake. Within the wake region

ORIGINAL PAGE IS
OF POOR QUALITY

behind the cylinder, a pressure-distribution curve clearly depicts suction or less-than-ambient pressure. Because of this pressure difference, a pressure drag occurs.

The shape of the body also controls the nature of the boundary-layer flow, i.e., whether the flow is laminar or turbulent. For minimum skin-friction drag, it is necessary or logical to maintain a laminar boundary over the greatest possible distance of the body. Although efforts have resulted in a reduction of skin-friction drag, attempts to maintain laminar flow along too great a surface distance can produce large increases in the over-all drag from high pressure drag. Since pressure drag can be many times greater than the skin-friction drag and flow separation should be delayed as long as possible, a turbulent boundary layer is desirable. Even though a turbulent layer increases the skin friction, a turbulent boundary layer is more stable than a laminar one and is capable of maintaining itself longer under an adverse pressure gradient because of its greater capacity to remove energy from the freestream. Consequently, the flow adheres to the surface for a greater distance and, in turn, delays separation. The increase in skin-friction drag is usually much less than the reduction in pressure drag.

Since the danger of boundary-layer separation always exists in regions of adverse pressure gradients with its likelihood of occurrence increasing for bodies with sharp or steep pressure curves (for instance, bodies with blunt ends), attempts should be made to seek a more streamlined body shape. The experimental pressure distributions for streamlined bodies differ so little from those predicted for frictionless flow that the pressure rise in the downstream direction is sufficiently gradual so that there is virtually no separation. Consequently, the pressure drag is small enough that the total drag consists mainly of skin-friction drag.

ORIGINAL PAGE IS
OF POOR QUALITY

When the boundary-layer equations are integrated, the velocity distribution can be obtained, and the location of the point of flow separation can be determined. This, in turn, allows the calculation of the viscous or skin-friction drag around the surface of the body by a simple process (in theory) of integrating the shearing stress imposed by the fluid onto the surface. Even in cases where there is no separation, the skin friction must be augmented by pressure drag because the boundary layer displaces the external potential* flow by a distance equal to the displacement thickness. The pressure distributions are therefore changed even in the absence of flow separation, and the resultant of these pressure forces in the flow direction is no longer zero. When applied to actual problems, this method and the present method** allow the calculation of both the skin-friction drag and the pressure drag.

Most fuselages and nacelles may be categorized as blunt or bluff bodies. For this reason, their drag is almost entirely due to pressure deviations (from ambient conditions) and, therefore, is generally greater than that of streamlined bodies of similar shape. In addition to rough surface textures, actual fuselages and nacelles experience interference effects from appendages and protuberances that, normally, adversely affect the drag. Since few appendages (wings, landing gear, etc.) can be removed, protuberances such as protruding engine exhaust pipes, projecting rivet heads, improperly-designed cowl flaps and canopies, etc. can be modified to provide the cleanest possible design without being impractical from the operational, maintenance, and financial points of view.

*Flow external to the boundary layer is considered to be inviscid and therefore potential.

**The reader should review the present report's section on boundary-layer simulation in an inviscid flow field.

ORIGINAL PAGE IS
OF POOR QUALITY

The obvious complexity of actual flow fields about real aircraft bodies makes it necessary to investigate the influence of *nonuniform** (in contrast to *uniform*) flows upon the over-all drag computations of the present method.

Following the recommendations of a previous section for a crude approximation of a propeller slipstream, systems of ring vortices were placed about bodies in a systematic fashion so that their diameters, strengths, and locations reflected the presence of the bodies and a specified power into the airstream. These vortex systems induced velocities from approximately five percent of the free-stream velocity onto the body near the nose to about ten percent near the tail for a specified power of 100.66 kilowatts.

The six bodies were tested with both uniform and nonuniform onset flow fields. The results are given in Figures 32, 33, 34, 35, 36, and 37 for the uniform flows, while those for the nonuniform flows are given in Figures 38, 39, 40, 41, 42, and 43. As shown by the figures, five of the six bodies with a nonuniform flow field experienced reductions in skin-friction drag along with substantial increases in the pressure or form drag, resulting in larger total drags. The other body also experienced an increase in pressure drag but was subdued by a substantial reduction in skin-friction drag to yield a lower total drag. A closer examination revealed that, possibly, the skin friction decreased because of the higher local Reynold's numbers at or near the body surfaces. Although the skin-friction drag was initially expected to increase because of the additional "scrubbing" of the flow upon the bodies, a 30% increase in velocity may be seen to reduce the friction drag by 7% or more. Thus, these friction-drag reductions were acceptable. The pressure drag increased because of the higher velocities over the surfaces that significantly modified the

*A nonuniform flow is defined as that onset flow with velocities differing from a constant value, whereas, an uniform flow is that onset flow with a constant velocity.

pressure distributions. The difference between the analytical method and physical phenomenon must also be noted. The analytical method automatically assumes flow separation near the rear of the body, while in actuality the flow may not separate because of the more energetic flow.

The drag calculations of the ATLIT aircraft fuselage (Figure 4) and nacelle (Figure 42) were compared with the experimental drag findings by Holmes [16] of a drag build-up for the complete aircraft. Holmes estimated the total aircraft drag coefficient to be 0.044. As a basis for comparison, the drag contributions [16] arising from the wing, the horizontal tail, and the vertical tail at zero angle of attack were accepted and used with the present method's prediction of those arising from the fuselage and nacelles to produce a total drag coefficient of 0.045. This prediction represents a significant improvement over previously-existing methods (including the 0.0358 value from earlier work of Smetana and Fox [17]) as well as portraying the present scheme as an useful tool for drag estimations.

A "fat" nacelle (Figure 37 or 38) was contrived for the purpose of investigating whether such a configuration might yield a lower drag for the ATLIT airplane. Initial calculations for the fat nacelle with an uniform onset flow field (Figure 37) showed a skin-friction drag coefficient of 0.00356 and pressure drag coefficient of 0.00317 to yield an over-all drag coefficient of 0.00673. Initial calculations for the ATLIT nacelle with an uniform onset flow field (Figure 36) showed a friction drag coefficient of 0.00308 and a pressure drag coefficient of 0.00414 to yield an over-all drag coefficient of 0.00722. Whereas, the friction drag for the fat nacelle was greater by 15.6%, a substantial decrease of 23.4% in the pressure drag was seen to cause a 6.8% reduction in the total drag. A nonuniform onset flow field was imposed onto the same two bodies to yield quite different results. For the fat nacelle (Figure 43), the skin-friction drag decreased by 9.2% to yield a skin-friction drag coefficient of 0.00323 and the pressure drag increased by 177% to yield a pressure drag

coefficient of 0.00879 for a total drag coefficient of 0.01203. For the ATLIT nacelle (Figure 42), the friction drag decreased by 7.5% to obtain a skin-friction drag coefficient of 0.00285 and the pressure drag increased by 84% to obtain a pressure drag coefficient of 0.00762 for a total drag coefficient of 0.01046. Obviously, the nonuniform flow had a significant effect since the total drag for the fat nacelle increased by 78.7% and that for the ATLIT nacelle increased by 44.9%. Although the smaller friction drags were acceptable, the extremely large increases in the pressure drags were not. Since these nacelles were wider and flatter than most bodies considered, the concept and utilization of the equivalent circular body (discussed in an earlier section) for the induced velocities by the propeller's slipstream onto the body surfaces were not suitable. For these nacelle cases and other possible cases of wide flat bodies, more accurate and realistic results would have been obtained with the use of an equivalent *ellipsoidal* body concept where the circular vortex rings are replaced with *elliptically-shaped* vortices. In addition to the unsuitability of the circular body scheme, the present tests were conducted with a propeller diameter less than the maximum cross-sectional dimension of the nacelles. Consequently, the propeller forced the air flow onto (rather than about and along) the surfaces, causing an appreciable variation in the velocity and pressure distributions and, in turn, resulting in a large increase in pressure drag. Specification of larger propeller diameters should lessen the increase to more realistic values.

Since all of the bodies were modeled by an orderly grouping of a large number of plane quadrilaterals (panels), it was therefore inevitable that such a modeling scheme produced only approximate representations to the actual bodies. For this reason, minor body recontouring was performed to study the severity of these crude models. The fuselage of a Cessna 182 airplane was

ORIGINAL PAGE IS
OF POOR QUALITY

chosen for this test. The body was recontoured by the GRIDPLOT program, while the drag computations were effected by the FLOWBODY program. Both programs are contained in Volume II of this work.

The study revealed that the total drag did not change appreciatively with typical calculations leading to drag reductions on the order of only one percent. In some cases, the total drag actually increased because of greater pressure drag attributed to larger adverse pressure gradients on the recontoured regions. In all cases the change in friction drag was insignificant. As an explicit example, the upper rearward cabin section of a Cessna 182 fuselage (Figure 38) was slightly recontoured or "smoothed" (Figure 39). Although difficult to see these modifications because of the scale and orientation of the drawings, calculations yielded a 0.42% total drag reduction with approximately 88% of this change arising from a decrease in the pressure drag. These results are encouraging since it is believed that further body modifications may reduce the drag even more.

A different situation occurred when more severe shape changes were imposed. The nose of the representation of the Cessna fuselage was severed or flattened to better approximate the actual fuselage (Figure 40). When compared with the results for the original fuselage (Figure 38), this action produced an increase of 11.3% in the pressure drag and a slight reduction of 0.65% in the skin-friction drag. Like the case of a flat plate nearly perpendicular to the flow direction, the increase in the pressure drag was entirely due to the disruption of the external flow field by the pressure of the blunt nose. In other words, the pressures on the blunt-nose panels of the fuselage approached the stagnation pressure, while the pressures on the "same" panels of the original fuselage were far less than the stagnation value. With the pressure distributions therefore changed, integration of the pressures over the entire surface produced a

net increase in the pressure drag. The skin-friction drag decreased primarily because of a decrease in the surface area.

Although modifications to body shape may be seen to affect the drag more or less, the main purpose of this work is to determine suitable locations for the intake and exhaust sites of the air mass flow for effective cooling and minimum adverse disruption of the external flow field. Intuitively, the location and size of these sites should be dependent on or influenced by the power setting and the magnitude of the effective orifice area of the engine.

Approximately 20 computer runs of the FLOWBODY program were performed on the blunt-nose Cessna fuselage. For the fuselage with the specification of the identical intake and exhaust sites and the same initial effective orifice area (Figures 44, 45, and 46), the total drag coefficient C_D was found to vary linearly with power (Figure 47). The validity or pausibility of these drag coefficients may be seen by comparing the present results with those from wind-tunnel tests of a light single-engine aircraft [Reference 18] and a light twin-engine aircraft [Reference 19]. The power settings were converted to thrust coefficients, and the drag coefficients of the present method were plotted along with those from wind-tunnel tests corresponding to zero lift. It can be observed from Figure 48 that the present method yielded drag coefficients approximately 60-70% below those from the wind-tunnel tests. Whereas, the wind-tunnel tests considered the full aircraft configurations, the present drag-coefficient extractions pertained only to those of the fuselage and, therefore, should be only 30-40% as large. The curve representing the results of the single-engine aircraft's wind-tunnel tests is shown to behave remarkably different from that of the twin-engine aircraft and the present method's findings. Such behavior may be attributable to higher local Reynold's numbers or to small

ORIGINAL PAGE IS
OF POOR QUALITY

or moderate flow separation. Further comparisons for similarly-shaped fuselages of References 9, 20, and 21 indicated that the extracted drag coefficients were indeed well within the range of typical values.

Upon the designation of specific panels on the body as air intake ports or exhaust ports, the FLOWBODY program assumes that the pressure coefficients on the "opened" panels are equal to those existing on the same impermeable panels of the closed body. In actuality, the pressure coefficients may be quite different if the respective panel areas are large in comparison to the total area of the body. Careful attention must be paid to satisfying this assumption if reasonable results are to be obtained. Since this analysis considers the interior of the body as essentially a "black box" containing an orifice (engine), a pressure drop normally occurs between the intake ports and the engine and, again, between the engine and the exhaust ports. Therefore, determination of two interior pressure coefficients is necessary to balance the mass flow properly. Since the models for the program consist of an arrangement of a large number of panels (each having its own pressure coefficient), the assumed pressure coefficients for the intake and exhaust ports are area-averages of those pressure coefficients existing on the individual sites.

As shown in Figure 49, an interesting and powerful result occurred when these pressure coefficients were plotted as functions of the effective orifice area, while the power and the intake and exhaust sites remained fixed. As the effective orifice area (EOA) was increased, the difference between the two interior pressure coefficients decreased. When EOA was increased to and beyond a value of 0.12 m^2 , the interior pressure coefficients had asymptotically approached a common value of 0.692. Therefore, a limiting value of EOA can be determined for each power setting and arrangement of intake and exhaust ports. Significant drag reductions were also observed as would be expected since the

ORIGINAL PAGE IS
OF POOR QUALITY

engine is now effectively out of the flow path. At these areas, cooling can be expected to be minimal. As depicted in Figure 50 (extracted from Figures 51, 52, 53, and 54), the total drag coefficient for the blunt-nose Cessna fuselage operating at the indicated test and freestream conditions decreased to 0.01240 (a 28.5% reduction in the drag of the same "closed" body) as the limiting EOA was reached. Since the mass flows entering and leaving the body are equal, sufficient air mass flow for effective engine cooling may be easily determined once the cooling requirements are known. It should also be noted that above the limiting EOA the drag no longer decreased but remained constant. Hence, a minimum-drag condition may be determined for each power setting and arrangement of the air intake and exhaust ports.

Intuition would suggest that the limiting EOA should be related to the intake and exhaust areas. Since the intake and exhaust pressure coefficients are determined by area-averages which in turn limit the range of values for the interior pressure coefficients (see Figure 49), their magnitudes and signs would indeed be functions of these areas. Upon this recognition, possible "optimum" sites for the air intake and exhaust may be chosen at the outset of the problem.

Cowl air intake and exhaust sites must be suitably designed and located so that they provide adequate engine cooling and carburetor induction and produce minimum pressure loss and favorable interactions with or minimum disruption to the external flows. Furthermore, they must provide good entrainment and extraction of the cooling air. The present method presumes that flows enter and exit the body normal to its surface and, consequently, must be of relatively low velocities to avoid severe disturbances to the external flow. It is advantageous to obtain prudent insight for judiciously selecting the proper sites.

ORIGINAL PAGE IS
OF POOR QUALITY

A fundamental knowledge of fluid dynamics is effectually sufficient for this task.

Several representative test cases were performed on the blunt-nose Cessna fuselage to yield the following general results:

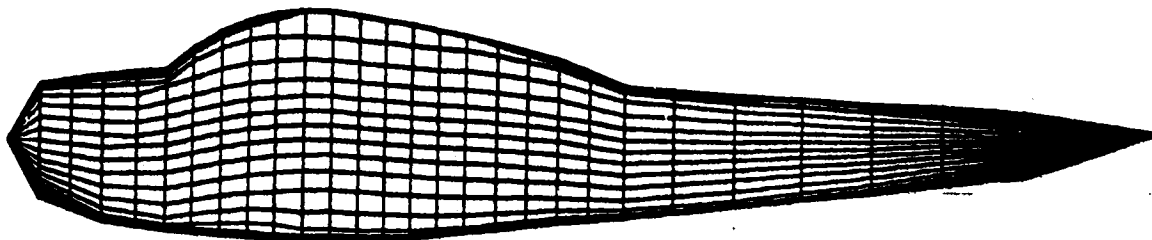
- (a) Exhausting cooling air into concave regions of the fuselage at relatively low velocities results in significant decreases in over-all pressure drag, probably because it effectively increases body streamlining. Two typical regions where this is particularly effective are immediately upstream of the canopy and immediately downstream of the canopy.
- (b) The volumetric flow rate of cooling air passing through the fuselage should not exceed the amount required for cooling because significant drag increments are associated with excesses. Since the flow rate depends upon the flight conditions, provisions should be available for controlling this flow rate. This suggests the use of flush, sliding cowl flaps which efficiently regulates the flow by varying the area of the exhaust port.
- (c) For good entrapment and extraction of the cooling air and minimum pressure loss, intakes should be located over regions with pressures near that of stagnation and exhausts should be located in low-pressure concave regions such that the exhaust flow produces a minimum disruption to or a favorable interaction with the external flow.
- (d) Sharp edges, bluff frontal surfaces, and short afterbodies should be avoided. These are found to produce significant regions of flow separation and therefore increased drags.

ORIGINAL PAGE IS
OF POOR QUALITY

The results of the 20 test cases conducted on the blunt-nose Cessna fuselage were insufficient to establish the "best" minimum-drag condition(s) for a particular power setting. The majority of the cases were performed to observe the behavior of the results, and thus only a small number remained for further verifications and comparisons. Although limited in scope, three additional fuselage shapes were investigated to yield results consistent with those of the blunt-nose Cessna. Without much fear of contradiction, the repeated occurrence of consistent patterns was perceived as generalizations applicable for a wide range of light aircraft.

ORIGINAL PAGE IS
OF POOR QUALITY

Body Description: Cessna 182 Fuselage Model
Flow Description: Uniform



Test Conditions:

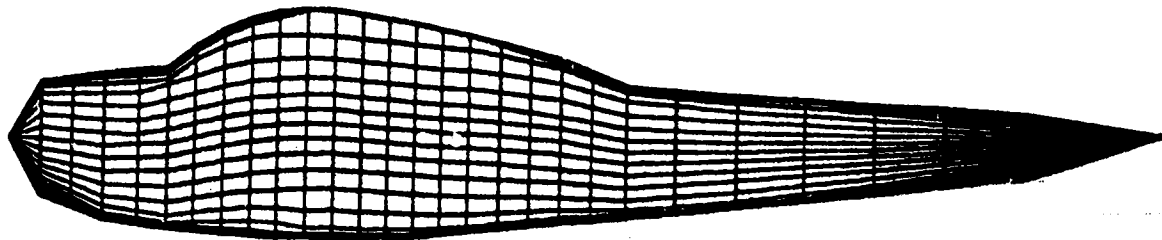
Freestream velocity (VIN _F), m/sec	48.768
Freestream density (ROE), kg/m ³	1.2252
Kinematic viscosity (VO), m ² /sec	1.486×10^{-5}
Reference area (REF _A), m ²	16.165
Developed engine power (DEP), kW	0.0
Reynold's number	24,420,000

Analysis Results:

Pressure C _L (w/o wake-body)	0.00446
Pressure C _D (w/o wake-body)	0.00488
Friction C _D	0.00780
Pressure C _L (with wake-body)	0.00444
Pressure C _D (with wake-body)	0.00491
Total Body C _L = 0.00444	
Total Body C _D = 0.01270	

Figure 32: Results of Cessna 182 fuselage model with uniform flow (power-off).

Body Description: Recontoured Cessna 182 Fuselage Model
Flow Description: Uniform



Test Conditions:

Freestream velocity (VINP), m/sec	48.768
Freestream density (ROE), kg/m ³	1.2252
Kinematic viscosity (VO), m ² /sec	1.486×10^{-5}
Reference area (REFA), m ²	16.165
Developed engine power (DEP), kW	0.0
Reynold's number	24,420,000

Analysis Results:

Pressure C_L (w/o wake-body)	0.00425
Pressure C_D (w/o wake-body)	0.00507
Friction C_D	0.00783
Pressure C_L (with wake-body)	0.00423
Pressure C_D (with wake-body)	0.00509

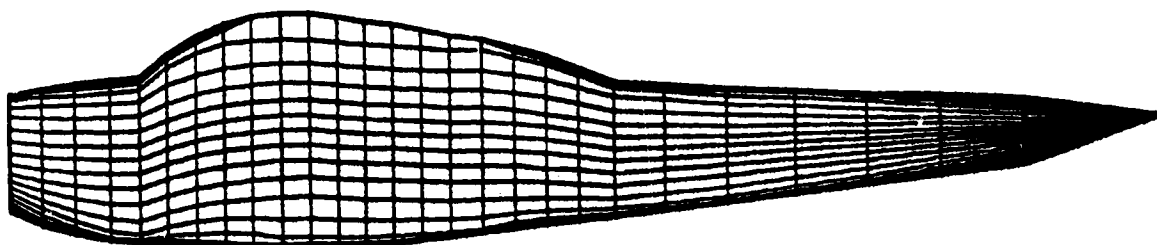
Total Body C_L = 0.00423

Total Body C_D = 0.01291

Figure 33: Results of recontoured Cessna 182 fuselage model with uniform flow (power-off).

ORIGINAL PAGE IS
OF POOR QUALITY

Body Description: Blunt-nose Cessna 182 Fuselage Model
Flow Description: Uniform



Test Conditions:

Freestream velocity (VIN _F), m/sec	48.768
Freestream density (ROE), kg/m ³	1.2252
Kinematic viscosity (VO), m ² /sec	1.486×10^{-5}
Reference area (REFA), m ²	16.165
Developed engine power (DEP), kW	0.0
Reynold's number	23,750,000

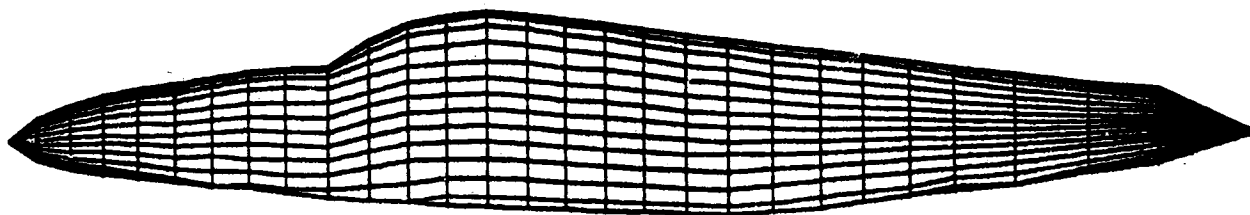
Analysis Results:

Pressure C _L (w/o wake-body)	0.00653
Pressure C _D (w/o wake-body)	0.00539
Friction C _D	0.00772
Pressure C _L (with wake-body)	0.00651
Pressure C _D (with wake-body)	0.00542
Total Body C _L	= 0.00651
Total Body C _D	= 0.01314

Figure 34: Results of blunt-nose Cessna 182 fuselage model with uniform flow (power-off).

ORIGINAL PAGE IS
OF POOR QUALITY

Body Description: ATLIT Fuselage Model
Flow Description: Uniform



Test Conditions:

Freestream velocity (VIN _F), m/sec	48.768
Freestream density (ROE), kg/m ³	1.2252
Kinematic viscosity (VO), m ² /sec	1.486×10^{-5}
Reference area (REFA), m ²	14.40
Developed engine power (DEP), kW	0.0
Reynold's number	28,250,000

Analysis Results:

Pressure C _L (w/o wake-body)	0.00329
Pressure C _D (w/o wake-body)	0.00222
Friction C _D	0.01057
Pressure C _L (with wake-body)	0.00300
Pressure C _D (with wake-body)	0.00242

Total Body C_L = 0.00300

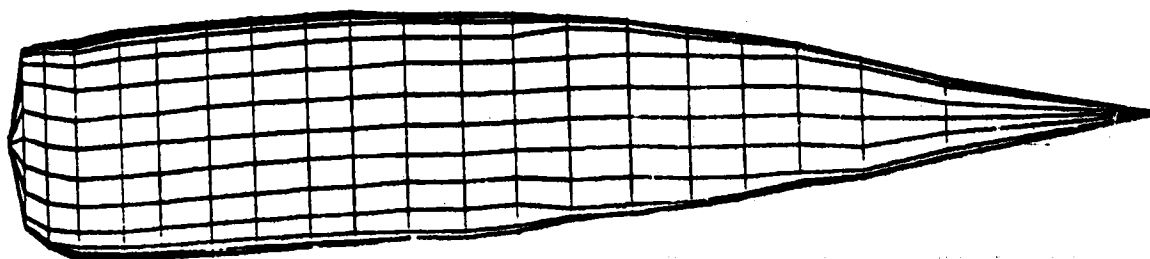
Total Body C_D = 0.01299

Figure 35: Results of ATLIT fuselage model with uniform flow (power-off).

ORIGINAL PAGE IS
OF POOR QUALITY

ORIGINAL PAGE IS
OF POOR QUALITY

Body Description: ATLIT Nacelle Model
Flow Description: Uniform



Test Conditions:

Freestream velocity (VIN _F), m/sec	48.768
Freestream density (ROE), kg/m ³	1.2252
Kinematic viscosity (VO), m ² /sec	1.486×10^{-5}
Reference area (REFA), m ²	14.40
Developed engine power (DEP), kW	0.0
Reynold's number	9,667,000

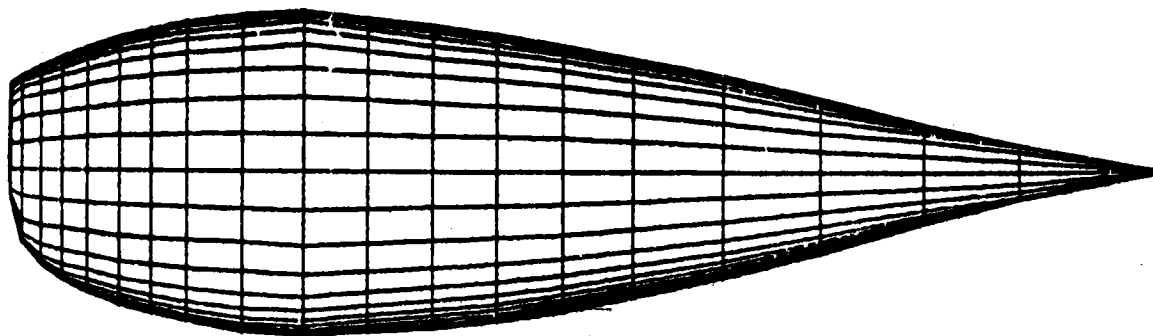
Analysis Results:

Pressure C _L (w/o wake-body)	0.00229
Pressure C _D (w/o wake-body)	0.00391
Friction C _D	0.00308
Pressure C _L (with wake-body)	0.00235
Pressure C _D (with wake-body)	0.00414
Total Body C _L = 0.00235	
Total Body C _D = 0.00722	

Figure 36: Results of ATLIT nacelle model with uniform flow (power-off).

Body Description: Fat Nacelle Model
Flow Description: Uniform

ORIGINAL PAGE IS
OF POOR QUALITY



Test Conditions:

Freestream velocity (VINP), m/sec	48.768
Freestream density (ROE), kg/m ³	1.2252
Kinematic viscosity (VO), m ² /sec	1.486×10^{-5}
Reference area (REFA), m ²	14.40
Developed engine power (DEP), kW	0.0
Reynold's number	9,628,000

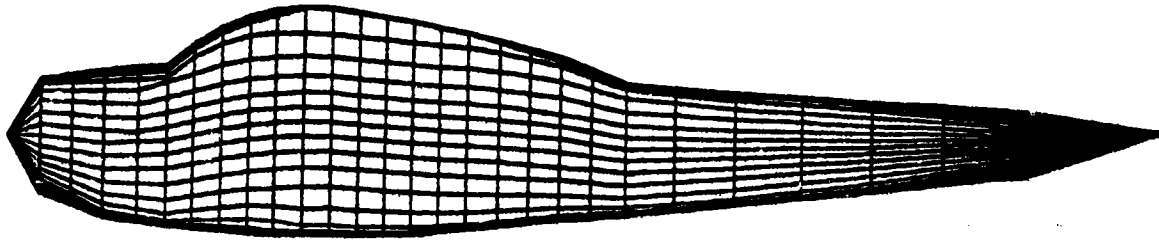
Analysis Results:

Pressure C_L (w/o wake-body)	0.00228
Pressure C_D (w/o wake-body)	0.00331
Friction C_D	0.00356
Pressure C_L (with wake-body)	0.00240
Pressure C_D (with wake-body)	0.00317
Total Body $C_L = 0.00240$	
Total Body $C_D = 0.00673$	

Figure 37: Results of a fat nacelle model with uniform flow (power-off).

ORIGINAL PAGE IS
OF POOR QUALITY

Body Description: Cessna 182 Fuselage Model
Flow Description: Nonuniform



Test Conditions:

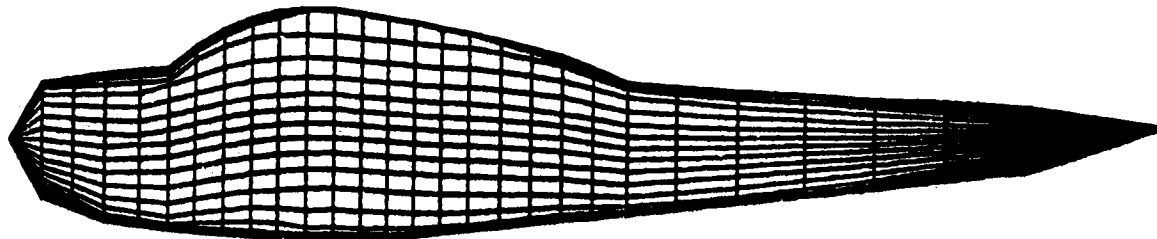
Freestream velocity (VIN _F), m/sec	48.768
Freestream density (ROE), kg/m ³	1.2252
Kinematic viscosity (VO), m ² /sec	1.486×10^{-5}
Reference area (REFA), m ²	16.165
Developed engine power (DEP), kW	100.66
Reynold's number	24,420,000

Analysis Results:

Pressure C _L (w/o wake-body)	0.00358
Pressure C _D (w/o wake-body)	0.00930
Friction C _D	0.00699
Pressure C _L (with wake-body)	0.00354
Pressure C _D (with wake-body)	0.00934
Total Body C _L = 0.00354	
Total Body C _D = 0.01633	

Figure 38: Results of Cessna 182 fuselage model with nonuniform flow (power-on).

Body Description: Recontoured Cessna 182 Fuselage Model
Flow Description: Nonuniform



Test Conditions:

Freestream velocity (VIN _F), m/sec	48.768
Freestream density (ROE), kg/m ³	1.2252
Kinematic viscosity (VO), m ² /sec	1.486×10^{-5}
Reference area (REFA), m ²	16.165
Developed engine power (DEP), kW	100.66
Reynold's number	24,420,000

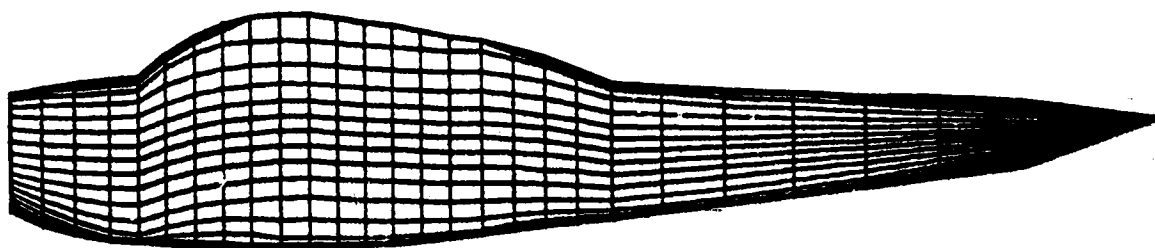
Analysis Results:

Pressure C _L (w/o wake-body)	0.00330
Pressure C _D (w/o wake-body)	0.00934
Friction C _D	0.00699
Pressure C _L (with wake-body)	0.00326
Pressure C _D (with wake-body)	0.00926
Total Body C _L = 0.00326	
Total Body C _D = 0.01623	

Figure 39: Results of recontoured Cessna 182 fuselage model with nonuniform flow (power-on).

ORIGINAL PAGE IS
OF POOR QUALITY

Body Description: Blunt-nose Cessna 182 Fuselage Model
Flow Description: Nonuniform



Test Conditions:

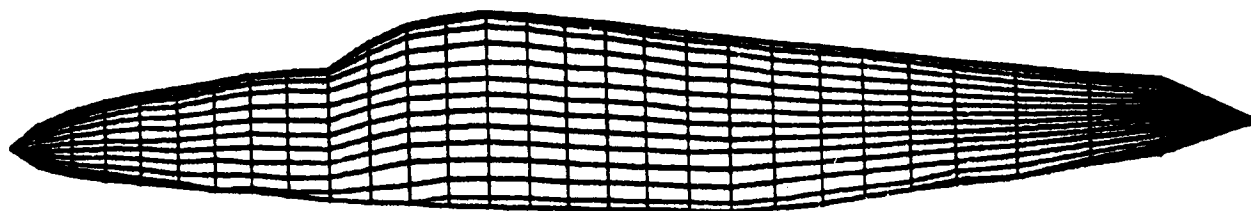
Freestream velocity (VIN _F), m/sec	48.768
Freestream density (ROE), kg/m ³	1.2252
Kinematic viscosity (VO), m ² /sec	1.486 × 10 ⁻⁵
Reference area (REF _A), m ²	16.165
Developed engine power (DEP), kW	100.66
Reynold's number	23,750,000

Analysis Results:

Pressure C _L (w/o wake-body)	0.00514
Pressure C _D (w/o wake-body)	0.01035
Friction C _D	0.00694
Pressure C _L (with wake-body)	0.00510
Pressure C _D (with wake-body)	0.01040
Total Body C _L = 0.00510	
Total Body C _D = 0.01734	

Figure 40: Results of blunt-nose Cessna 182 fuselage model with nonuniform flow (power-on).

Body Description: ATLIT Fuselage Model
Flow Description: Nonuniform



Test Conditions:

Freestream velocity (VIN _F), m/sec	48.768
Freestream density (ROE), kg/m ³	1.2252
Kinematic viscosity (VO), m ² /sec	1.486×10^{-5}
Reference area (REFA), m ²	14.40
Developed engine power (DEP), kW	100.66
Reynold's number	28,250,000

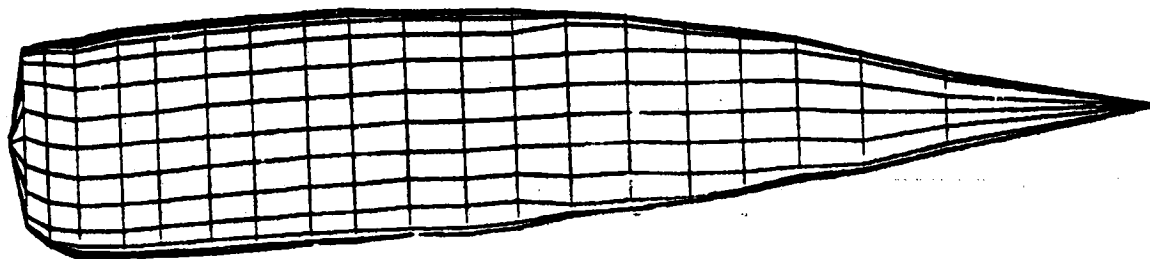
Analysis Results:

Pressure C _L (w/o wake-body)	0.00246
Pressure C _D (w/o wake-body)	0.00251
Friction C _D	0.00927
Pressure C _L (with wake-body)	0.00223
Pressure C _D (with wake-body)	0.00271
Total Body C _L = 0.00223	
Total Body C _D = 0.01198	

Figure 41: Results of ATLIT fusealge model with nonuniform flow
(power-on).

ORIGINAL PAGE 13
OF POOR QUALITY

Body Description: ATLIT Nacelle Model
Flow Description: Nonuniform



Test Conditions:

Freestream velocity (VIN _F), m/sec	48.768
Freestream density (ROE), kg/m ³	1.2252
Kinematic viscosity (VO), m ² /sec	1.486×10^{-5}
Reference area (REFA), m ²	14.40
Developed engine power (DEP), kW	100.66
Reynold's number	9,667,000

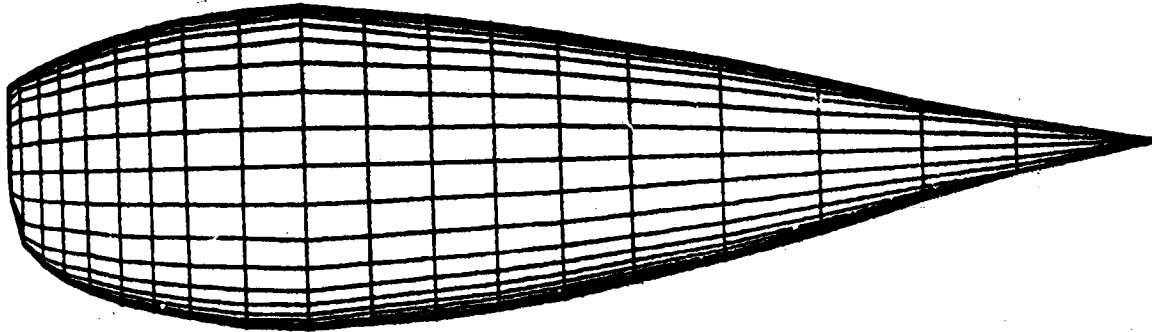
Analysis Results:

Pressure C _L (w/o wake-body)	0.00182
Pressure C _D (w/o wake-body)	0.00745
Friction C _D	0.00285
Pressure C _L (with wake-body)	0.00189
Pressure C _D (with wake-body)	0.00762
Total Body C _L = 0.00189	
Total Body C _D = 0.01046	

Figure 42: Results of ATLIT nacelle model with nonuniform flow (power-on).

ORIGINAL PAGE IS
OF POOR QUALITY

Body Description: Fat Nacelle Model
Flow Description: Nonuniform



Test Conditions:

Freestream velocity (VIN _F), m/sec	48.768
Freestream density (ROE), kg/m ³	1.2252
Kinematic viscosity (VO), m ² /sec	1.486×10^{-5}
Reference area (REFA), m ²	14.40
Developed engine power (DEP), kW	100.66
Reynold's number	9,628,000

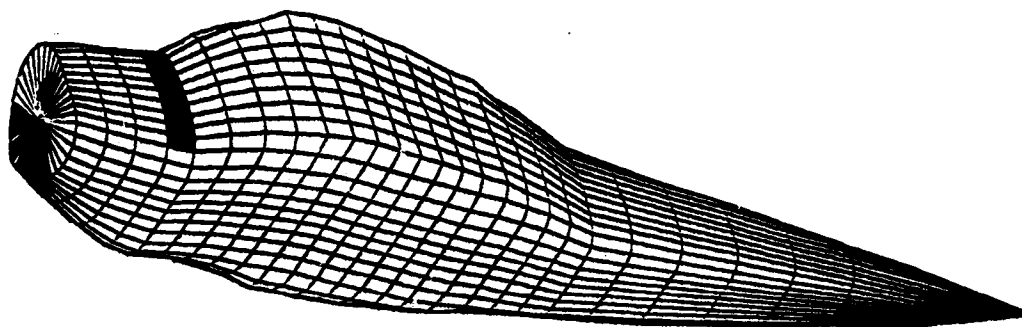
Analysis Results:

Pressure C _L (w/o wake-body)	0.00187
Pressure C _D (w/o wake-body)	0.00894
Friction C _D	0.00323
Pressure C _L (with wake-body)	0.00199
Pressure C _D (with wake-body)	0.00879
Total Body C _L = 0.00199	
Total Body C _D = 0.01203	

Figure 43: Results of fat nacelle model with nonuniform flow
(power-on).

ORIGINAL PAGE IS
OF POOR QUALITY

Body Description: Blunt-nose Cessna 182 Fuselage Model
Flow Description: Nonuniform



(Shaded areas denote ports for air intake and exhaust)

Test Conditions:

Freestream velocity (VIN _F), m/sec	48.768
Freestream density (ROE), kg/m ³	1.2252
Freestream temperature (TIN _F), °K	288.86
Kinematic viscosity (VO), m ² /sec	1.486 × 10 ⁻⁵
Constant-pressure specific heat of air (CPHA), kJ/kg°K ...	0.3095
Reference area (REFA), m ²	16.165
Heat of combustion of fuel (HVF), kJ/kg	41787.54
Specific fuel consumption (SFC), kg/kJ	1.5561 × 10 ⁻⁴
Developed engine power (DEP), kW	74.563
Initial effective orifice area (EOA), m ²	0.04645
Reynold's number	23,750,000

Specification of non-zero normal velocities

Input Code:	MS1	MS2	NS1	NS2	Panel No.	Type
	1	2	1	2	1	Intake
	3	4	1	2	5	Intake
	4	5	1	2	7	Intake
	5	6	1	2	9	Intake
	6	7	1	2	11	Intake
	7	8	1	2	13	Intake
	8	9	1	2	15	Intake
	16	17	5	6	111	Exhaust
	17	18	5	6	113	Exhaust
	18	19	5	6	115	Exhaust
	19	20	5	6	117	Exhaust
	20	21	5	6	119	Exhaust

Figure 44: Results of blunt-nose Cessna 182 fuselage model (nonuniform flow, 74.563 kW power, intake and exhaust ports).

ORIGINAL PAGE IS
OF POOR QUALITY

Analysis Results:

(Average C_p) _{inlet}	= 0.72902	(Average C_p) _{exhaust}	= 0.02949
Inlet area, m ²	= 0.07158	Exhaust area, m ²	= 0.08294
T_∞/T_1	= 0.681	Final EOA, m ²	= 0.03833

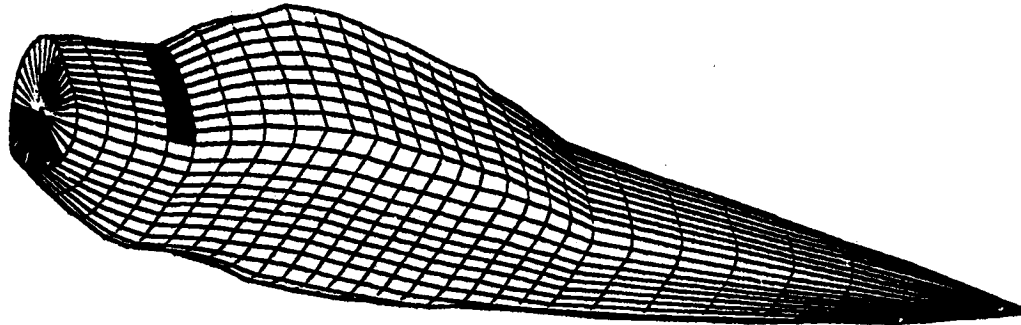
C_{p_x} = 0.64605
 $C_{p_{xx}}$ = 0.35667

Pressure C_L (w/o wake-body)	0.00276
Pressure C_D (w/o wake-body)	0.00656
Friction C_D	0.00666
Pressure C_L (with wake-body)	0.00273
Pressure C_D (with wake-body)	0.00660

Total Body C_L = 0.00273
 Total Body C_D = 0.01326

Figure 44: Concluded

Body Description: Blunt-nose Cessna 182 Fuselage Model
Flow Description: Nonuniform



(Shaded areas denote ports for air intake and exhaust)

Test Conditions:

Freestream velocity (VIN _F), m/sec	48.768
Freestream density (ROE), kg/m ³	1.2252
Freestream temperature (TIN _F), °K	288.86
Kinematic viscosity (VO), m ² /sec	1.486×10^{-5}
Constant-pressure specific heat of air (CPHA), kJ/kg°K ...	0.3095
Reference area (REFA), m ²	16.165
Heat of combustion of fuel (HVF), kJ/kg	41787.54
Specific fuel consumption (SFC), kg/kJ	1.5561×10^{-4}
Developed engine power (DEP), kW	100.66
Initial effective orifice area (EOA), m ²	0.04645
Reynold's number	23,750,000

Specification of non-zero normal velocities

Input Code:	MS1	MS2	NS1	NS2	Panel No.	Type
	1	2	1	2	1	Intake
	3	4	1	2	5	Intake
	4	5	1	2	7	Intake
	5	6	1	2	9	Intake
	6	7	1	2	11	Intake
	7	8	1	2	13	Intake
	8	9	1	2	15	Intake
	16	17	5	6	111	Exhaust
	17	18	5	6	113	Exhaust
	18	19	5	6	115	Exhaust
	19	20	5	6	117	Exhaust
	20	21	5	6	119	Exhaust

Figure 45: Results of blunt-nose Cessna fuselage model (nonuniform flow, 100,66 kW power, intake and exhaust ports).

ORIGINAL PAGE IS
OF POOR QUALITY

Analysis Results:

(Average C_p) _{inlet}	= 0.70333	(Average C_p) _{exhaust}	= 0.15529
Inlet area, m ²	= 0.07158	Exhaust area, m ²	= 0.08294
T_∞/T_1	= 0.640	Final EOA, m ²	= 0.03715

$$C_{p_x} = 0.60290$$

$$C_{p_{xx}} = 0.23009$$

Pressure C_L (w/o wake-body)	0.00195
Pressure C_D (w/o wake-body)	0.01035
Friction C_D	0.00613
Pressure C_L (with wake-body)	0.00190
Pressure C_D (with wake-body)	0.01040

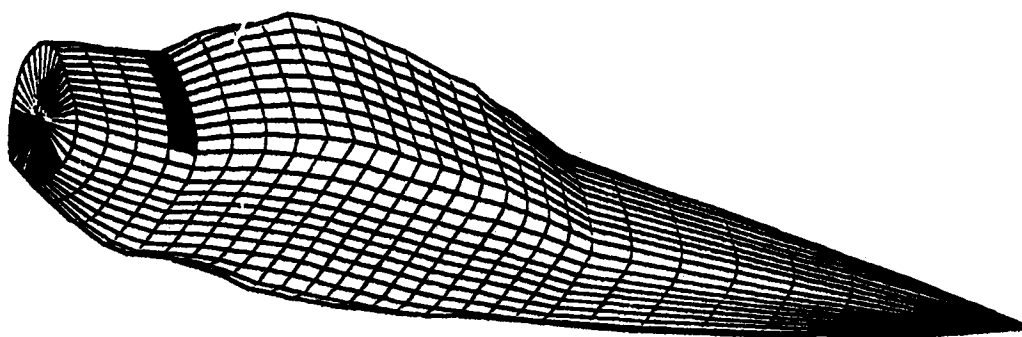
$$\text{Total Body } C_L = 0.00190$$

$$\text{Total Body } C_D = 0.01654$$

Figure 45: Concluded.

ORIGINAL PAGE IS
OF POOR QUALITY

Body Description: Blunt-nose Cessna 182 Fuselage Model
Flow Description: Nonuniform



(Shaded areas denote ports for air intake and exhaust)

Test Conditions:

Freestream velocity (VIN _F), m/sec	48.768
Freestream density (RO _E), kg/m ³	1.2252
Freestream temperature (TIN _F), °K	288.86
Kinematic viscosity (VO), m ² /sec	1.486×10^{-5}
Constant-pressure specific heat of air (CPH _A), kJ/kg°K ...	0.3095
Reference area (REFA), m ²	16.165
Heat of combustion of fuel (HVF), kJ/kg	41787.54
Specific fuel consumption (SFC), kg/kJ	1.5561×10^{-4}
Developed engine power (DEP), kW	223.69
Initial effective orifice area (EOA), m ²	0.04645
Reynold's number	23,750,000

Specification of non-zero normal velocities

Input Code:	MS1	MS2	NS1	NS2	Panel No.	Type
	1	2	1	2	1	Intake
	3	4	1	2	5	Intake
	4	5	1	2	7	Intake
	5	6	1	2	9	Intake
	6	7	1	2	11	Intake
	7	8	1	2	13	Intake
	8	9	1	2	15	Intake
	16	17	5	6	111	Exhaust
	17	18	5	6	113	Exhaust
	18	19	5	6	115	Exhaust
	19	20	5	6	117	Exhaust
	20	21	5	6	119	Exhaust

Figure 46: Results of blunt-nose Cessna 182 fuselage model (nonuniform flow, 223.69 kW power, intake and exhaust ports).

ORIGINAL PAGE IS
OF POOR QUALITY

Analysis Results:

(Average C_p) _{inlet}	= 0.60655	(Average C_p) _{exhaust}	= -0.41775
Inlet area, m ²	= 0.07158	Exhaust area, m ²	= 0.08294
T_∞/T_1	= 0.522	Final EOA, m ²	= 0.03356

C_{p_x} = 0.44380
 $C_{p_{xx}}$ = -0.29653

Pressure C_L (w/o wake-body)	0.00051
Pressure C_D (w/o wake-body)	0.02648
Friction C_D	0.00768
Pressure C_L (with wake-body)	0.00037
Pressure C_D (with wake-body)	0.02658

Total Body C_L = 0.00037
 Total Body C_D = 0.03427

Figure 46: Concluded.

ORIGINAL PAGE IS
OF POOR QUALITY.

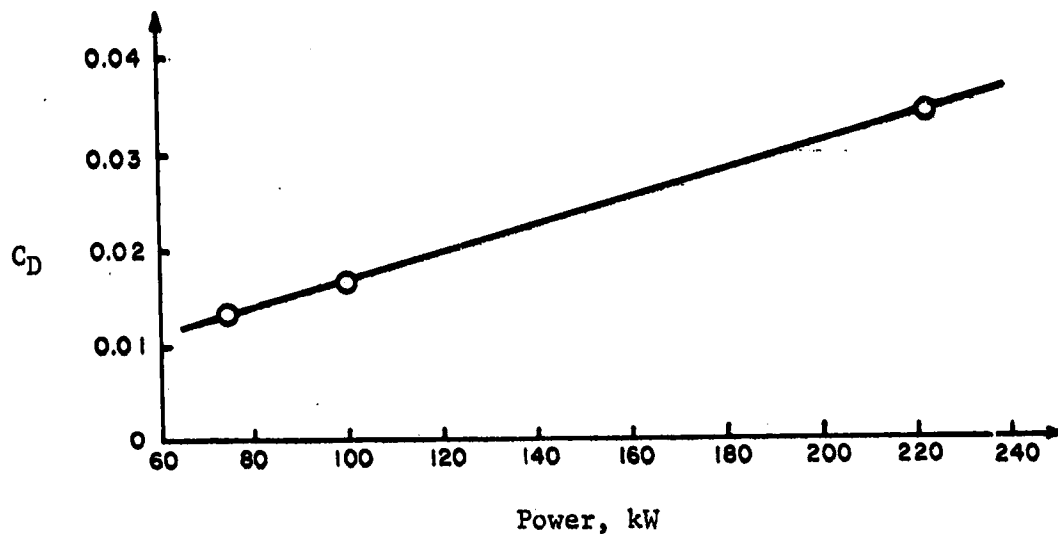


Figure 47: Variation of total drag coefficient C_D with power for blunt-nose Cessna fuselage model with fixed intake and exhaust sites.

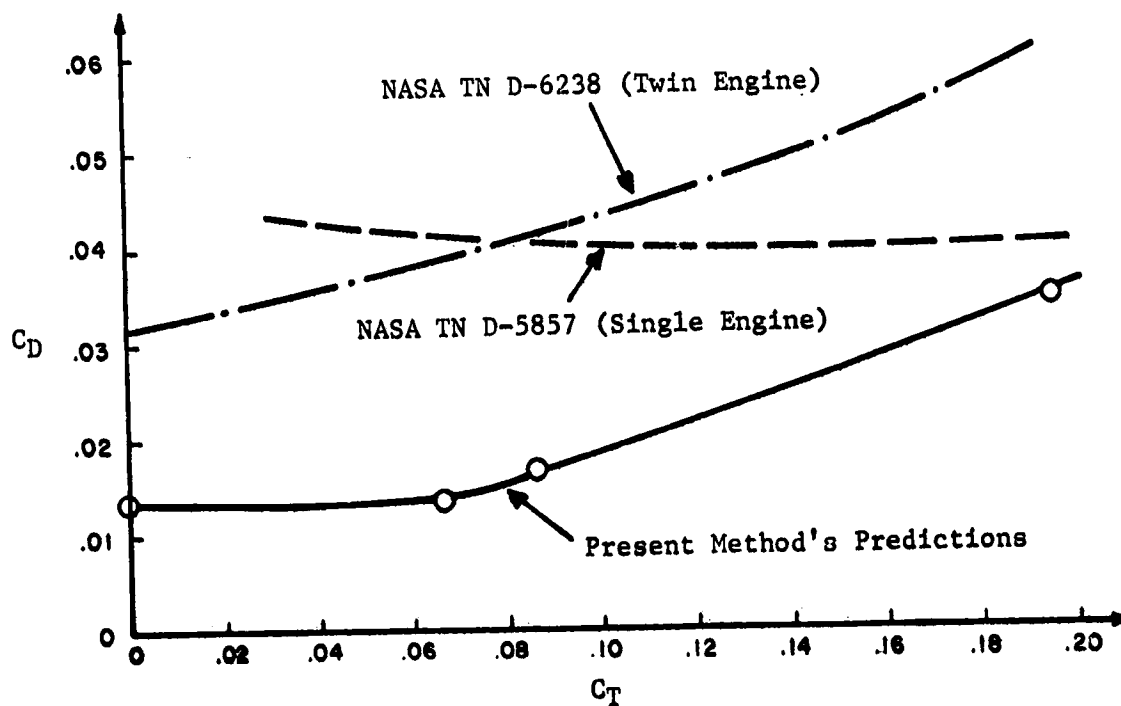


Figure 48: Comparison of drag coefficients C_D between prediction and wind-tunnel tests.

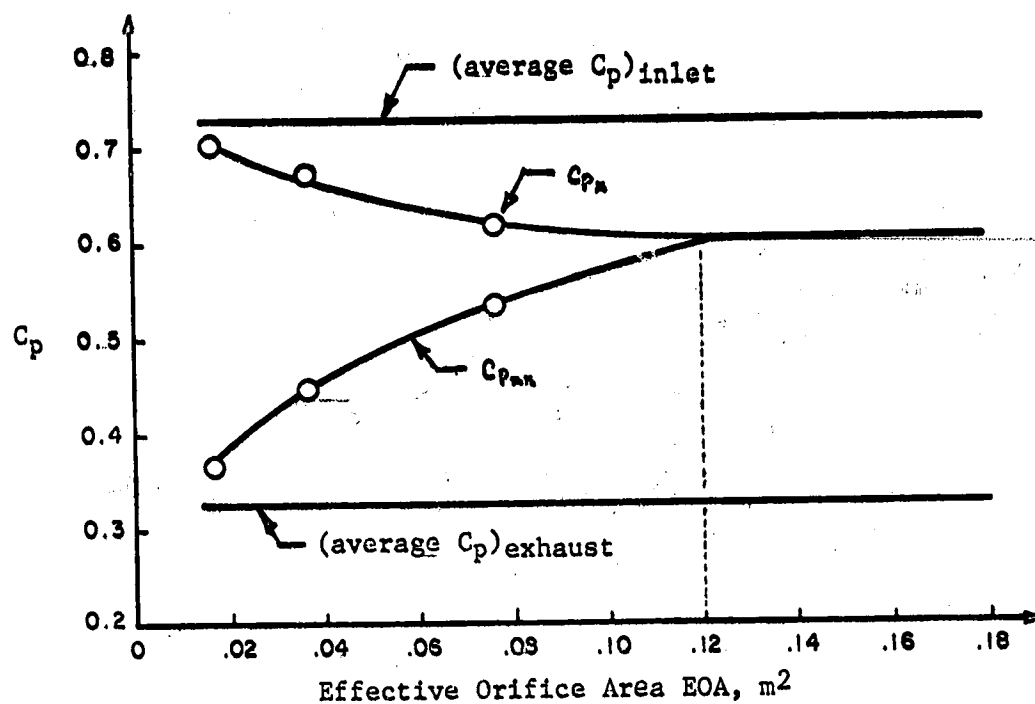


Figure 49: Behavior of pressure coefficients with effective orifice area.

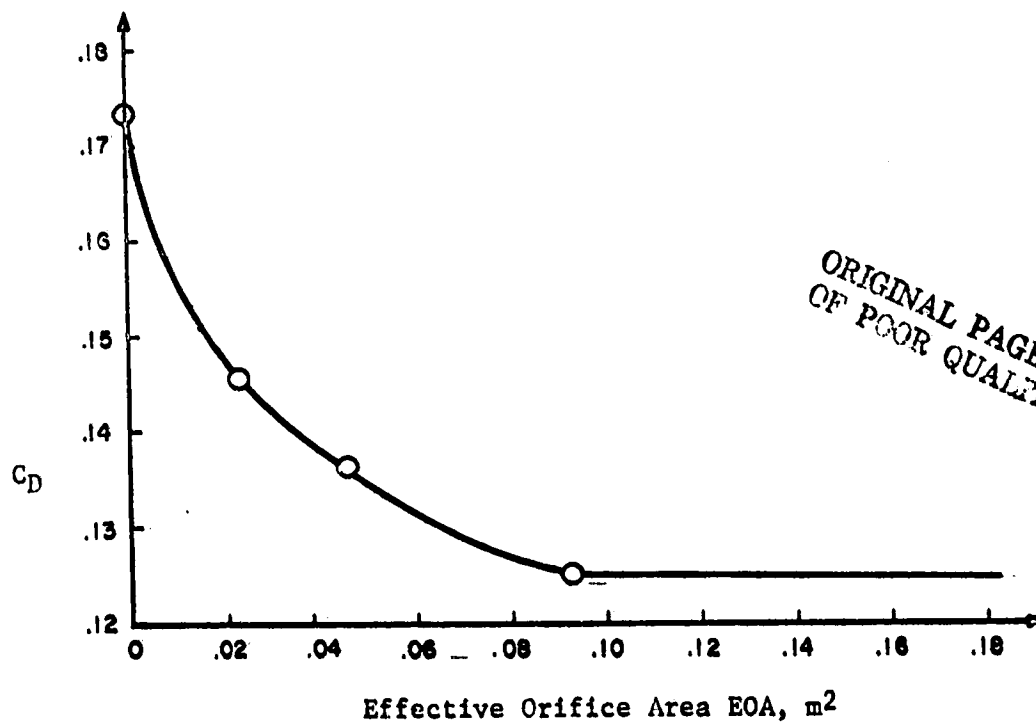
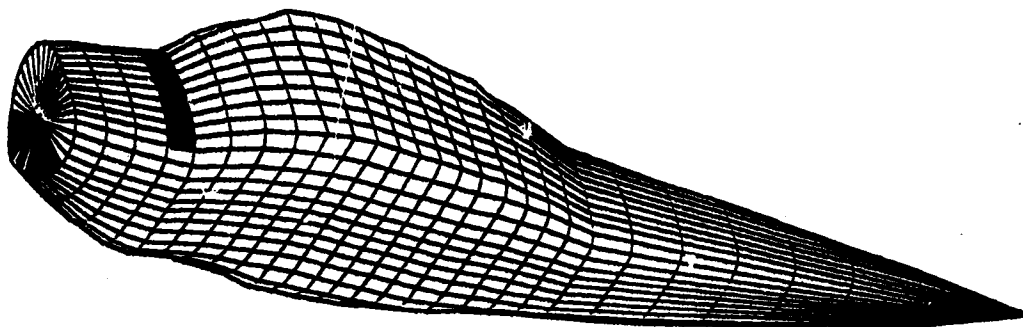


Figure 50: Behavior of drag coefficient with effective orifice area.

ORIGINAL PAGE IS
OF POOR QUALITY.

Body Description: Blunt-nose Cessna 182 Fuselage Model
Flow Description: Nonuniform



(Shaded areas denote ports for air intake and exhaust)

Test Conditions:

Freestream velocity (VIN _F), m/sec	48.768
Freestream density (ROE), kg/m ³	1.2252
Freestream temperature (TIN _F), °K	288.86
Kinematic viscosity (VO), m ² /sec	1.486×10^{-5}
Constant-pressure specific heat of air (CPHA), kJ/kg°K ...	0.3095
Reference area (REFA), m ²	16.165
Heat of combustion of fuel (HVF), kJ/kg	41787.54
Specific fuel consumption (SFC), kg/kJ	1.5561×10^{-4}
Developed engine power (DEP), kW	74.563
Initial effective orifice area (EOA), m ²	0.02322
Reynold's number	23,750,000

Specification of non-zero normal velocities

Input Code:	MS1	MS2	NS1	NS2	Panel No.	Type
	1	2	1	2	1	Intake
	3	4	1	2	5	Intake
	4	5	1	2	7	Intake
	5	6	1	2	9	Intake
	6	7	1	2	11	Intake
	7	8	1	2	13	Intake
	8	9	1	2	15	Intake
	16	17	5	6	111	Exhaust
	17	18	5	6	113	Exhaust
	18	19	5	6	115	Exhaust
	19	20	5	6	117	Exhaust
	20	21	5	6	119	Exhaust

Figure 51: Results of blunt-nose Cessna 182 fuselage model (nonuniform flow, 74.563 kW power, 0.023 m² initial EOA, intake and exhaust ports).

ORIGINAL PAGE IS
OF POOR QUALITY

Analysis Results:

(Average C_p) _{inlet}	=	0.72902	(Average C_p) _{exhaust}	=	0.32620
Inlet area, m^2	=	0.07158	Exhaust area, m^2	=	0.05109
T_∞/T_1	=	0.542	Final EOA, m^2	=	0.01709

C_{p_x} = 0.70938
 $C_{p_{xx}}$ = 0.36477

Pressure C_L (w/o wake-body)	0.00384
Pressure C_D (w/o wake-body)	0.00787
Friction C_D	0.00665
Pressure C_L (with wake-body)	0.00381
Pressure C_D (with wake-body)	0.00791

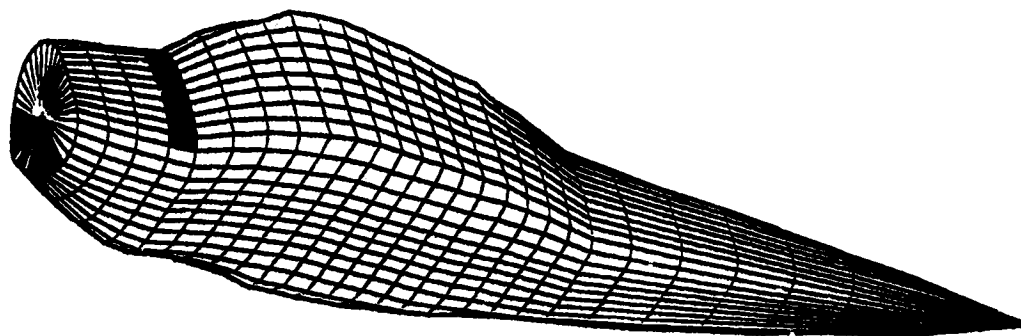
Total Body C_L = 0.00381

Total Body C_D = 0.36477

Figure 51: Concluded.

ORIGINAL PAGE IS
OF POOR QUALITY

Body Description: Blunt-nose Cessna 182 Fuselage Model
Flow Description: Nonuniform



(Shaded areas denote ports for air intake and exhaust)

Test Conditions: -

Freestream velocity (VIN _F), m/sec	48.768
Freestream density (ROE), kg/m ³	1.2252
Freestream temperature (TIN _F), °K	288.86
Kinematic viscosity (VO), m ² /sec	1.486×10^{-5}
Constant-pressure specific heat of air (CPHA), kJ/kg°K	0.3095
Reference area (REFA), m ²	16.165
Heat of combustion of fuel (HVF), kJ/kg	41787.54
Specific fuel consumption (SFC), kg/kJ	1.5561×10^{-4}
Developed engine power (DEP), kW	74.563
Initial effective orifice area (EOA), m ²	0.04645
Reynold's number	23,750,000

Specification of non-zero normal velocities

Input Code:	MS1	MS2	NS1	NS2	Panel No.	Type
	1	2	1	2	1	Intake
	3	4	1	2	5	Intake
	4	5	1	2	7	Intake
	5	6	1	2	9	Intake
	6	7	1	2	11	Intake
	7	8	1	2	13	Intake
	8	9	1	2	15	Intake
	16	17	5	6	111	Exhaust
	17	18	5	6	113	Exhaust
	18	19	5	6	115	Exhaust
	19	20	5	6	117	Exhaust
	20	21	5	6	119	Exhaust

Figure 52: Results of blunt-nose Cessna 182 fuselage model (nonuniform flow, 74.563 kW power, 0.046 m² initial EOA, intake and exhaust ports).

ORIGINAL PAGE IS
OF POOR QUALITY

Analysis Results:

(Average C_p) _{inlet}	=	0.72902	(Average C_p) _{exhaust}	=	0.32621
Inlet area, m^2	=	0.07158	Exhaust area, m^2	=	0.05109
T_w/T_1	=	0.643	Final EOA, m^2	=	0.03726
	C_{p_x}	=	0.66847		
	$C_{p_{xx}}$	=	0.44504		

Pressure C_L (w/o wake-body)	0.00202
Pressure C_D (w/o wake-body)	0.00690
Friction C_D	0.00666
Pressure C_L (with wake-body)	0.00199
Pressure C_D (with wake-body)	0.00694

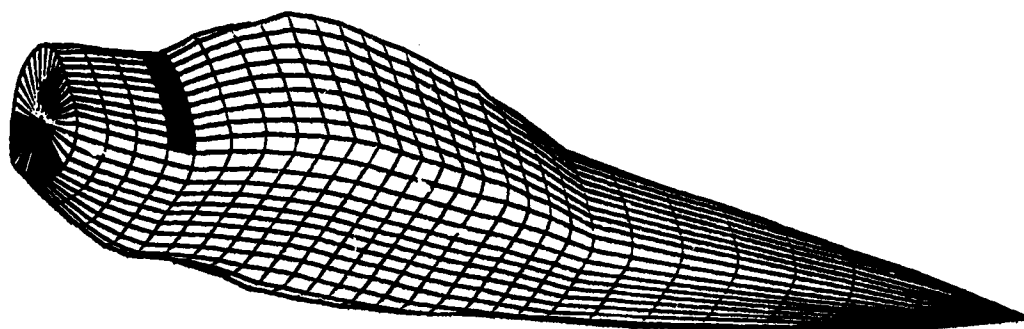
$$\text{Total Body } C_L = 0.00199$$

$$\text{Total Body } C_D = 0.01360$$

Figure 52: Concluded.

ORIGINAL PAGE IS
OF POOR QUALITY

Body Description: Blunt-nose Cessna 182 Fuselage Model
Flow Description: Nonuniform



(Shaded areas denote ports for air intake and exhaust)

Test Conditions:

Freestream velocity (VIN _F), m/sec	48.768
Freestream density (ROE), kg/m ³	1.2252
Freestream temperature (TIN _F), °K	288.86
Kinematic viscosity (VO), m ² /sec	1.486 × 10 ⁻⁵
Constant-pressure specific heat of air (CPHA), kJ/kg°K	0.3095
Reference area (REFA), m ²	16.165
Heat of combustion of fuel (HVF), kJ/kg	41787.54
Specific fuel consumption (SFC), kg/kJ	1.5561 × 10 ⁻⁴
Developed engine power (DEP), kW	74.563
Initial effective orifice area (EOA), m ²	0.0929
Reynold's number	23,750,000

Specification of non-zero normal velocities

Input Code:	MS1	MS2	NS1	NS2	Panel No.	Type
	1	2	1	2	1	Intake
	3	4	1	2	5	Intake
	4	5	1	2	7	Intake
	5	6	1	2	9	Intake
	6	7	1	2	11	Intake
	7	8	1	2	13	Intake
	8	9	1	2	15	Intake
	16	17	5	6	111	Exhaust
	17	18	5	6	113	Exhaust
	18	19	5	6	115	Exhaust
	19	20	5	6	117	Exhaust
	20	21	5	6	119	Exhaust

ORIGINAL PAGE IS
OF POOR QUALITY

Figure 53: Results of blunt-nose Cessna 182 fuselage model (nonuniform flow, 74.563 kW power, 0.093 m² initial EOA, intake and exhaust ports).

ORIGINAL PAGE IS
OF POOR QUALITY

Analysis Results:

(Average C_p) _{inlet}	= 0.72902	(Average C_p) _{exhaust}	= 0.32621
Inlet area, m ²	= 0.07158	Exhaust area, m ²	= 0.05109
T_∞/T_1	= 0.689	Final EOA, m ²	= 0.07709

C_{p_x} = 0.62370
 $C_{p_{xx}}$ = 0.53290

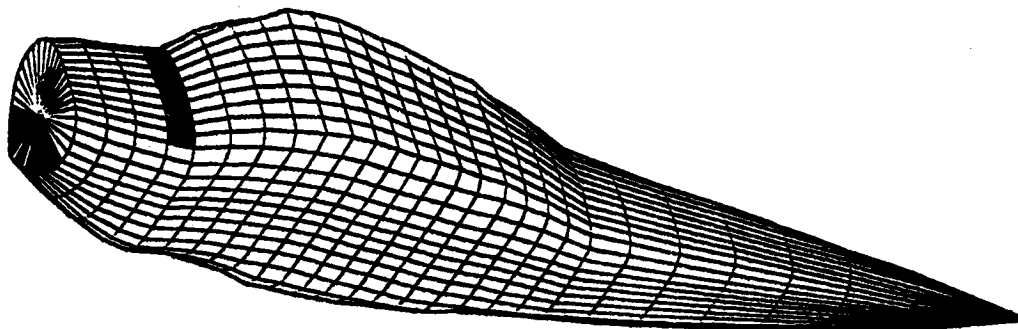
Pressure C_L (w/o wake-body)	0.0037
Pressure C_D (w/o wake-body)	0.00574
Friction C_D	0.00666
Pressure C_L (with wake-body)	0.00033
Pressure C_D (with wake-body)	0.00578

Total Body C_L = 0.00033

Total Body C_D = 0.01244

Figure 53: Concluded.

Body Description: Blunt-nose Cessna 182 Fuselage Model
Flow Description: Nonuniform



(Shaded areas denote ports for air intake and exhaust)

Test Conditions:

Freestream velocity (VIN _F), m/sec	48.768
Freestream density (ROE), kg/m ³	1.2252
Freestream temperature (TIN _F), °K	288.86
Kinematic viscosity (VO), m ² /sec	1.486×10^{-5}
Constant-pressure specific heat of air (CPHA), kJ/kg°K ...	0.3095
Reference area (REFA), m ²	16.165
Heat of combustion of fuel (HVF), kJ/kg	41787.54
Specific fuel consumption (SFC), kg/kJ	1.5561×10^{-4}
Developed engine power (DEP), kW	74.563
Initial effective orifice area (EOA), m ²	0.9290
Reynold's number	23,750,000

Specification of non-zero normal velocities

Input Code:	MS1	MS2	NS1	NS2	Panel No.	Type
	1	2	1	2	1	Intake
	3	4	1	2	5	Intake
	4	5	1	2	7	Intake
	5	6	1	2	9	Intake
	6	7	1	2	11	Intake
	7	8	1	2	13	Intake
	8	9	1	2	15	Intake
	16	17	5	6	111	Exhaust
	17	18	5	6	113	Exhaust
	18	19	5	6	115	Exhaust
	19	20	5	6	117	Exhaust
	20	21	5	6	119	Exhaust

ORIGINAL PAGE IS
OF POOR QUALITY

Figure 54: Results of blunt-nose Cessna 182 fuselage model (nonuniform flow, 74.563 kW power, 0.929 m² initial EOA, intake and exhaust ports).

Analysis Results:

(Average C_p) _{inlet}	= 0.72902	(Average C_p) _{exhaust}	= 0.32621
Inlet area, m^2	= 0.07158	Exhaust area, m^2	= 0.05109
T_∞/T_1	= 0.708	Final EOA, m^2	= 0.78153

C_{p_x} = 0.59344
 $C_{p_{xx}}$ = 0.59230

Pressure C_L (w/o wake-body) -0.00069
 Pressure C_D (w/o wake-body) 0.00493
 Friction C_D 0.00666
 Pressure C_L (with wake-body) -0.00073
 Pressure C_D (with wake-body) 0.00574

Total Body C_L = -0.00073
 Total Body C_D = 0.01240

Figure 54: Concluded.

CONCLUSIONS

1. A technique has been developed which can yield physically-acceptable skin-friction and pressure drag coefficients for isolated light aircraft bodies.
2. For test cases, the technique has predicted drag reductions as much as 28.5% by body recontouring and proper placements and sizing of the cooling air intakes and exhausts.
3. The predicted total drag coefficient for the ATLIT airplane using this approach was only 2.3% larger than that obtained by Holmes [16] using other techniques. Since the present work pertained to fuselage and nacelle drag predictions, drag contributed from other aircraft components were made identical to those of Holmes.
4. Simulating the propeller flow by systems of ring vortices appears to be adequate for use with most isolated bodies. The equivalent circular-body concept may be unsuitable for wide flat bodies. In such cases, an ellipsoidal-body concept would be preferable.

REFERENCES

ORIGINAL PAGE IS
OF POOR QUALITY

1. Hess, J. L.; and Smith, A. M. O.: "Calculation of Nonlifting Potential Flow about Arbitrary Three-Dimensional Bodies". Douglas Aircraft Company Report No. ES 40622, March 1962.
2. Hess, J. L.; and Smith, A. M. O.: "Calculation of Potential Flow About Arbitrary Bodies". Progress in Aeronautical Sciences, Vol. 8, pp. 1-138, Pergamon Press, 1967.
3. Kellogg, O. D.: Foundations of Potential Theory, Dover Publications, Inc., New York, 1953.
4. Smetana, F. O.; Summey, D. C.; Smith, N. S.; and Carden, R. K.: "Light Aircraft Lift, Drag, and Moment Prediction - A Review and Analysis". NASA CR-2523, May 1975, 480 pages.
5. Hess, J. L.: "A Fully Automatic Combined Potential-Flow Boundary-Layer Procedure for Calculating Viscous Effects on the Lifts and Pressure Distributions of Arbitrary Three-Dimensional Configurations". Douglas Aircraft Company Report No. MDC J7491, June 1977.
6. Lighthill, M. J.: "On Displacement Thickness". J. of Fluid Mech., Part 4, 1958.
7. Stepniewski, W. Z.: "Rotary-Wing Aerodynamics". NASA CR-3082, Vol. I, II, January 1979.
8. Baskin, V. E.; Vil'dgrube, L. S.; Vozhdayev, Ye. S.; and Maykapar, G. I.: "Theory of the Lifting Airscrew". NASA TT F-823, February 1976.
9. Dommasch, Daniel O.; Sherby, Sydney S.; and Connolly, Thomas F.: Airplane Aerodynamics. Pitman Publishing Corporation, 1967.
10. Basset, A. B.: A Treatise on Hydrodynamics. Vol. 2, Dover Publications, Inc., 1961.
11. Ahlberg, J. H.; Nilson, Edwin N.; and Walsh, Joseph L.: The Theory of Splines and Their Applications. Academic Press, New York, 1967.
12. Greville, T. N. E.: Theory and Applications of Spline Functions. Academic Press, New York, 1969.
13. Craidon, Charlotte B.: "Description of a Digital Computer Program for Airplane Configuration Plots". NASA TM X-2374, September 1970.
14. Halsey, N. Douglas; and Hess, John L.: "A Geometry Package for Generation of Input Data for a Three-Dimensional Potential-Flow Program". NASA CR-2962, June 1978.

ORIGINAL PAGE 19
OF POOR QUALITY

15. Schlichting, H.: Boundary Layer Theory. McGraw-Hill Book Co., Inc., New York, Sixth Edition, 1968.
16. Holmes, B. J.: "Flight Evaluation of an Advanced Technology Light Twin-Engine Airplane (ATLIT)." NASA CR-2832, July 1977.
17. Smetana, F. O.; and Fox, S. R.: "Flight Test Evaluation of Predicted Aircraft Drag, Performance, and Stability." NASA CR-159062, May 1979.
18. Shivers, J. P.; Fink, M. P.; and Ware, G. M.: "Full-Scale Wind-Tunnel Investigation of the Static Longitudinal and Lateral Characteristics of a Light Single-Engine Low-Wing Airplane." NASA TN D-5857, June 1970.
19. Fink, M. P.; Shivers, J. P.; and Smith, C. C., Jr.: "A Wind-Tunnel Investigation of Static Longitudinal and Lateral Characteristics of a Full-Scale Mockup of a Light Twin-Engine Airplane." NASA TN D-6238, April 1971.
20. Wood, K. D.: Aerospace Vehicle Design: Aircraft Design. Johnson Publishing Co., Colorado, Vol. I, Third Edition, 1968.
21. Coe, P. L., Jr.: "Review of Drag Clean-up Tests in Langley Full-Scale Tunnel (From 1935 to 1945) Applicable to Current General Aviation Airplanes." NASA TN D-8206, June 1976.